Functional properties of Plasma polymer coatings deposited using a hollow cathode arc discharge based PECVD process

Top, Michiel

rijksuniversiteit groningen

Functional properties of plasma polymer coatings deposited using a hollow cathode arc discharge based PECVD process

Proefschrift

ter verkrijging van de graad van doctor aan de
Rijksuniversiteit Groningen
op gezag van de
rector magnificus, prof. dr. E. Sterken
en volgens besluit van het College voor Promoties.

De openbare verdediging zal plaatsvinden op

vrijdag 5 oktober 2018 om 09.00 uur

door

Michiel Top

geboren op 8 Januari 1991

te Amersfoort

Promotor

Prof. dr. J. Th. M. de Hosson

Copromotor

Dr. J. Fahlteich

Beoordelingscommissie

Prof. dr. ing. G. Gerlach

Prof. dr. P. Rudolf

Prof. dr. H.A. de Raedt

Functional properties of plasma polymer coatings deposited using a hollow cathode arc discharge based PECVD process

Michiel Top

PhD thesis
University of Groningen

Zernike Institute PhD thesis series 2018-28
ISSN: 1570-1530
ISBN: 978-94-034-0874-3 (Printed version)
ISBN: 978-94-034-0873-6 (Electronic version)
Print: Ipskamp Printing

The research presented in this thesis was performed in a collaboration between the Materials Science group of the department of Applied Physics of the Zernike Institute for Advanced Materials at the University of Groningen (The Netherlands) and the department of flat and flexible products at the Fraunhofer Institute for Organic Electronics, Electron Beam and Plasma technology (FEP) in Dresden (Germany).

This work was funded by the Fraunhofer Institute for Organic Electronics, Electron Beam and Plasma technology.

Cover: Photograph of the hollow cathode arc discharge plasma in the lab coater *labFlex® 200* at Fraunhofer FEP.
Cover design by Finn Hoyer and Michiel Top.

university of groningen / faculty of science and engineering / zernike institute for advanced materials

Table of content

Chapter 1

Introduction

Flexible, light-weight and low-cost are three driving properties that boosted the application of polymer films into numerous applications. Even though the main development and industrialization only took place within the last century [1], polymer films play an important role in our daily life. In 2014, the world production of plastic was estimated around 311 million tons [2]. Nowadays, it is impossible to imagine many large industries, including the food packaging industry, car industry and consumer electronics industry, without plastics.

Even though plastic films combine these great properties of being flexible, light-weight and general low-cost, they have many material properties that limit their application. Polymer films show low thermal stability and inferior mechanical performance compared to glass or metals. A major drawback in the food packaging and organic electronic industry is the high permeability of water vapor and oxygen through the film leading to reduced lifetimes of e.g. packed food or flexible organic electronic devices.

The functionality of polymer films is often modified or improved by the application of thin coatings (usually below 1 µm) using thin film deposition techniques like sputtering, evaporation or Plasma Enhanced Chemical Vapor Deposition (PECVD). PECVD became a designation for a collection of coating technologies that use a plasma to initiate a chemical reaction between volatile and reactive compounds in order to generate a non-volatile compound on top of a substrate [3]. Compared to thermal CVD where the reaction is thermally activated, PECVD uses the plasma while keeping the

substrate at a low temperature allowing the usage in fields where low temperature deposition is required, e.g. organic electronics [4] and sensor-actuator industry [5].

1.1 Industrial perspective

A major economic advantage of flexible polymeric substrates, compared to rigid substrates, is the ability to use a roll-to-roll coating process. The substrate material is available as a compact roll of material. The sample passes one or multiple deposition stations during the deposition in order to deposit a single or multi-layer coating, respectively, and is finally wrapped around a new core. An example of a roll-to-roll coater is the *novoFlex® 600*, which is shown in Figure 1. Figure 1a shows a picture of this roll-to-roll coater that is used at Fraunhofer FEP to qualify vacuum deposition processes at a pilot-production scale. Figure 1b shows a schematic representation of the *novoFlex® 600*. The winder and unwinder are shown at the upper left and upper right. The blue line represents the path-way of the substrate through the coater. The substrate passes several deposition stations and in-line inspection systems along the path-way. The latter ones are used for quality control and to check the plasma process stability over time. The *novoFlex® 600* can be used to coat substrates up to 650 mm width. Within industrial production, the dimensions of these reels go up to several meters web width and lengths up to several tens of kilometer.

Apart from increased film width and length, the combination between the deposition speed and required film thickness determine the speed of the web passing through the web coater. Both optimization of the deposition speed as well as reduction of the coating thickness, without losing the functional performance, contribute towards the enhanced time-efficiency of the deposition process.

This lead to the development of a variety of PECVD setups over the years using different pressures ranging from high vacuum (sub Pascal domain) up to atmospheric pressure [6–9], a variety of plasma sources (including microwave [6,10–13], radio frequency [14–16], electron cyclotron resonance [17,18], magnetron [19,20] and hollow cathode [19,21,22]) to improve the coating properties and deposition speed while minimizing the production costs. The high electron density generated by the hollow cathode

arc discharge and the high ionization of the process gas opens the road to fast deposition of functional coatings. This makes the process especially very attractive for the in-line deposition of relatively thick (~ 1 µm) coatings with other coating technologies were thinner films are required. The long-time experience of Fraunhofer FEP with hollow cathodes for the application in evaporation technologies [23,24] allows for fast transfer to the industry of the hollow cathode based PECVD process provided that the mechanisms for the thin film growth are understood.

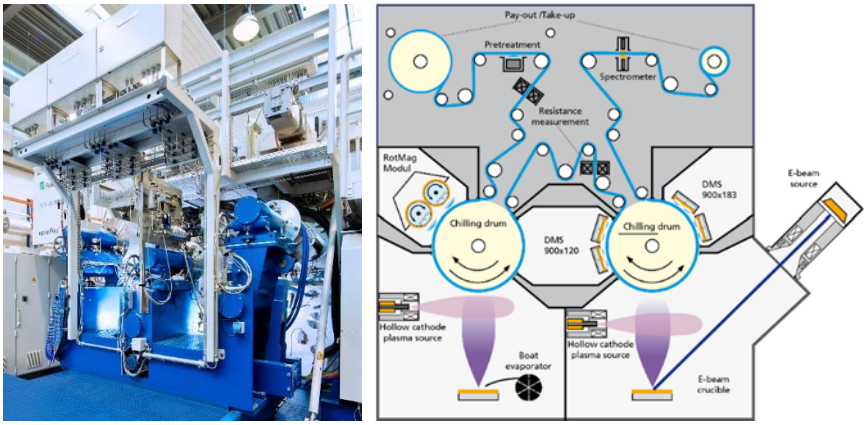

(a) (b)

Figure 1. (a): Image of the web coater NovoFlex® 600. (b) Schematic representation of the web coater.

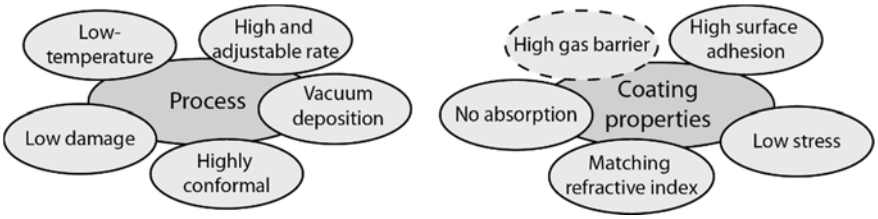

Figure 2. Schematic representation of the requirements to the deposition process and coating properties for thin film encapsulation.

1.2 Scientific perspective

From a scientific point of view, it is important to understand the film growth mechanisms of these thin films, which are deposited under high speed deposition conditions in a roll-to-roll web coater. Understanding the film growth mechanisms allows us to tailor the coating properties corresponding to their applications and helps to find the limitations in order to further improve the deposition process.

This thesis characterizes coatings deposited with a hollow cathode arc discharge based PECVD process and focuses on the gas permeation barrier and residual stress properties. These properties are critical for many applications including thin film encapsulation of organic electronic devices (e.g. organic photovoltaics of organic light emitting diodes) or as a mechanical protective coating on plastic substrates or fragile ceramic coatings. The goal within this thesis is to create an understanding how process parameters influence the chemical structure of the coating and how these changes affect the functional performance.

The most stringent requirements are most likely needed for the thin film encapsulation (TFE) of organic electronic devices. TFE comprises all deposition techniques were the water vapor and oxygen barriers are directly deposited on top of an organic electronic device. Thin film encapsulation puts stringent requirements both on the process as well as on the coating properties. Figure 2 gives a schematic overview of the process and coating requirements.

At the processing side, it is important that the substrate temperature remains low (usually below 100-150 °C) as higher temperatures induce degradation reactions [25] or influences the crystalline state of the hole transport layers [26] within the organic electronic devices. High-energy particle bombardment and UV-radiation may lead to degradation [27] and should, when possible, be avoided as well. To avoid degradation in air and mechanical contact with the active layers, it is preferred to deposit the coating directly in vacuum in-line with the active device. Depositing the layer in-line in a roll-to-roll setup requires a high and adjustable rate. It is common to adjust the coating thickness by adjustment of the web speed.

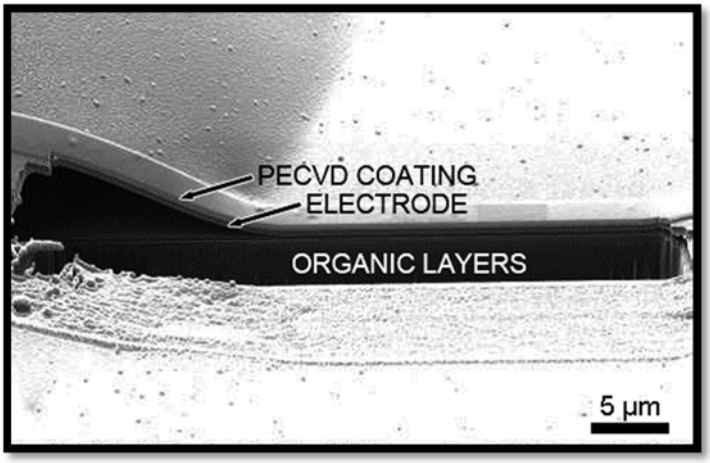

Figure 3. An SEM image of a thick PECVD coating with high residual stresses deposited on an organic PV device. The internal stress in the thick PECVD coating leads to delamination of the interface between the electrode and the organic.

For TFE applications, the web speed is usually set by the deposition speed of the (usually) much thinner layers within the active device. Obtaining a thick coating requires a much higher deposition rate to guarantee the in-line deposition of thick protective coatings.

Looking at the coating properties, absorption is unwanted as it reduces the amount of light getting into the device. To avoid interference effects, a refractive index similar to the adjacent layers is advantageous. If additional coatings are applied, a high surface adhesion is necessary to avoid delamination. PECVD deposited coatings have residual stresses, which could lead to delamination of the underlying interfaces. Figure 3 shows an example of a thick PECVD coating on an OPV device. The residual stress in the PECVD coating leads to delamination of the underlying electrode from the organic coatings. Therefore it is important to fully understand the residual stress formation mechanism in order to reduce the residual coating stress and avoid delamination of the underlying layer stack.

The most stringent requirement remains the gas permeation barrier. The deposition of a barrier coating on a polymer substrate is still highly challenging and is strongly affected by the surface quality of the film. Deposition on top of a device poses even more challenges as the surface

quality is usually not perfectly smooth due to the initial process steps. A recent review shows that it is possible to use static deposition for the application of a coating that has all required properties but are still far away from industrial uptake due to extremely low deposition speeds and therefore long tact times [28].

Even without the high barrier performance, a “thick” plasma polymer coating on top of an active device can fulfill many applications:

1 Preliminary barrier coating against H_2O and O_2

2 Mechanical protection during further processing steps

3 Permeation barrier for aggressive chemicals migrating from the adhesive

4 Adhesion improvement layer

As shown in Figure 3, a major challenge for the application of thick films is the reduction of residual stresses. The origin of residual stresses in thick hybrid organic/inorganic coatings on polymer webs is not widely discussed in literature. Especially for roll-to-roll deposited coatings, scant literature is available. Residual stress is often described as a combination of intrinsic stresses and thermal stresses. The latter one is related to the difference in thermal expansion coefficient between the coating and substrate and is often not considered for low temperature PECVD processes. An often ignored contribution towards residual stress is hygroscopic expansion. For roll-to-roll deposited films, not only the stresses related to the coating properties but also externally applied forces during winding should be taken into account. The contributions of the different mechanisms usually depend on the type of coating and the type of substrate.

The reliable characterization of the mechanical properties of the coating as well as the residual stress for thin (< 1 µm) coatings on polymer substrates is a challenging topic as well and the classical methods are often not applicable. Within this research, a comparison of the available methods for mechanical characterization are given and a novel measurement setup was designed and tested to characterize the residual stress.

1.3 Scope of the thesis

This thesis focuses on the characterization of roll-to-roll deposited silicon-containing plasma polymer coatings that are deposited in a roll-to-roll process using a hollow cathode arc discharge plasma source.

Chapter 2 will present an introduction to the hollow cathode arc discharge based PECVD process. The different components of the deposition geometry will be introduced and a literature overview of the physical mechanisms will be provided. The chapter finishes with a brief overview of the used thin film coating technologies.

Chapter 3 investigates the chemical and gas barrier properties of the coatings and discusses the effect of the oxygen flow and the applied plasma power on the water vapor permeation rate for SiO_x coatings with high carbon concentration.

The second part of this thesis focusses on the mechanical properties and residual stresses. **Chapter 4** introduces a novel method to measure the radius of curvature of highly curved samples and discusses the practical limitations of nanoindentation for the measurement of the mechanical properties of stiff coatings on flexible polymer substrates. Alternative methods, including PeakForce Quantitative Nanomechanic property Mapping, Dynamic Mechanical Analysis (nanoDMA) on the coating cross-section and Atomic Force Acoustic Microscopy (AFAM), are evaluated and a discussion is provided on the advantages and disadvantages of the individual methods.

Chapter 5 is dedicated to scrutinize the origin of residual stresses for silicon-containing plasma polymeric coatings on a polymer web using a roll-to-roll web coater. The effect of the applied web tension and viscoelastic deformation is discussed and quantified. An extensive study was performed on the stress induced due to changes the relative humidity after the deposition. Accurate curvature measurement under a controlled humidity allowed the calculation of the coefficient of hygroscopic expansion. These measurement provide valuable and significant information for the understanding of failure modes in silicon-containing plasma polymeric coatings. The chapter concludes with an investigation on the relation between the intrinsic stress and the carbon concentration in the coating.

Chapter 6 concludes this thesis and provides an outlook on the possible applications for silicon containing-plasma polymers deposited using hollow cathode active arc discharge based PECVD.

1.4 References

[1] A.L. Andrady, M.A. Neal, Applications and societal benefits of plastics, Philosophical Transactions of the Royal Society B: Biological Sciences 364 (2009) 1977–1984.

[2] PlasticsEurope, Plastics - the Facts 2015 (2015) http://www.plasticseurope.org/information-centre/publications.aspx.

[3] G. Franz, Low Pressure Plasmas and Microstructuring Technology, Springer Berlin Heidelberg, Berlin, Heidelberg (2009).

[4] W. Huang, X. Wang, M. Sheng, L. Xu, F. Stubhan, L. Luo, T. Feng, F. Zhang, S. Zou, Low temperature PECVD SiNx films applied in OLED packaging, Mater. Sci. Eng. B 98 (2003) 248–254.

[5] G. Suchaneck, V. Norkus, G. Gerlach, Low-temperature PECVD-deposited silicon nitride thin films for sensor applications, Surf. Coat. Technol. 142–144 (2001) 808–812.

[6] V. Hopfe, Remote Microwave PECVD for Continuous, Wide-Area Coating Under Atmospheric Pressure, Chemical Vapor Deposition 11 (2005) 497–509.

[7] R. Morent, N. de Geyter, T. Jacobs, S. van Vlierberghe, P. Dubruel, C. Leys, E. Schacht, Plasma-Polymerization of HMDSO Using an Atmospheric Pressure Dielectric Barrier Discharge, Plasma Process. Polym. 6 (2009) 537-542.

[8] P.A. Premkumar, S.A. Starostin, M. Creatore, H. de Vries, Paffen, Roger M. J., P.M. Koenraad, van de Sanden, Mauritius C. M., Smooth and Self-Similar SiO_2-like Films on Polymers Synthesized in Roll-to-Roll Atmospheric Pressure-PECVD for Gas Diffusion Barrier Applications, Plasma Process. Polym. 7 (2010) 635–639.

[9] R. Reuter, K. Rügner, D. Ellerweg, de los Arcos, Teresa, A. von Keudell, J. Benedikt, The Role of Oxygen and Surface Reactions in the Deposition of Silicon Oxide like Films from HMDSO at Atmospheric Pressure, Plasma Process. Polym. 9 (2012) 1116–1124.

[10] D. Korzec, D. Theirich, F. Werner, K. Traub, J. Engemann, Remote and direct microwave plasma deposition of HMDSO films: comparative study, Surf. Coat. Technol. 74–75 (1995) 67–74.

[11] A. Maria Coclite, F. de Luca, K.K. Gleason, Mechanically robust silica-like coatings deposited by microwave plasmas for barrier applications, J. Vac. Sci. Technol. A 30 (2012) 61502.

[12] J. Schwarz, M. Schmidt, A. Ohl, Synthesis of plasma-polymerized hexamethyldisiloxane (HMDSO) films by microwave discharge, Surf. Coat. Technol. 98 (1998) 859–864.

[13] M. Deilmann, H. Halfmann, S. Steves, N. Bibinov, P. Awakowicz, Silicon Oxide Permeation Barrier Coating and Plasma Sterilization of PET Bottles and Foils, Plasma Process. Polym. 6 (2009) 695–699.

[14] S. Steves, Barrier coating and sterilization of plastics by microwave and radio frequency low-pressure plasmas, Bochum, 2013.

[15] M.R. Alexander, F.R. Jones, R.D. Short, Radio-Frequency Hexamethyldisiloxane Plasma Deposition: A Comparison of Plasma- and Deposit-Chemistry, Plasmas and Polymers 2 (1997) 277–300.

[16] M. Creatore, F. Palumbo, R. D'Agostino, Deposition of SiOx Films from Hexamethyldisiloxane/Oxygen Radiofrequency Glow Discharges: Process Optimization by Plasma Diagnostics, Plasmas and Polymers 7 (2002) 291–310.
[17] F. Plais, B. Agius, F. Abel, J. Siejka, M. Puech, G. Ravel, P. Alnot, N. Proust, Low Temperature Deposition of SiO2 by Distributed Electron Cyclotron Resonance Plasma‐Enhanced Chemical Vapor Deposition, Journal of The Electrochemical Society 139 (1992) 1489–1495.
[18] K.L. Seaward, J.E. Turner, K. Nauka, A.M.E. Nel, Role of ions in electron cyclotron resonance plasma‐enhanced chemical vapor deposition of silicon dioxide, J. Vac. Sci. Technol. B 13 (1995) 118‐124.
[19] S. Günther, M. Fahland, J. Fahlteich, B. Meyer, S. Straach, N. Schiller, High rate low pressure plasma-enhanced chemical vapor deposition for barrier and optical coatings, Thin Solid Films 532 (2013) 44–49.
[20] M. Fahland, T. Vogt, B. Meyer, J. Fahlteich, N. Schiller, M. Vinnichenko, F. Munnik, Deposition of functional coatings on polyethylene terephthalate films by magnetron-plasma-enhanced chemical vapour deposition, Thin Solid Films 517 (2009) 3043–3047.
[21] S. Muhl, A. Pérez, The use of hollow cathodes in deposition processes: A critical review, Thin Solid Films 579 (2015) 174–198.
[22] D. Lusk, T. Casserly, M. Gupta, K. Boinapally, Y. Cao, R. Ramamurti, P. Desai, A High Density Hollow Cathode Plasma PECVD Technique for Depositing Films on the Internal Surfaces of Cylindrical Substrates, Plasma Process. Polym. 6 (2009) S429-S432.
[23] F. Fietzke, H. Morgner, S. Günther, “Magnetically enhanced hollow cathode—a new plasma source for high-rate deposition processes”, Plasma Process. Polym. 6 (2009) S242-S246.
[24] H. Morgner, M. Neumann, S. Straach, M. Krug, The hollow cathode: a high-performance tool for plasma-activated deposition, Surf. Coat. Technol. 108–109 (1998) 513–519.
[25] N. Grossiord, J.M. Kroon, R. Andriessen, P.W. Blom, Degradation mechanisms in organic photovoltaic devices, Organic Electronics 13 (2012) 432–456.
[26] M. Hermenau, M. Riede, K. Leo, in: Stability and Degradation of Organic and Polymer Solar Cells, John Wiley & Sons, Ltd (2012), 109–142.
[27] A.G. Erlat, M. Yan, A. R. Duggal, in: W.S. Wong, A. Salleo (Eds.), Flexible Electronics: Materials and Applications, Springer US, Boston, MA (2009), 413–449.
[28] D. Yu, Y.-Q. Yang, Z. Chen, Y. Tao, Y.-F. Liu, Recent progress on thin-film encapsulation technologies for organic electronic devices, Polymer Photonics and Its Applications 362 (2016) 43–49.

Chapter 2

Hollow cathode activated arc discharge based PECVD

The broad application of plasma within the industry pushed the development of a wide variety of plasma systems. The most elementary plasma setup consists of a cathode and an anode located in vacuum. An inert gas, the process gas, is purged into the chamber. By applying an electrical current, the electrons will excite part of the process gas leading to the presence of neutral atoms, charged particles and free electrons: the plasma. Many modifications were made to the classical parallel plate geometry to optimize the coating for specific applications. For example, a toroidal source was developed to homogeneously coat around objects [1] whereas a cylindrical plasma source was developed to coat the inside of e.g. a plastic bottles [2] or containers [3]. However, adaptations were also made to change the plasma properties. In 1916, Paschen [4] was the first one who reported a cathode, which had a cavity-like geometry. It was the large discharge current of the hollow cathode that attracted the interest to this specific geometry [5]. The hollow cathode is nowadays well developed and used for the deposition of a variety of coatings [6].

This chapter gives an overview of the hollow cathode and introduces the process that takes place in the plasma. This chapter ends with a concise overview of the analytical methods used in this thesis.

Within this thesis work, the hollow cathode is used as a plasma source in a roll-to-roll deposition configuration. Figure 1 shows a schematic representation of the deposition geometry. The next three sections explain the three main elements (indicated by the three dashed circles) of the setup and provides a concise literature review of the processes that occur.

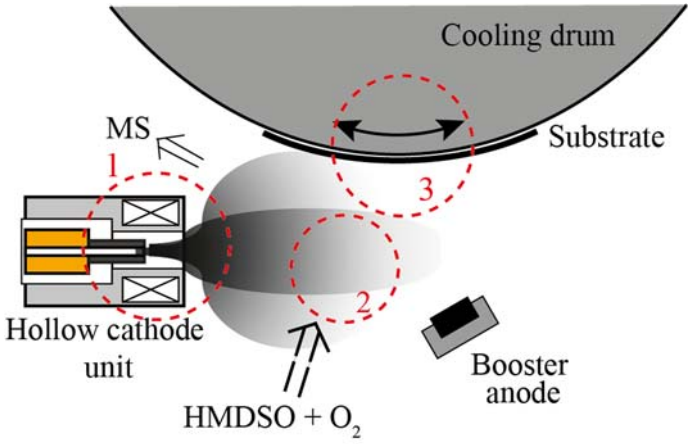

Figure 1. Schematic representation of the PECVD geometry used in this thesis. The components and processes within the three dashed circles are explained in section 2.1 till 2.3.

2.1 Hollow cathode plasma

An important part of the deposition geometry for PECVD is the plasma source. The Hollow Cathode Unit (HCU) is shown in figure 1 in the first circle. The HCU contains four components of the deposition system. The main part is the actual hollow cathode, which consists of a tube made of molybdenum. A thin cylinder made of lanthanum hexaboride (LaB_6) with an inner diameter of 5.5 mm is located within this tube. The low work function of the LaB_6 promotes the emission of electrons. A gas inlet is located at the beginning of the hollow cathode and is used to purge argon through the hollow cathode into the reaction chamber. An annular anode is placed at the end of the hollow cathode. This anode is mainly used during the initiation of the plasma as it is located close to the exit of the hollow cathode. The last component in the HCU is a double wire coil. This coil is used to create an axial magnetic field in and around the hollow cathode and is used to change

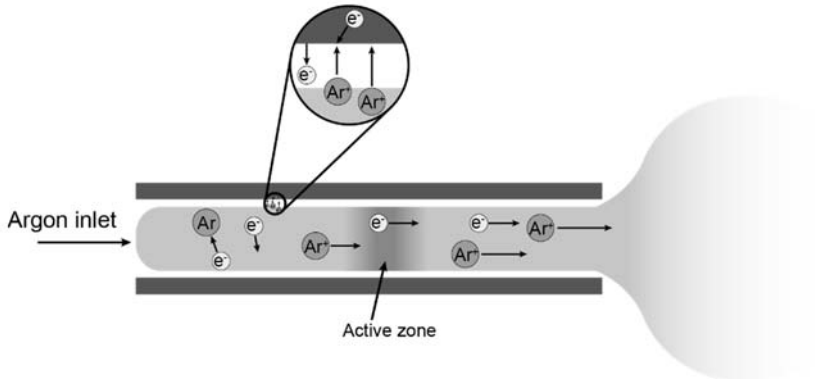

Figure 2. Working principle of a hollow cathode. Based on [7]. The pop-up shows a more detailed view of the processes in the plasma sheath.

the shape of the plasma.

The booster-anode is shown at the bottom-right side of Figure 1. This anode is a secondary anode and is used to create a dense plasma below the substrate. HMDSO and oxygen are purged into the reaction chamber using the gas shower located at the bottom of the figure.

The principle of the discharge inside the hollow cathode is displayed in Figure 2. The cathode has a cavity like geometry. On the backside, an inert gas, usually argon, is purged into the cathode. Due to the pressure gradient, the gas is accelerated through the cathode into the reactive chamber. The plasma created by the hollow cathode is divided into the internal and external plasma. The latter one will be described later on. The internal plasma, also called Internal Plasma Column (IPC), allows for the highly ionized plasma outside of the cathode.

A thin plasma sheath is presented at the inside of the cathode, which is necessary to accommodate the voltage drop between the neutral plasma and the negative charged cathode. Electrons emitted from the cathode walls are accelerated within the plasma sheath towards the center of the cylindrical cathode resulting in an increases of the electron's kinetic energy [8]. After passing through the plasma sheath, the electrons may have energies of several tens of electron volt [9], which allows them to ionize the argon atoms. When the positive ions enter the plasma sheath, they are accelerated towards the cathode wall and collide with the wall resulting in the emission

of electrons. The electron-ion collisions result in the formation of argon ions whereas the ion-wall collisions results in severe heating of the wall. The latter one allows the thermionic emission of electrons, which results in an increase of the available electrons. The large number of electrons result in a decrease of the plasma resistivity leading to the characteristic low voltage and high current of an arc discharge. The thermionic emission was found to be the primary electron source for a hollow cathode arc discharge [9].

As mentioned before, a hollow cathode plasma is known for its high electron and ion density compared to other (e.g. parallel plate) geometries. Two mechanisms contribute to this high density. The first mechanism is a result of the cavity-like geometry. Where other cathode geometries usually have only one confined direction, electrons are easily able to leave the plasma. In the hollow cathode, the electrons are confined in two directions and are only able to leave the plasma in the direction parallel to the cathode axis. This results in a reduced electron and ion loss. The second reason is also known as the hollow cathode effect. The electrons within the hollow cathode are moving in a pendulum motion through the cathode [10]. The electrons created using this pendulum motion are generally low energy electrons, which are not responsible for further ionization. However, when collisions take place within the sheath between the plasma and cathode wall, they are accelerated in the electric field allowing them to gain sufficient energy to ionize other atoms [11]. The ionization process is most efficient when the mean free path of the high speed electrons is of the order of the cathode tube diameter. This results in a balance between electron-ion and ion-wall collisions [12]. Because argon is purged through the hollow cathode, a pressure drop exists in the axial direction within the hollow cathode. As a result, a pressure gradient causes the ion density to decrease whereas the mean free path of the electrons increases as a function of the axial distance. For a specific combinations of background pressure and argon flow, a zone exists where the mean free path of the ions is on the order of the diameter of the cathode tube and a highly efficient ionization process takes place. This area is called the “active zone” [5]. The existence of the active zone was experimentally confirmed. Decroix et al. used a pyrometer to measure the temperature profile on the outside of the cathode wall. A local maximum of the wall temperature was found at the location where the active zone was predicted [5]. The electron density in the active zone is estimated around

10^{20}-10^{21} m^{-3} [9,13,14]. The length of the active zone is found to increase with the discharge current and to decrease with the mass flow rate [15].

To initiate the plasma, a high voltage pulse is applied to create an electric field. The electric field accelerates the charge carriers into the plasma area [16]. Non-elastic collisions between the electrons and the atoms results in the excitation and ionization of the atoms. The ionization will release additional electrons until an electron avalanche creates a stable hollow cathode discharge plasma. After the ignition, a glow discharge, which can be identified by a high voltage and low current, is obtained. As soon as the temperature of the cathode walls becomes sufficiently high, the voltage will drop indicating an arc discharge is present in the plasma chamber.

The efficient ionization within the IPC results in a highly ionized plasma with high electron densities directly outside the cathode. Besides the electron density, an important plasma parameter in the electron energy distribution function (EEDF). A commonly assumed EEDF is the Maxwellian shape which allows a definition of the electron temperature (T_e). Directly outside the hollow cathode, the EEDF cannot be described by a Maxwellian distribution but should be described by a Maxwellian distribution that is superimposed with a directed beam of high energy electrons [17]. This directed beam is usually called the Low Voltage Electron Beam (LVEB) and contains electrons with energies between 10 and 30 eV [18,19]. The high energy of the electrons in the LVEB make them suitable to efficiently ionize and fragmentize vaporized monomers in the reaction chamber.

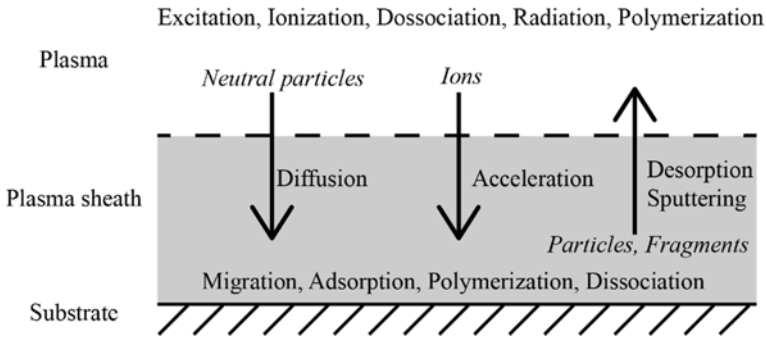

Figure 3.Process that occur during plasma enhanced chemical vapor deposition. Based on [20].

2.2 Plasma enhanced Chemical Vapor Deposition

The second circle in Figure 1 surrounds the reactive plasma zone. PECVD covers all depositions processes where a plasma is used to initiate a chemical reaction between volatile and reactive components in order to generate a non-volatile compound on top of a surface [21] and is a sub-group of chemical vapor deposition (CVD) techniques. CVD usually uses thermal activation to dissociate and activate the reactive gas and monomer. The plasma allows for much lower substrate temperatures compared to thermal CVD. It is important to mention that, in this case, low temperature processes indicate processes with substrate temperatures ranging between room temperature and approximately 200 °C [22–24]. Other effects of the plasma on the substrate are the generation of active sites as a result of ion and electron bombardment before the deposition and densification of the coating after the deposition.

The involved processes are schematically summarized in Figure 3. Is should however be mentioned that an exact correlation between plasma properties and film properties remains phenomenological as a result of a large number of unknown parameters due to the complexity of the system [20].

Plasma polymerization

Plasma polymerization can be considered as a sub-group within PECVD as well as a sub-group within polymerization. Plasma polymerization describes the deposition of polymers while using a plasma for the dissociation of the monomer.

Plasma polymerization gained attention because it allows the deposition of polymers with properties that cannot be obtained by classical polymerization. Even though the exact polymerization routes are still not completely understood, great work is done to obtain a better understanding of the processes within the plasma [25]. The polymerization model described by Yasuda [26] is nowadays widely accepted and supported by experimental data. He proposed the “atomic polymerization”- model. It is similar to the “Plasma electrical polymerization” model described by Drost [27] and the “Quasi-Hydrogen Plasma” model by Friedrich [25]. The model describes plasma polymerization as a two-step process. First, the monomer is completely dissociated by the plasma into single atoms and ions. Then, the

atoms and ions are transported to the substrate. The polymerization occurs at the surface of the substrate. The complete dissociation of the monomer is only possible when sufficient power is available within the plasma. This resulted in the factor

$$\frac{W}{FM} \tag{2.1}$$

With W the applied power, F the monomer flow and M the molecular mass of the monomer. This factor is known as the Yasuda factor and describes the importance of the applied power per unit of monomer during the fragmentation of the monomer. Several authors [25,26] found that the coatings deposited with low power per unit of monomer are more similar to classical polymers. This indicates a non-complete dissociation of the monomer where original fragments of the monomer still can be found in the deposited coating.

Reaction pathways of HMDSO and Oxygen

Extensive research has been performed on the dissociation of HMDSO [28–33]. Several authors took special interest in the dissociation of HMDSO and Oxygen [34–37]. Even though the deposition of silica containing plasma polymers is widely studied using mass spectrometry, the exact deposition mechanism is a complicated process and still not completely understood in detail. This section provides an overview of the processes that occur during the deposition of silica containing plasma polymers using PECVD. It should be mentioned that the described pathways are the dominant reaction mechanisms. In practice, the deposition mechanism is a combination of reaction mechanisms.

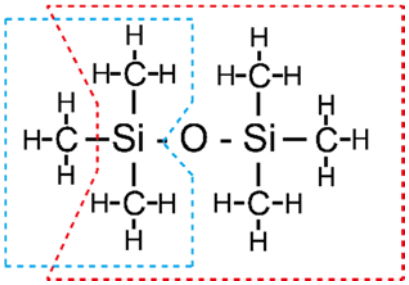

Figure 4. Commonly observed dissociation steps for HDMSO.

For the dissociation of HMDSO, most radicals and ions are formed by dissociative ionization [33]. This process leads to the formation of initiators for the polymerization process. Most authors agree that the first step in the dissociation is the removal of a methyl group [33,35–38] (red rectangle in Figure 4) which is described by

$$Si_2O(CH_3)_6 \rightarrow Si_2O(CH_3)_5^+ + CH^*_3 + e^- \quad (2.2)$$

This was confirmed by the presence of a large peak at 147 amu. Additional peaks with mass differences of 15 amu where found indicating the presence of Si-O-Si molecules with 1 up to 5 methyl groups. Breaking of Si-O bonds (blue rectangle in Figure 4) was also observed, to a lesser extent, which led to peaks at 73 and 89 amu and is described by

$$Si_2O(CH_3)_6 \rightarrow Si(CH_3)_3 + SiO(CH_3)_3 \quad (2.3)$$

Alexander et al.[39] showed that the intensity of the peak at 73 decreased compared to 147 for an increased power per unit of monomer. This indicates that for high power, the methyl extraction becomes a preferred way of fragmentation and leads to a lower organic content in the coating. Adding oxygen to the plasma increases the fragmentation rate [34,37]. The ratio between oxygen and HMDSO was found to be an important parameter for the chemical composition of the deposited thin films. With increasing oxygen present in the plasma, a higher number of HMDSO fragments oxidizes after methyl extraction which results in a reduced organic part of deposited film.

For low pressure deposition, the formation of the thin film is favored at the surface of the substrate. For high pressures (>133 Pa), the formation of “polymers” in the plasma was also observed [25].

Silica-containing plasma polymer thin films

Numerous literature reports PECVD processes were HMDSO and oxygen are used to deposit thin films. The resulting silica containing layers are described by a variety of different name. Examples are Silica-like [40], SiO2-like [41–43], SiOx [44–46], SiOCH [47], ppHMDSO [42],Plasma-polymerized HMDSO [48,49], Silicon containing [50], $SiO_xH_yH_z$ [51] or Organosilicon [52–55] thin films. All these names summarize a collection of thin films that are deposited using PECVD where a silicon containing

monomer is used together with oxygen for the deposition of layers with the chemical composition

$$SiO_xC_yH_z$$

The variety of names indicates the wide variety of possible layer properties that can be achieved using the aforementioned gas combination. Especially the gas flow ratio between HMDSO and oxygen results in a large change of the chemical composition. Whereas most plasma polymer layers are combinations of different structures, the structure that attracts the most interest is silica or SiO_2. This perfect inorganic structure is shown in Figure 5a. In three dimensions, the four oxygen atoms are surrounded in a tetrahedral coordination around the silicon atom. Chemical thermodynamics shows that the reaction that takes place can be described by [25]

$$12\ O2 + Si_2O(CH_3)_6) \rightarrow 2\ SiO_2 + 6\ CO_2 + 9\ H_2O \qquad (2.4)$$

This reaction requires 12 times more oxygen compared to HMDSO molecules. For much lower oxygen flows, the formation of polydimethylsiloxane(PDMS)-like structures [28,56] can be formed as is described by

$$8\ O_2 + 2\ Si_2O(CH_3)_6) \rightarrow 2\ (SiO(CH_3)_4)n + 4\ CO_2 + 6\ H_2O \qquad (2.5)$$

It should be mentioned that plasma polymer layers show a certain degree of cross-linking. Even for low applied power per unit monomer.

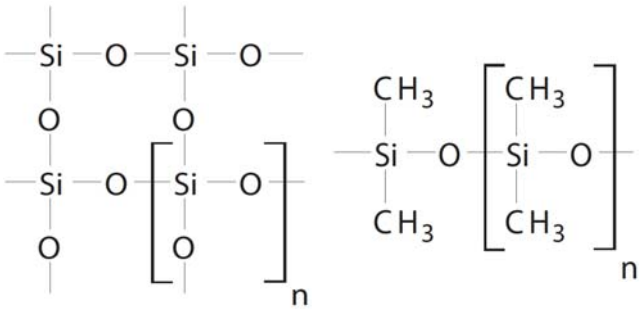

(a) (b)

Figure 5 (a) The perfect structure of SiO_2. (b) The suggested groups in a silica containing plasma polymer [42].

Both structures represent a theoretical situation. In reality, amorphous coatings are deposited that consist of a mixture of different bonds and groups. E.g. Lefèvre et al. [57] described the presence of *(-Si-O-)$_n$*-rings. They used molecular dynamics simulations to show that low-energy particle bombardment resulted in the breaking of large rings (n >=9) and formation of smaller rings (n=5-7) leading to a higher film density.

It is clear that the substrate temperature has a major influence on the process. Lowering the substrate temperature increases the sticking coefficient which results in a higher deposition rate [21] but also reduces the atom mobility at the surface.

2.3 Substrate surface

The third circle in Figure 1 surrounds the substrate and cooling drum. Whereas the previous two sections were both valid for static, dynamic and roll-to-roll deposition processes, the cooling drum is distinctive for roll-to-roll processes.

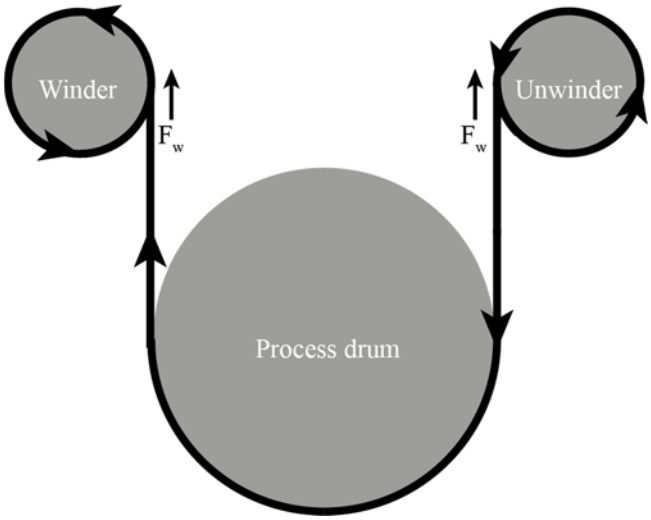

Figure 6. Schematic representation of the substrate pathway trough a roll coater.

The substrate is initially wounded around the unwinder as shown in Figure 6. After leaving the unwinder, the substrate is wrapped around the cooling drum before being rewound at the winder. The cooling drum is a metal drum equipped with a water-based cooling and heating system that enables control of the surface temperature. R2R deposition allows for the deposition of substrates reels with lengths up to 60 km. The homogeneity along the reel is mainly dependent on the time stability of the plasma process. Because the sample passes by the plasma, it is exposed to different parts of the plasma. Therefore, the lower and upper parts of the coating are deposited at the edges of the plasma cloud, which usually has lower ion energies. This could lead to slightly different properties at the top and bottom of the coating.

Both the winder and unwinder exert tension on the substrate, which will be called the web-tension. As the speed of the substrate is controlled by rotation of the cooling drum, the web-tension is necessary so as to avoid slip between the substrate and the process drum. More important, the web-tension ensures sufficient thermal contact between the substrate and process drum, which is necessary to dissipate the heat resulting from the process.

Heat load and dissipation during the deposition.

There are several contribution to the heat load during the deposition of a thin film coating on a polymer web. Literature identifies the main heat sources as [58]

- Condensation heat
- Exothermic chemical processes
- Heat generation due to ion and atom impingement
- Radiative heat of high temperature parts.

A schematic representation of the thermodynamical process is shown in Figure 7. The plasma applies a heat flux onto the substrate leading to increased substrate temperatures (darker color). The back-side of the substrate is in contact with the cooling drum, which is actively cooled by a liquid flow through the drum. This allows for heat dissipation through the back side of the substrate. The efficiency of the heat dissipation is mainly dominated by the water vapor enclosed between the substrate and the cooling drum as well as the effective contact between the substrate and drum. The

effective contact between the substrate and the cooling drum is dependent on the surface roughness and presence of particles at the interface. After the deposition, a minor part of the heat dissipates from the front side by radiation and gaseous conduction [59]. Most of the heat dissipates through the back-side and is thereby the main focus of interest for optimization.

The thermal contact between the polymer substrate and cooling drum is the critical point and is determined by a number of factors:

- Actual contact area
- Water vapor between the substrate and cooling drum
- Thermal conductivity of the substrate and cooling drum

Whereas the latter one is intrinsically material dependent, the contact area can be influenced by extrinsic properties including surface roughness of both the drum and substrate as well as contamination between the drum and substrate. Especially the presence of anti-block particles on the back-surface (used to reduce the adhesion between the substrate while being wound on the core) of the substrate could majorly influence the heat transfer. Apart from heat dissipation due to direct contact, it was found that water vapor trapped in small cavities between the substrate and cooling drum is an important heat carrier [58] which contributes to the total heat dissipation. Since the main water vapor contribution is a result of outgassing of the polymer, the heat dissipation rate becomes time-dependent which could lead to increased substrate temperature if subsequent deposition are performed on a substrate.

Literature agrees that the thermal contact between substrate and the cooling drum is the limiting interface for heat dissipation [58,60]. Therefore, it is valid to assume that the cooling drum remains at a fixed temperature. Due to the non-perfect thermal contact between substrate and cooling drum, a step-wise increase of the temperature occurs between cooling drum and substrate. In accordance to steady state heat transfer, a linear increase of the temperature is assumed in the substrate. This leads to a temperature profile as shown in Figure 8.

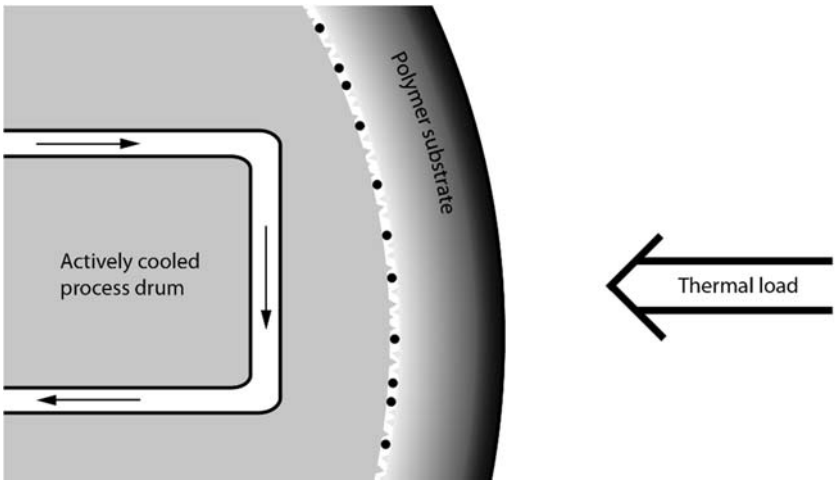

Figure 7. Schematic representation of the heat flow during a roll-to-roll deposition process. The black circles and edges represent particles and defects that reduce the effective contact area between the cooling drum and the substrate. The color gradient in the coating represents the gradient in the temperature.

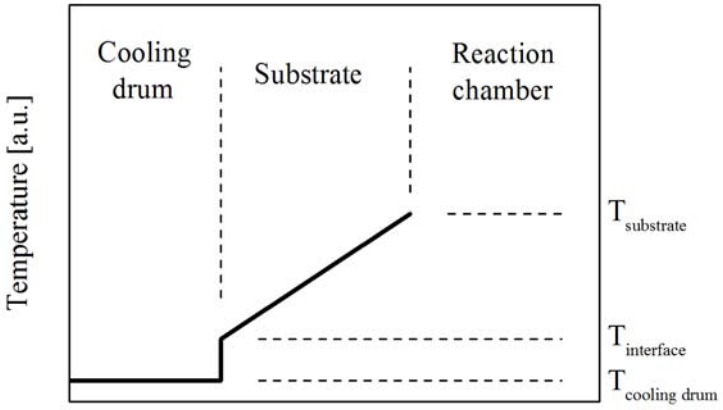

Figure 8. Assumed temperature gradient within the cooling drum and substrate.

2.4 Thin film characterization

This section provides a brief overview of the commonly used characterization techniques within this research. The mechanical characterization is discussed separately in Chapter 4 and is therefore not included in this section.

Visual light spectroscopy

Evaluation of the coating thickness measurements was performed using optical spectroscopy. The reflectance and transmittance of the samples were measured using a Perkin Elmer 900 optical spectrometer. Unless mentioned otherwise, spectra were measured for the wavelength between 300 and 1100 nm with a 2 nm resolution. The angle of incidence is 90 degrees. Before every measurement series, a reference measurement was made to check the calibration of the spectrometer. Optical simulations were performed using the commercial software SCOUT [61], based on the Lorentz Oscillator model, to obtain information on the refractive index and coating thickness. Unless mentioned otherwise, the transmittance and reflectance are simulated between 500 and 1000 nm. For lower wavelengths, the UV absorption of the substrate becomes significant and needs to be taken into account.

The model used for simulation is schematically shown in Figure 9. The light is entering the sample from the top. The light is transmitted through a dielectric coherent thin film (coating) and a thick film (substrate) and leaves the substrate at the bottom. The substrate was simulated as an incoherent layer which was recommended by Harbecke [62]. Simulation of an incoherent layer ignores the phase information of the reflected waves. The bare substrate was measured and simulated to obtain the optical properties of the substrate which are kept constant in further simulations. The refractive index, absorption and film thickness were used to fit the simulation to the measured transmittance using the “Downhill simplex”- method. The coatings are simulated with a constant n, independent of the wavelength, and setting k equal to 0 (no absorption), which is commonly applied for dielectric materials [63].

It is known from literature that thin films, deposited using PECVD, exhibit a gradient through the coating [26]. Especially for roll-to-roll deposited systems, a gradient of the plasma in the direction of movement results into a

gradient in the coated layer. When the single layer model was not sufficient to obtain a good agreement between measurement and simulation, a surface layer was introduced. It should be noticed that gradients may occur at the interface between the coating and the substrate. Within this research, no further improvements were found when adding additional sub-layers into the model.

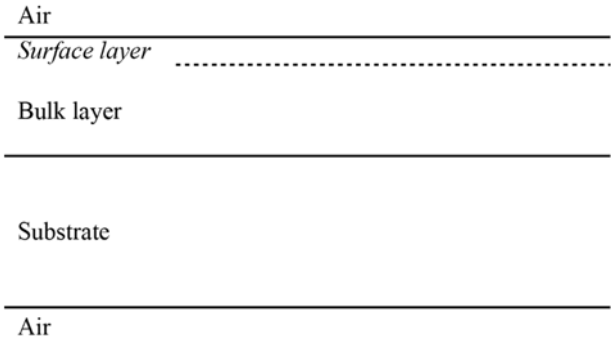

Figure 9. The simulation model used to fit the measured spectra in SCOUT. The surface layer was used for correct for coating gradients if necessary. This height of the layers is just for illustration purposes and is not to scale.

Fourier transformed Infrared spectroscopy

Information regarding the chemical bonds within the coating were obtained using Fourier Transformed Infrared Spectroscopy (FTIR). Within this research, a Perkin Elmer Spectrum 2000 was used. As the samples are extremely thin (< 1 µm) compared to the substrate thickness (75 µm), standard transmission or absorption measurement were not possible as the signal from the substrate dominates the measurement. To reduce the penetration depth of the signal, Attenuated total reflection (ATR) measurements were taken instead. The ATR adapter was equipped with a germanium crystal (n_{Ge}=4) and the beam had a 45° angle of incidence (α). The penetration depth is described by [64]

$$d_p = \frac{\lambda}{2 \cdot \pi \cdot n_{Ge} \sqrt{\sin^2 \alpha - \left(\frac{n_{coating}}{n_{Ge}}\right)^2}} \qquad (2.6)$$

where $n_{coating}$ is the refractive index of the coating material and λ is the wavelength.

Table 1. Effective measurement depth according to Eq. (2.6) for a coating with n=1.6 for selected wavelengths.

Wavenumber [cm-1]	Wavelength [nm]	Penetration depth (n=1.6) [nm]
3500	2857	195
1365	7327	500
800	12500	853

Usually, thin coatings around 500 nm are analyzed. For these coatings, it has to be taken into account that the penetration depth between 800 and 1363 cm^{-1} partly penetrates into the substrate and absorption of the substrate has to be taken into account. If required, the influence of the substrate will be discussed separately in the results.

For coatings below 500 nm thickness, the absorption in the substrate becomes larger and thereby limits the information from the coating. As an alternative to FTIR-ATR, a thin IR reflecting coating (e.g. aluminum) was applied before deposition of the plasma polymer. This allowed the measurement of all coatings independent of their thickness. However, it cannot be excluded that the aluminum interlayer influences the growth process of the plasma polymer coating and thereby this method was only used when coatings with a thickness below 500 nm were analyzed.

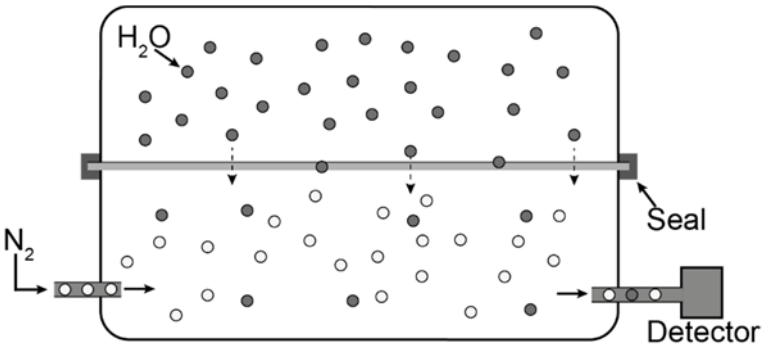

Figure 10. Schematic representation the Brugger WDDG coulometric measurement device.

Water vapor permeation measurements

Water vapor permeation measurements were performed to calculate the water vapor transmission rate (WVTR). Large area permeation measurements were made to include both intrinsic as well as defect dominated permeation. The WVTR was measured using a WDDG (Brugger Feinmechanik) measurement device. One side of the sample is exposed to a known water vapor concentration and the other side is exposed to a dry nitrogen atmosphere. As a result of the water gradient, water diffuses through the sample. The amount of water is measured using a Coulometric detector. From the diffused mass, the WVTR can be calculated according to

$$WVTR = \frac{M_{H_2O}\,[g]}{Area\,[m^2]\cdot Measurement\ time\,[day]} \tag{2.7}$$

It is important to mention that the WVTR is usually calculated when the permeation has reached a certain steady state. The time until the steady state is reached is the so-called "lag time" [65]. Unless mentioned otherwise, the tests were performed at 38 °C and 90% relative humidity. Detailed information about the measurement setup and conditions can be found in Table 2.

Table 2. Overview of the permeation measurement parameters.

Measurement Parameter	**WVTR**
Device	WDDG (Brugger Feinmechanik)
Measurement Area	78 cm²
Temperature	38 °C
Relative Humidity	90 %
Partial Pressure Oxygen	21 vol% (air)
Measurement limit	$5\cdot10^{-3}$ g/(m²day)
Measurement accuracy	$5\cdot10^{-3}$ g/(m²day)

Glow Discharge-Optical Emission Spectroscopy (GD-OES)

Glow Discharge-Optical Emission Spectroscopy uses an RF argon plasma to etch thin film coatings layer-by-layer. The removed atoms are excited by the plasma and will decay back under the emittance of a photon. The emitted photons are observed using a spectrometer and counted in an energy dispersive spectrum. Because the wavelength of these photons is defined by the energy gap between the energy bands of the atom, analyzing the spectrum provides information on the type of atoms that are removed from the composite material. This process is schematically shown in Figure 11a. Additional pulsing of the plasma is used to minimize the thermal load on the sample [66]. The intensity of the measured signal is proportional dependent on the number of atoms. As not every atom has the same emission yield [67], a calibration is necessary to properly calibrate the process before quantitative evaluation can be performed.

Hodoroba et al. [68] showed that hydrogen from the coating influences the excitation and ionization processes of other species. Literature shows that an increase in the hydrogen concentration results in a decrease of the silicon and carbon signal [69,70]. The same authors also showed that oxygen drastically increases the sputter rate without an increased oxygen signal.

The results in this research were measured with a Horiba GD-Profiler 2 using a 13,56 MHz RF Glow discharge plasma that was additionally pulsed at 3000 Hz. Figure 11b, shows a typical measurement result. The upper curves were shifted to improve the visibility. The horizontal axis shows the sputter time that under the assumption of a steady sputter rate can be converted into a depth scale. The vertical axis shows the voltage signal of the photodetectors which are set for the elements H, C, O and Si. A significant gradient in the hydrogen content is visible. After approx. 45 seconds, the Si curve goes to zero. This was used to identify the interface between coating and substrate. The non-infinite slope could be a result of silicon diffusion into the substrate or because the atoms were not removed perfectly layer-by-layer during the measurement. Besides carbon, all curves show a higher signal at the bottom of the coating. To check whether the strong increase at the interfaces was a result of the coating gradient or an artifact of the measurement, a four-layer stack was analyzed as well. As there is no significant peaks at the interfaces between the deposited layers, these peaks were assumed to be measurement artifacts and the center part of the coating was used for the analysis.

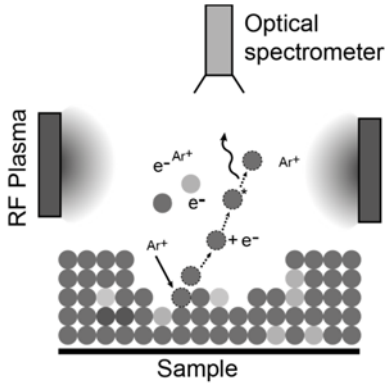

(a)

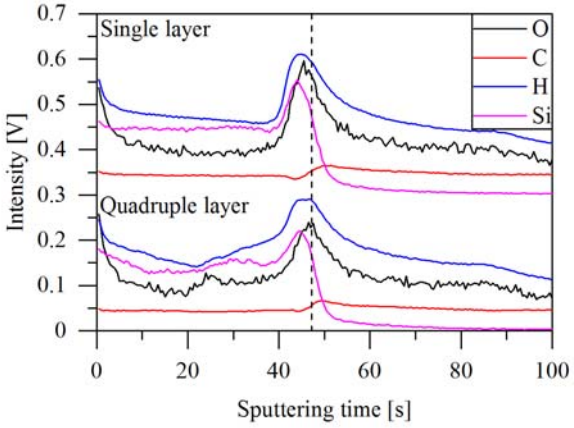

(b)

Figure 11 (a) Schematic representation of the GD-OES setup. (b) Typical spectra of the plasma polymer coating in this research. The upper and lower picture represents coatings that were deposited in 1 and 4 passes, respectively. The dashed line indicates the transition from the coating into the substrate.

Atomic Force Microscopy

The surface roughness of the coatings was measured using Atomic Force Microscopy (AFM). An "Explorer" (Topometrix) AFM was used in non-contact mode to scan a 2.3 x 2.3 µm area. (Resolution 7.7 nm/pixel). The surface roughness was defined by the arithmetic surface roughness [71].

X-Ray Reflectivity

X-ray reflectivity (XRR) is applied to analyze roughness, density and thickness of thin films and thin film stacks. In this thesis, XRR was used to gain access to the mass density of the thin films. Measurements were performed using a Bruker D8 Discover. A monochromatic X-ray beam (wavelength: 0.154 nm) was parallelized using a Göbel mirror [72]**.** Consequently, the beam was reflected onto the surface of the sample. The intensity of the reflected beam was measured using a scintillation detector as a function of the angle of incidence. Measurements were taken between 0 and 5°-10°. The measured curve is fitted to a simulation to evaluate the thin film properties. The simulation and fitting procedure were performed with the open source software Gen-X [73]. During the measurement, the flexible samples where adhered to a silica waver, which functioned as a carrier.

Already in 1923, Compton discovered that X-Rays do not penetrate into the material for small angles of incidence between the incoming beam and the surface of the material [74]. This is due to the phenomenon that is known as total reflection and can be derived from Snell's law for reflection:

$$\frac{n_1}{n_2} Cos(\theta_1) = Cos(\theta_2) \qquad (2.8)$$

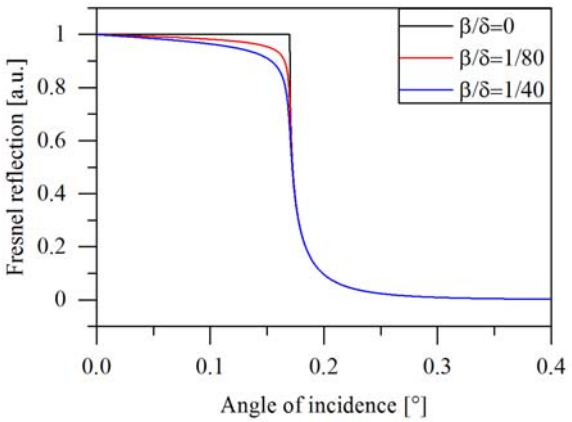

Figure 12. Fresnel reflectance for a thin film for different absorption/dispersion ratio's. The dispersive part is chosen in such a way that the critical angle is fixed at 0.17. Based on an image of Tolan et al.[75].

When light wants to enter a low refractive medium (compared to the medium it is leaving e.g. $n_2<n_1$) under a small angle, $n_1/n_2 Cos(\theta_1)$ could become larger than 1, which would require $Cos(\theta_2)$ also to become larger than 1. Since this is not possible, the beam will be completely reflected. For visible light, most materials have a higher refractive index compared to air ($n_{air}=1$) which results in total internal reflection when light tries to leave a material under very small angles of incidence. The refractive index for materials in the X-ray domain is smaller than one resulting in total reflection of X-rays when X-rays tries to penetrate a material under small angles of incidence.

The refractive index for matter in interaction with X-rays is given by

$$n = 1 - \delta - i\beta \tag{2.9}$$

where δ is the dispersive component and β is related to the absorption. Because X-rays interact with the electrons l, δ and β are functions of the electron scattering factors and are given by [76,77]

$$\delta = \frac{r_e}{2\pi}\lambda^2 N_a \rho \sum_{j=1}^{N} C_j f_{1j} \tag{2.10a}$$

$$\beta = \frac{r_e}{2\pi}\lambda^2 N_a \rho \sum_{j=1}^{N} C_j f_{2j} \tag{2.10b}$$

In these equations, r_e is the classical electron radius, λ is the wavelength of the beam, N_a is Avogadro constant, ρ is the mass density and C_j is the atomic fraction of atoms in the material with electron scattering factors f_{1j} and f_{2j}.

Since the absorption is usually much smaller compared to the dispersion, absorption is often neglected. Neglecting the absorption and using the small-angle approximation for the cosine term, the critical angle can be expressed as

$$\theta_c = \sqrt{2\delta} \tag{2.11}$$

Combining equation 2.10a and 2.11 provides an expression for the mass density of the thin film that can be related to the measurement curve. Figure 12 shows three simulated curves. The black one represents the model without any absorbance. However, the absorbance reduces the ideal edge making it more difficult to directly read θ_c.

XRR also allows for measurement of the thin film roughness and thickness. More information on these topics can be found in the literature [78,79].

Scanning Electron Microscopy (SEM) and Energy Dispersive Spectroscopy (EDS)

SEM and EDS were used to analyze the microstructure and chemical composition of the coatings. An SU8000 Hitachi was used to image the coating structures. A low acceleration voltage (~1 kV in SE mode and ~2 kV in BSE mode) was used to image the microstructure without additional metallic coating. The cross-section of the coatings was analyzed using different preparation techniques. For cross-sections without surface topography, the sample was cut and afterwards polished using a cross section polisher (SM-09010, JEOL). This method allowed a clean cross-section but provides no information on the microstructure. Alternatively, a micro-crack which is generated by spontaneous cracking perpendicular to the cutting direction of the sample was analyzed under approximately 45° in SE mode to obtain information on the morphology in the cross-section.

The atomic ratio between silicon, oxygen and carbon was measured using EDS. The X-Ray penetration depth was calculated using the Andersen and Hasler approximation to ensure that only the coating was measured [19]. An acceleration voltage of 5 kV, assuming a mass density of 1.6 g/cm³, results in a penetration depth between 480 and 600 nm for analyzed elements as shown in Figure 13.

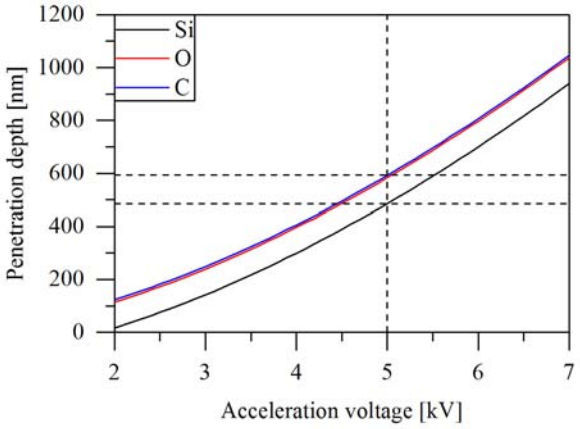

Figure 13. Penetration depth of the characteristic X-Ray as a function of the acceleration voltage. The values are calculated based on the Andersen and Hasler approximation assuming a mass density of 1.6 g/cm³.

2.5 References

[1] B.C. Zhang, R.C. Cross, Application of a toroidal plasma source to TiN thin film deposition, J. Vac. Scie. Technol. A 16 (1998) 2016–2020.

[2] X. Tian, J. Li, L. Tian, C. Gong, S. Yang, P.K. Chu, A novel technique to enhance surface properties of DLC films deposited on the inner wall of cylindrical PET barrel by DC-RF hybrid discharge, Surface Modification of Materials by Ion beams Proceedings of the 16th International Conference on Surface Modification of Materials by Ion Beams 206 (2011) 1016–1019.

[3] F. Jansen, S. Krommenhoek, Thin film deposition on inside surfaces by plasma enhanced chemical vapor deposition, Thin Solid Films 252 (1994) 32–37.

[4] F. Paschen, Bohrs Heliumlinien, Annalen der Physik 355 (1916) 901–940.

[5] J.-L. Delcroix, A.R. Trindade, in: L. Marton (Ed.), Advances in Electronics and Electron Physics, Academic Press (1974), 87–190.

[6] S. Muhl, A. Pérez, The use of hollow cathodes in deposition processes: A critical review, Thin Solid Films 579 (2015) 174–198.

[7] S. Günther, Plasma-aktivierte Bedampfung von flexiblen Materialien. Plasma-activated vapour deposition on flexible substrates, Vakuum in Forschung und Praxis 16 (2004) 6–10.

[8] R V Kennedy, Theory of the arc hollow cathode, J. Phys. D: Appl. Phys. 34 (2001) 787.

[9] C.M. Ferreira, J.L. Delcroix, Theory of the hollow cathode arc, J. Appl. Phys. 49 (1978) 2380–2395.

[10] G Stockhausen, M Kock, Proof and analysis of the pendulum motion of beam electrons in a hollow cathode discharge, J. Phys. D: Applied Physics 34 (2001) 1683.

[11] V I Kolobov, L D Tsendin, Analytic model of the hollow cathode effect, Plasma Sources Science and Technology 4 (1995) 551.

[12] B. Zimmerman, Plasmaphysikalische Charakterisierung einer magnetfeldgestützten Hohlkathoden-Bogenentladung und ihre Anwendung in der Vakuumbeschichtung. Dissertation, 2012.

[13] I. Mikkellides, I. Katz, Goebel, D and Polk, J (Eds.), Theoretical Model of a Hollow Cathode Insert Plasma, 2004.

[14] L.M. Lidsky, S.D. Rothleder, D.J. Rose, S. Yoshikawa, C. Michelson, R.J. Mackin, Highly Ionized Hollow Cathode Discharge, J. Appl. Phys. 33 (1962) 2490–2497.

[15] R.T. Downey, Theoretical and experimental investigation into high current hollow cathode arc attachment. Dissertation, 2008.

[16] H Conrads, M Schmidt, Plasma generation and plasma sources, Plasma Sources Science and Technology 9 (2000) 441.

[17] S. Klagge, A. Lunk, Probe diagnostics of anisotropic plasma in a hollow cathode arc, J. Appl. Phys. 70 (1991) 99–105.

[18] H. Morgner, M. Neumann, S. Straach, M. Krug, The hollow cathode: a high-performance tool for plasma-activated deposition, Surf. Coat. Technol. 108–109 (1998) 513–519.

[19] F. Fietzke, H. Morgner, S. Günther, “Magnetically enhanced hollow cathode—a new plasma source for high-rate deposition processes”, Plasma Process. Polym. 6 (2009) 242-246.

[20] M. Konuma, Film Deposition by Plasma Techniques, Springer Series on Atoms+Plasmas 10, Springer Berlin Heidelberg, Berlin, Heidelberg, 1992.

[21] G. Franz, Low Pressure Plasmas and Microstructuring Technology, Springer Berlin Heidelberg, Berlin, Heidelberg, 2009.

[22] F. Plais, B. Agius, F. Abel, J. Siejka, M. Puech, G. Ravel, P. Alnot, N. Proust, Low Temperature Deposition of SiO2 by Distributed Electron Cyclotron Resonance Plasma‐Enhanced Chemical Vapor Deposition, Journal of The Electrochemical Society 139 (1992) 1489–1495.
[23] W. Huang, X. Wang, M. Sheng, L. Xu, F. Stubhan, L. Luo, T. Feng, X. Wang, F. Zhang, S. Zou, Low temperature PECVD SiNx films applied in OLED packaging, Mater. Sci. Eng. B 98 (2003) 248–254.
[24] G. Suchaneck, V. Norkus, G. Gerlach, Low-temperature PECVD-deposited silicon nitride thin films for sensor applications, Surf. Coat. Technol. 142–144 (2001) 808–812.
[25] J. Friedrich, Mechanisms of Plasma Polymerization – Reviewed from a Chemical Point of View, Plasma Process. Polym. 8 (2011) 783–802.
[26] H. Yasuda, Plasma polymerization, Academic Press, Orlando, 1985.
[27] H. Drost, Plasmachemie: Prozesse der chemischen Stoffwandlung unter Plasma-Bedingungen, Akad.-Verlag, 1978.
[28] R. Morent, N. de Geyter, T. Jacobs, S. van Vlierberghe, P. Dubruel, C. Leys, E. Schacht, Plasma-Polymerization of HMDSO Using an Atmospheric Pressure Dielectric Barrier Discharge, Plasma Process. Polym. 6 (2009) 537-542.
[29] R.P. Mota, D. Galvão, S.F. Durrant, De Moraes, Mário A. Bica, de Oliveira Dantas, Socrates, M. Cantão, HMDSO plasma polymerization and thin film optical properties, 22nd International Conference on Metallurgical Coatings and Thin Films 270 (1995) 109–113.
[30] N.E. Blanchard, B. Hanselmann, J. Drosten, M. Heuberger, D. Hegemann, Densification and Hydration of HMDSO Plasma Polymers, Plasma Process. Polym. 12 (2015) 32–41.
[31] D. Hegemann, U. Schütz, A. Fischer, Macroscopic plasma-chemical approach to plasma polymerization of HMDSO and CH4, Surf. Coat. Technol. 200 (2005) 458–462.
[32] A.M. Wróbel, M. Kryszewski, M. Gazicki, Oligomeric Products in Plasma Polymerized Organosilicones, Journal of Macromolecular Science: Part A - Chemistry 20 (1983) 583–618.
[33] R. Basner, R. Foest, M. Schmidt, K. Becker, H. Deutsch, Absolute total and partial electron impact ionization cross sections of hexamethyldisiloxane, International Journal of Mass Spectrometry 176 (1998) 245–252.
[34] R. Barni, S. Zanini, C. Riccardi, Characterization of the Chemical Kinetics in an O2/HMDSO RF Plasma for Material Processing, Advances in Physical Chemistry 2012 (2012) 1–6.
[35] D.S. Wavhal, J. Zhang, M.L. Steen, E.R. Fisher, Investigation of Gas Phase Species and Deposition of SiO2 Films from HMDSO/O2 Plasmas, Plasma Process. Polym. 3 (2006) 276–287.
[36] D. Magni, C. Deschenaux, C. Hollenstein, A. Creatore, P. Fayet, Oxygen diluted hexamethyldisiloxane plasmas investigated by means of in situ infrared absorption spectroscopy and mass spectrometry, J. Phys. D: Appl. Phys. 34 (2001) 87–94.
[37] K. Li, O. Gabriel, J. Meichsner, Fourier transform infrared spectroscopy study of molecular structure formation in thin films during hexamethyldisiloxane decomposition in low pressure rf discharge, J. Phys. D: Appl. Phys. 37 (2004) 588-594.
[38] J.L. Jauberteau, I. Jauberteau, Comparison of hexamethyldisiloxane dissociation processes in plasma, The journal of physical chemistry. A 116 (2012) 8840–8850.

[39] M.R. Alexander, F.R. Jones, R.D. Short, Radio-Frequency Hexamethyldisiloxane Plasma Deposition: A Comparison of Plasma- and Deposit-Chemistry, Plasmas and Polymers 2 (1997) 277–300.
[40] P. Zhu, M. Teranishi, J. Xiang, Y. Masuda, W-S. Seo, K. Koumoto, A novel process to form a silica-like thin layer on polyethylene terephthalate film and its application for gas barrier, Thin Solid Films 473 (2005) 351–356.
[41] D.S. Wuu, W.C. Lo, L.S. Chang, R.H. Horng, Properties of SiO2-like barrier layers on polyethersulfone substrates by low-temperature plasma-enhanced chemical vapor deposition, Thin Solid Films 468 (2004) 105–108.
[42] A. Granier, G. Borvon, A. Bousquet, A. Goullet, C. Leteinturier, van der Lee, Arie, Mechanisms Involved in the Conversion of ppHMDSO Films into SiO2-Like by Oxygen Plasma Treatment, Plasma Process. Polym. 3 (2006) 365–373.
[43] A. Bousquet, V. Bursikova, A. Goullet, A. Djouadi, L. Zajickova, A. Granier, Comparison of structure and mechanical properties of SiO2-like films deposited in O2/HMDSO pulsed and continuous plasmas, Surf. Coat. Technol. 200 (2006) 6517–6521.
[44] A. Bieder, A. Gruniger, R. von Rohr, Deposition of SiOx diffusion barriers on flexible packaging materials by PECVD, Surf. Coat. Technol. 200 (2005) 928–931.
[45] P.G. Pai, Infrared spectroscopic study of SiOx films produced by plasma enhanced chemical vapor deposition, J. Vac. Sci. Technol. A 4 (1986) 689-694.
[46] D. Hegemann, U. Vohrer, C. Oehr, R. Riedel, Deposition of SiOx films from O2/HMDSO plasmas, Surf. Coat. Technol. 116–119 (1999) 1033–1036.
[47] A. Walkiewicz-Pietrzykowska, Deposition of Thin Films of SiOCH in a Surfatron Microwave Plasma Reactor with Hexamethyldisiloxane as Precursor, Chemical Vapor Deposition 11 (2005) 317–323.
[48] J. Schwarz, M. Schmidt, A. Ohl, Synthesis of plasma-polymerized hexamethyldisiloxane (HMDSO) films by microwave discharge, Surf. Coat. Technol. 98 (1998) 859–864.
[49] C. Vautrin-Ul, F. Roux, C. Boisse-Laporte, J.L. Pastol, A. Chausse, Hexamethyldisiloxane (HMDSO)-plasma-polymerised coatings as primer for iron corrosion protection: influence of RF bias, J. Mater. Chem. 12 (2002) 2318–2324.
[50] F. Garbassi, E. Occhiello, Plasma deposition of silicon-containing layers on polymer substrates, Macromolecular Symposia 139 (1999) 107–114.
[51] S. Zanini, C. Riccardi, M. Orlandi, E. Grimoldi, Characterisation of SiOxCyHz thin films deposited by low-temperature PECVD, Vac. 82 (2007) 290–293.
[52] M. Naddaf, S. Saloum, Visible photoluminescence from plasma-polymerized-organosilicone thin films deposited from HMDSO/O 2 induced remote plasma: effect of oxygen fraction, J. Phys. D: Appl. Phys. 41 (2008) 175206.
[53] P. Supiot, C. Vivien, A. Granier, A. Bousquet, A. Mackova, D. Escaich, R. Clergereaux, P. Raynaud, Z. Stryhal, J. Pavlik, Growth and Modification of Organosilicon Films in PECVD and Remote Afterglow Reactors, Plasma Process. Polym. 3 (2006) 100–109.
[54] R. Clergereaux, M. Calafat, F. Benitez, D. Escaich, I. Savin de Larclause, P. Raynaud, J. Esteve, Comparison between continuous and microwave oxygen plasma post-treatment on organosilicon plasma deposited layers: Effects on structure and properties, Thin Solid Films 515 (2007) 3452–3460.
[55] A. Mackova, V. Perina, Z. Stryhal, J. Pavlik, M. Svec, A. Quédé, P. Supiot, G. Borvon, A. Granier, P. Raynaud, The combined study of the organosilicon films by RBS, ERDA and AFM analytical methods obtained from PECVD and PACVD, Surf. Sci. 566–568, Part 2 (2004) 1143–1146.
[56] T. Fouquet, Mass Spectrometry of Synthetic Polysiloxanes: From Linear Models to Plasma Polymer Networks, ChemistryOpen 3 (2014) 269–273.

[57] A. Lefèvre, L.J. Lewis, L. Martinu, M.R. Wertheimer, Structural properties of silicon dioxide thin films densified by medium-energy particles, Phys. Rev. B 64 (2001) 115429.
[58] C. Bishop, Vacuum Deposition onto Webs, Films and Foils, 2nd edition Elsevier Science, 2011,
[59] W.C. Hendricks, P.A. Diffendaffer, in: 38th Annual Technical Conference Proceedings (1995), 134–139.
[60] M. Roehrig, C. Bright, D. Evans, in: Proceedings of the 43th Annual Technical Conference of the Society of Vacuum Coaters (2000), 335–341.
[61] W. Theiss, SCOUT Optical Spectrum Simulation, W. Theiss Hard- and Software, Aachen, 2002, http://www.mtheiss.com.
[62] B. Harbecke, Coherent and incoherent reflection and transmission of multilayer structures, Applied Physics B 39 (1986) 165–170.
[63] P. Baumeister, Optical coating technology, SPIE v. no. PM137, SPIE Optical Engineering Press, Bellingham, WA., 2004.
[64] Manual of FTIR-ATR Device, Perkin Elmer.
[65] G.L. Graff, R.E. Williford, P.E. Burrows, Mechanisms of vapor permeation through multilayer barrier films: Lag time versus equilibrium permeation, J. Appl. Phys. 96 (2004) 1840-1848.
[66] J. Angeli, A. Bengtson, A. Bogaerts, V. Hoffmann, V.-D. Hodoroaba, E. Steers, Glow discharge optical emission spectrometry: moving towards reliable thin film analysisa short review, Journal of Analytical Atomic Spectrometry 18 (2003) 670–679.
[67] R. Payling, M. Aeberhard, D. Delfosse, Improved quantitative analysis of hard coatings by radiofrequency glow discharge optical emission spectrometry (rf-GD-OES), J. Anal. At. Spectrom. 16 (2001) 50–55.
[68] V.-D. Hodoroaba, V. Hoffmann, Steers, Edward B. M., K. Wetzig, Emission spectra of copper and argon in an argon glow discharge containing small quantities of hydrogen, J. Anal. At. Spectrom. 15 (2000) 951–958.
[69] B. Fernandez, N. Bordel, C. Perez, R. Pereiro, A. Sanz-Medel, The influence of hydrogen, nitrogen or oxygen additions to radiofrequency argon glow discharges for optical emission spectrometry, J. Anal. At. Spectrom. 17 (2002) 1549–1555.
[70] 兵庫県立大学, Elemental Distribution Analysis of Lithium Ion Battery Electrodes with Glow Discharge Optical Emission Spectroscopy, 2014.
[71] F.A. Ferri, G. Malegori, M. Enachescu, M. Veis, N. Behary, P.K. Das, R. de Oliveira, T.L. Horng, V.J. Bellitto, V. Gupta, Measurement of the Nanoscale Roughness by Atomic Force Microscopy: Basic Principles and Applications, INTECH Open Access Publisher,
[72] M. Schuster, H. Goebel, C. Michaelsen, R. Bormann, X-ray analysis apparatus with a graded multilayer mirror, Patent, 2001,
[73] M. Björck, G. Andersson, GenX, J. Appl. Crystallogr. 40 (2007) 1174–1178.
[74] A.H. Compton, CXVII. The total reflexion of X-rays, Philosophical Magazine Series 6 45 (1923) 1121–1131.
[75] M. Tolan, X-ray scattering from soft-matter thin films: Materials science and basic research. Univ., Habil.-Schr. u.d.T.: Tolan, Metin: X-ray diffraction from soft-matter thin films--Kiel, 1998, Springer Tracts in Modern Physics 148, Springer, Berlin, 1999.
[76] K. Stoev, K. Sakurai, Recent theoretical models in grazing incidence X-Ray reflectrometry, The Rigaku Journal 14 (1997) 22–37.
[77] I. Kojima, L. Boquan, Structural Characterization of thin films by X-Ray Reflectivity, The Rigaku Journal 16 (1999) 31-42.

[78] J. Daillant, A. Gibaud (Eds.), X-ray and neutron reflectivity: Principles and applications, Lecture notes in physics 770, Springer, Berlin, Heidelberg, 2009.
[79] L. Spieß, G. Teichert, R. Schwarzer, H. Behnken, C. Genzel, in: Moderne Röntgenbeugung, Vieweg+Teubner (2009), 453–486.

Chapter 3

Gas barrier and chemical analysis of plasma polymeric coatings[a]

The water vapor barrier performance of thin film coatings can be quantified by their water vapor transmission rate. This chapter discusses the impact of a broad range of process parameters on the chemical structure of the coatings and relates changes in the chemical structure with the gas barrier performance of the deposited coating. The first section discusses the effect on the oxygen-to-HMDSO ratio under low and high applied plasma power settings. After concluding that the organic coatings show great potential as a gas barrier, the second

[a] *This chapter is based on the following journal publications:*

Michiel Top, Steffen Schönfeld, John Fahlteich, Sebastian Bunk, Thomas Kühnel, Steffen Straach, Jeff. Th. De Hosson (2017): Hollow-cathode activated PECVD for the high-rate deposition of permeation barrier films. In Surf. Coat. Techn. 314, pp. 155–159.

Michiel Top, John Fahlteich, Jeff. Th. De Hosson (2017): Influence of the applied power on the barrier performance of silicon-containing plasma polymer coatings using a hollow cathode-activated PECVD process. In Plasma Process Polym, 14, e1700016

section provides an in-depth discussion on the effect of the applied plasma power per unit of monomer for organic coatings on the permeation barrier properties. The mechanisms behind the water vapor barrier is exposed. The chapter finalizes with a discussion on the limitations of the hollow cathode arc discharge based PECVD as a tool for the deposition of permeation barrier coatings.

SiO_2 has been widely investigated as thin film permeation barrier to reduce the oxygen and water vapor transmission. These coatings are commonly deposited using PECVD, Electron beam evaporation or sputtering techniques. One of the main advantages of PECVD compared to sputtering is the versatility of the technique. By carefully selection of the monomer and process parameters, a coating with tailored properties can be deposited. In this thesis, the choices of monomer and reactive gas are limited to HMDSO and oxygen, respectively. This combinations allows us to deposit coatings that are partly organic up to mainly inorganic coatings. HMDSO is well-used due to its good availability and requires relative low safety precautions.

In this section, the literature review concentrates on PECVD processes based on a mixture of HMDSO and oxygen. Literature has tested these two materials in combinations with a variety of plasma sources including Radio Frequency (13.56 MHz) [1–8] or MicroWave [1,7,9–11]. Special types include a 2.5 kHz RF set-up [12] or the Pennings Discharges Plasma (PDP) source [13,14]. In order to compare the processes, two different processing parameters are defined:

$$Applied \text{ plasma } power\ per\ unit\ of\ monomer\ [\frac{W}{sccm}]$$

and

$$Oxygen\text{-}to\text{-}HMDSO\ ratio\ [-]$$

The first one directly relates to the amount of energy per HMDSO molecule whereas the second one is related to the ratio between oxygen and carbon molecules present in the deposition zone and mainly affects the organic concentration in the coating. Reducing carbon content within the coating usually leads to a change in the ratio between oxygen and silicon as was explained in chapter 2. Additionally, the process pressure and coating

thickness play an important role. The pressure range is usually optimized for the plasma source whereas the thickness is often a trade-off between process efficiency, mechanical properties and barrier properties.

The wide range of processing parameters studied in literature is illustrated in Table 1. The oxygen-to-HMDSO ratio is varied from values as low as 0.25, for highly organic coatings, to values as high as 100 for inorganic coatings. The applied power per unit of monomer is varied ranging from 2.6 W/sccm to 800 W/sccm. Pressures were reported from 1.3 up to 30 Pa. Coating thicknesses were reported between 30 and 700 nm.

This broad variation also leads to a tremendous difference in the chemical structure and thereby the improved gas barrier performance. Here, not only the coating but also the substrate material and cleanliness of the surface of the substrate play an important role that makes it even more difficult to compare different sources in literature. A convenient, even though not extensive, method for making a comparison is the so-called barrier improvement factor (BIF), which is defined by

$$BIF_{\mathrm{H_2}O} = \frac{WVTR_{coated\ substrate}}{WVTR_{bare\ substrate}}$$

The BIF represents the ratio between the coated and uncoated substrate. The barrier improvement for water vapor was measured between 2 and 160.

Table 1. Overview of the main process parameters and the range used within literature. The last column present

Processing Parameter	Range in literature	arcPECVD (in this chapter)
Applied power/unit of monomer	2.6-800 w/sccm	70 w/sccm
Oxygen-to-HMDSO Ratio	0.25-100	2
Pressure	1.3-30 Pa	< 4 Pa
Coating thickness	30-700	400 nm
BIF (H_2O)	2-160	40

The following two sections discuss the variation of the Oxygen-to-HMDSO ratio and the applied power per unit of monomer on the chemical and barrier properties for HMDSO coatings. The last section discusses the limitation of the deposition technique for barrier applications.

3.1 Effect of the Oxygen-to-HMDSO ratio

The WVTR was measured for samples with different Oxygen-to-HDMSO variations between 2 and 16 as well as for two different setting (high and low) of the applied plasma power to obtain a general overview of the promising process parameters for permeation barrier coatings. The "high power" samples were deposited using a plasma power close to the thermal limit of the substrate. Further increase in the applied plasma power lead to thermal damage of the substrate. For the "low power" samples, the current on the boosteranode was reduced down to 50% of the high power current. Detailed process parameters are given in Table 2. The range for the Oxygen-to-HMDSO ratio of 2 till 16 was chosen based on the theoretical reaction mechanisms as discussed in chapter 2.

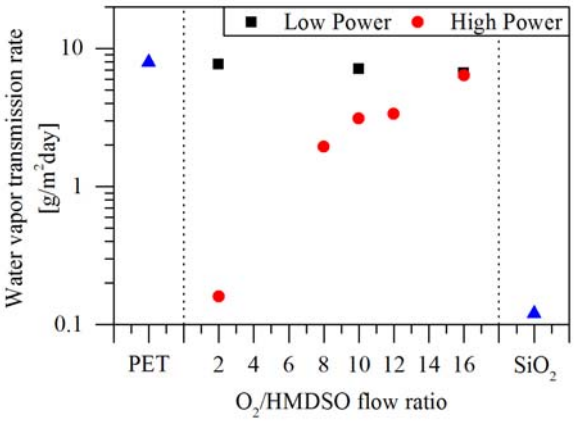

Figure 1. Measured water vapor transmission rate (in g/m²day) of the coatings as a function of the oxygen-to-HMDSO ratio. The middle part shows the PECVD coatings deposited with (black squares) low power and (red circles) high power. The blue triangles on the left and right show the WVTR of the bare substrate and sputtered SiO_2 coating, respectively.

The gas barrier results are shown in Figure 1. For the sake of reference, the blue triangles on the left and the right indicate the permeation rates of the bare substrate and sputtered SiO_2 coating, respectively. The coatings deposited with low and high plasma power have an approximate thickness of 350 and 400-450 nm, respectively. The first observation is that without sufficient power, no improved barrier performance is observed as is shown by the low power samples (black squares). This indicates that porous polymeric coatings are deposited, which provide no significant additional barrier functionality compared to the PET substrate. The high power samples, however, show a clear trend. For low oxygen flows, a major improvement was observed from 7.8 g/(m²day) of the bare substrate to 0.16 g/(m²day) of the coated substrate. However, it is rather unexpected that the organic coating shows a good barrier performance whereas the inorganic coating shows almost no improvement even though it should resemble the SiO_2 coating most.

This result clearly showed that the low power coatings show no potential as gas barrier coatings and the focus was set on the high power coatings. To obtain a better understanding of the changes in the coating, the high power coatings and the sputtered barrier coatings were analyzed in more detail.

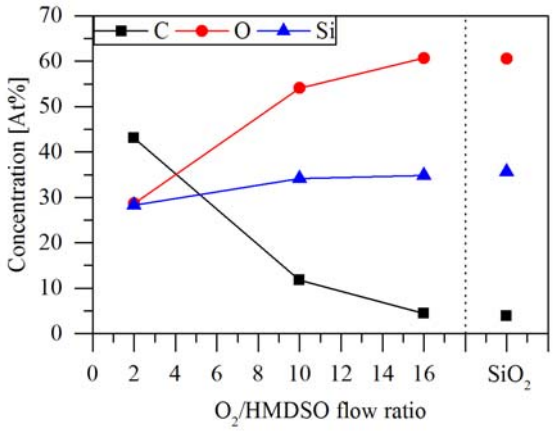

Figure 2. Measurement of the chemical composition (except hydrogen) using XPS. The results on the left show the trend for the high-power deposited PECVD coatings whereas the values right of the dotted line show the results of the sputtered reference coating.

Table 2. Deposition parameters that were used for the deposition. A range is provided for the parameters that were varied.

Processing parameter	Range
Web coater	*novoFlex® 600*
Web speed	1 m/min
Cooling drum temperature	0 °C
Argon Flow	500 sccm + 400 sccm (100 sccm through every hollow cathode)
Web tension	450 N
HMDSO flow	125 sccm
Oxygen flow	250-2000 sccm
HC Discharge Current / Voltage	100 A / 24-26 V (low power) 131 A / 24-26 V (high power)
BA Discharge Current / Voltage	17 A / 7-16 V (low power) 33 A / 17-22 V (high power)

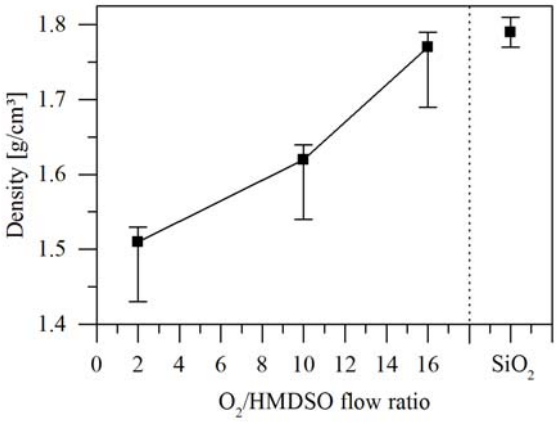

Figure 3. XRR density of the coatings as a function of the oxygen to HMDSO ratio. The „SiO_2 „-coating at the right represents the density of a sputtered SiO_2 coating for reference.

The chemical composition was analyzed using XPS. As the coatings were approximately 400 till 450 nm thick, it should be mentioned that only a small part of the coatings is analyzed. GD-OES was used to confirm that there are no compositional gradients in the coating which allows us to use the XPS data as a good approximation for the whole thickness of the coating. The XPS results agree with the initial expectations. For low oxygen flows, the coating is a $SiOC_{1.5}$ coating which gradually changes to a mainly inorganic $SiO_{1.7}$ coating for high oxygen flows.

The PECVD coating shows an almost identical composition to the sputtered coating for an Oxygen-to-HMDSO ratio of 16. As the density also plays a major role in the barrier performance [5], XRR measurements were performed to calculate the material density of the same samples. Figure 3 shows the results of the XRR measurement. To convert the measured electron density in the weight density, the chemical composition of the XPS measurements was used. As no information on the hydrogen content is known, the calculation was performed for coatings under the assumption that the coatings do not contain any hydrogen. The measurement errors towards lower values do not take only the statistical error into account but also include the effect of hydrogen incorporation. A clear trend is observed from 1.51 g/cm³ for the polymeric coating up to 1.77 g/cm³ for the inorganic coating. A slightly higher density is observed for the sputtered coating. This

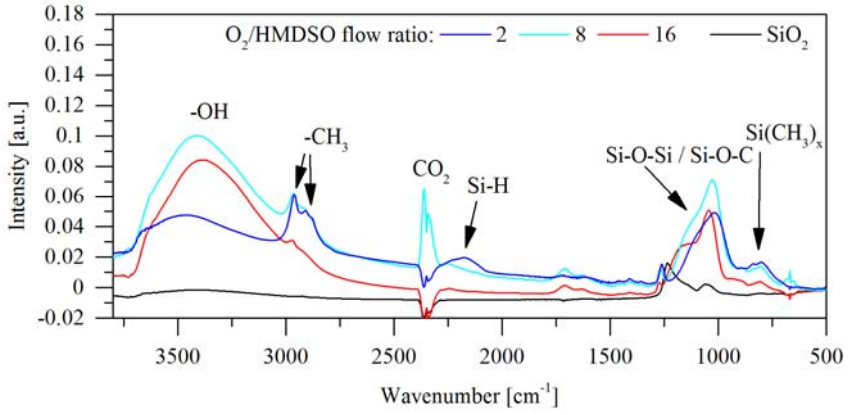

Figure 4 FTIR spectra of selected coatings. The different colors refer to the various Oxygen-to-HMDSO ratios deposited using PECVD The black line indicates the sputtered SiO_2 coating.

could be explained by the incorporation of –OH groups, which is known to induce a porosity in the coating [15,16]. It also explains the lack of barrier performance. The presence of –OH groups was confirmed by the IR spectra as shown in Figure 4 and an overview of the peaks and their corresponding groups can be found in Table 3. The black line shows the sputtered SiO_2 sample and the red line represents the absorption spectrum of the inorganic PECVD coating. The blue and light blue line represent the more organic type of coatings. The peak doublet at 2340 and 2360 cm^{-1} is related to CO_2 in the measurement chamber and was not taken into account any further. The peaks between 800 and 840 cm^{-1} as well as at 2913 and 2966 cm^{-1} show a steady decrease of the CH_x groups with increasing oxygen content. The small peaks indicate that there is still some carbon present in all PECVD coatings. The peak between 3000 and 3750 cm^{-1} that is assigned to –OH groups confirms that the coatings deposited with high oxygen flow contain a significant amount of –OH groups. The maximum peak intensity for an oxygen to HMDSO ratio of 1:8 indicates the further increase of the oxygen flow could reduce the presence of OH groups. For the organic coatings, some Si-H groups were observed as well.

Between 1000 and 1250 cm^{-1}, the sputtered SiO_2 film shows only two significant peaks at 1235 and 1050 cm^{-1}. These peaks are assigned to longitudinal and transverse optical phonon mode in an Si-O stretch, respectively [17,18]. The PECVD samples show an overlapped peak. Deconvolution using two Gaussian peaks was performed to analyze the peaks. For increasing oxygen flow, the right peak slowly shifts from 1006 cm^{-1} to 1042 cm^{-1} whereas the left peak shifts from 1086 cm^{-1} to 1150 cm^{-1}. Meanwhile, the intensity of the left peak increases compared to the intensity of the right peak. *Pai et al.* [19] also observed these peaks. They considered the left peak as a broad shoulder that increases with increasing oxygen content. The shift was related to the oxygen to silicon ratio. With less oxygen, the Si-O-Si angle changes due to a shift from SiO_2 towards SiO and thereby changes the absorption frequency. The broadening is a result of the increase in different bonding arrangements that are present within the coating. The different angles agree with the presence of $(Si\text{-}O)_n$ ring structure [20].

Table 3. An overview of the chemical groups present in the coatingand their corresponding locations.

Wave number [cm^{-1}]	Groups	Source
800 & 840	$Si(CH_3)_2$ & $Si(CH_3)_3$	[21]
1027	Si-O-Si & Si-O-C	[22]
1150	Si-O-Si	[19]
2095-2260	SiH	[23]
2340 & 2360	CO_2	[24]
2913 & 2966	CH_3	[21]
3000-3750	OH	[25]

Conclusions

The lack of barrier performance of the SiO_2 like PECVD layer was explained by the presence of CH_x and OH groups as well as presence of $(Si\text{-}O)_n$ rings. The single bond of hydrogen reduces the cross-linking of the plasma polymer which results in a lower density as compared to the sputtered SiO_2 coating whereas the larger rings create preferred permeation pathways.

The existence of barrier performance for the sample with low oxygen flow was explained by Weston [26]. The explanation was based on the idea that $(Si\text{-}O)_n$ rings, which are preferred permeation pathways, are filled up by carbon atoms. This leads to more cross-linking and increases the density of the coating. This could explain the decreasing WVTR with increasing carbon content. It should be mentioned that the explanations given for the change in chemical composition are based on simplified models that can give the reader an idea about the structure of the coating. In reality, the exact structure is far too complex and consists of a wide variety of different bonds to a higher or lesser degree.

To reduce the hydrogen content, even higher oxygen flows [11] or higher energy per unit of monomer [2,3] could be applied to reduce the hydrogen content in the coating. Within this research, the Oxygen-to-HMDSO ratio

was usually limited as the high deposition rates require significant HMDSO flow rates. The limitation was usually a result of the limitations of the flow controllers and the vacuum pump capacity.

3.2 Influence of the plasma power on the gas permeation properties of organic coatings.

As the organic coatings showed potential as barrier coatings, a thorough investigation was performed on the barrier mechanism of the silicon-containing organic barrier coatings and the effect of the applied plasma power on the barrier performance. The process parameters used during these experiments are listed in Table 4. Multiple samples were produced with a constant I_{BA} of 2.4 $A \cdot sccm^{-1}$ HMDSO. The plasma voltage was varied by both changing the magnetic field (i.e. the current through the coils) around the cathodes as well as changing the argon flow at the booster anodes.

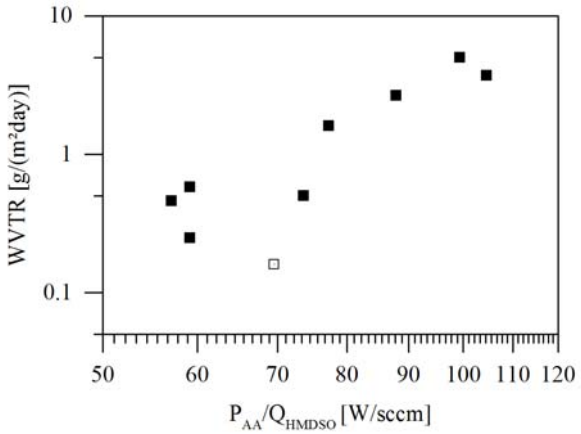

Figure 5 The WVTR (at 38 °C and 90% r.h.) of the thin films coatings is plotted as a function of the applied power between the hollow cathode and the annular anode (P_{AA})

Table 4. Deposition parameters that were used for the deposition. For parameters that were varied, the range is given.

Processing parameter	Range
Web speed	1 m/min
Cooling drum temperature	0 °C
Argon Flow	250-500 sccm + 400 sccm (100 sccm through every hollow cathode)
Web tension	450 N
HMDSO flow	125 sccm
Oxygen flow	250 sccm
Pressure	0.07-0.1 Pa
HC Discharge Current / Voltage	131 A / 23.5-30.5 V
BA Discharge Current / Voltage	33 A / 7-16 and 8-27 V

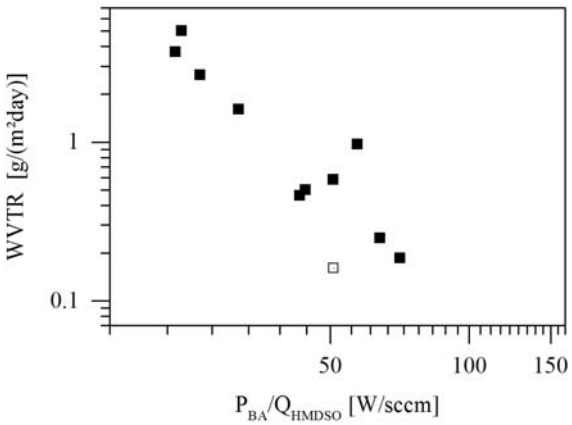

Figure 6 The WVTR (at 38 °C and 90% r.h.) of the thin films coatings is plotted as a function of applied power at the booster anode (P_{BA}). In improved permeation barrier performance is observed with increased power.

WVTR's were measured between 0.16 and 6.3 g m^{-2} day^{-1}. As the applied plasma current was kept constant, this proofed that there is no direct correlation between the applied booster anode current and the barrier performance. To analyze the relation between gas barrier properties and the applied power, the barrier performance was also plotted as a function of P_{AA} and P_{BA}. These results are shown in Figure 5 and Figure 6, respectively. The vertical axis shows the Water Vapor Transmission Rate in g m^{-2} day^{-1} (measured at 38 °C and 90% r.h.) whereas the horizontal axis presents the applied plasma power per sccm HMDSO for the annular anode and the booster anode.

An inverse relation is observed between P_{AA} and the barrier performance of the coatings whereas a direct relation is observed between the barrier performance and P_{BA}. The measured power between the hollow cathode and the annular anode mostly represents the plasma directly around the hollow cathode unit and P_{BA} mainly relates to the applied power in the reaction zone and therefore describes the plasma that directly influences the fragmentation and ionization of the monomer and reactive gas before deposition. The direct relation between P_{BA} and the barrier indicates that the dissociation of the monomer plays a dominant role.

Influence of the coating thickness

The coatings were deposited with a constant web speed of 1 m/min. Changing the applied plasma power also influenced the deposition rate and thereby lead to a small variation in the final coating thickness. The coatings discussed in this section had a thickness between 350 and 510 nm.

To exclude that the thickness influences the permeation barrier between 350 and 510 nm, single layer coatings were deposited on a PET substrate with web speeds varying between 1 and 30 m/min. The web speeds were chosen in a random order to make sure that changes in the permeation barrier were actually due to the difference in thickness and not due to any time effects. Figure 7 shows the WVTR as a function of the coating thickness. Up to 150 nm coating thickness, the WVTR steadily decreases with increasing thickness. For 150 nm and upwards, no significant changes are observed in the WVTR. This allows us to rule out any effects of the coating thickness on the permeation barrier for the coatings analyzed in this section.

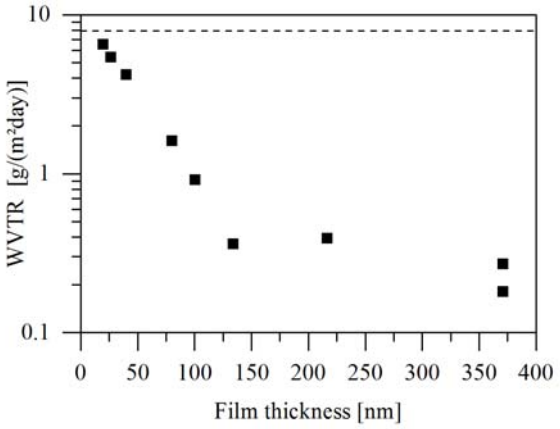

Figure 7. The water vapor transmission rate was measured as a function of the coating thickness. The dashed lines indicates the WVTR of the bare substrate.

Fragmentation of HMDSO

As the first part of section 3.2 showed that the dissociation seems to play a dominant role in the permeation performance. Mass spectrometry was used to analyze the effect of the applied plasma power on the fragments that are present in the plasma.

Figure 8 shows two typical mass spectra. One for the deposition with low (red) plasma power and one for the deposition with high (black) plasma power. The mass spectrometer was limited up to 100 atomic mass units (amu) which did not allow us to detect whether any remaining HMDSO molecules (162 amu) were present in the plasma.

For the evaluation of the spectra, the observed peaks were divided into two groups with masses below and above 50 amu as indicated by the dashed line. The first group is assigned to single molecules and small groups (e.g. O_2, Ar, C, H_2O, Si^+), which are a result of oxidation reactions of small hydrocarbon groups [21]. These molecules are wanted in the plasma to allow the formation of a dense coating. The latter group represents larger fragments which can be assigned to intermediate products of the HMDSO molecule as described in literature.[27] In our spectra, peaks were found for $SiOC_2H_8$, $SiO(CH_3)$, $Si_2O(CH_3)_4$, $Si(CH_3)_4$) and Si_2OH.

As a measure of the dissociation of the HMDSO molecule, the sum of the intensity of the molecules and fragments below 50 amu was divided by the sum of the intensities of the fragments above 50 amu. It was found that the degree of dissociation of the monomer in the mass spectrum shows a linear correlation with:

$$\frac{\Sigma \text{ Peaks } (<50 \text{ amu})}{\Sigma \text{ Peaks } (>50 \text{ amu})} \propto \left(\frac{P_{BA}}{Q_{HMDSO}}\right)^{\alpha} \times Q_{BA\,Ar} \times Q_{O_2} \qquad (3.1)$$

In this equation, P_{BA} represents the Booster Anode Power, Q represents the flows of HMDSO, the argon through the booster anode and oxygen. The measured dissociation was plotted against Eq. (3.1) in Figure 9.

The process parameters in Eq. (3.1) were compared with literature. The first part represents the applied power per unit of monomer which is consistent with the findings by Yasuda [28]. The influence of the fragmentation of oxygen was also observed by Li [29]. The increase of argon results in a higher pressure, which increases the collision rate and therefore it is thought to have a positive effect on the dissociation of the HMDSO.

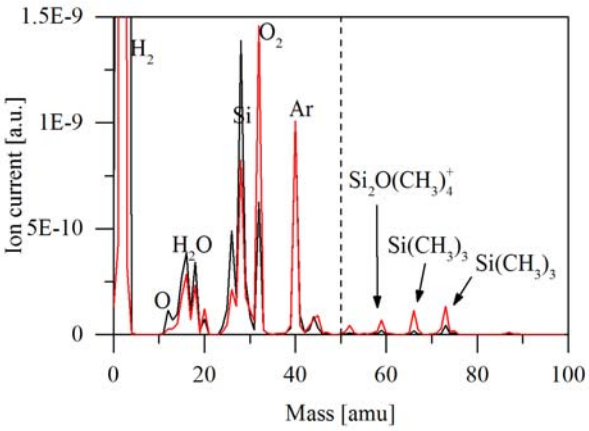

Figure 8 A typical mass spectrum for a deposition with a (red line) low power per unit of monomer and (black line) high power per unit of monomer. Peaks at the left part of the dashed line are mainly assigned to single atoms or small molecules. The peaks at the right side could be assigned to larger fragments of the HMDSO molecule. The main peaks are identified in the figure. Increasing the power reduces the number of "large fragment" within the plasma.

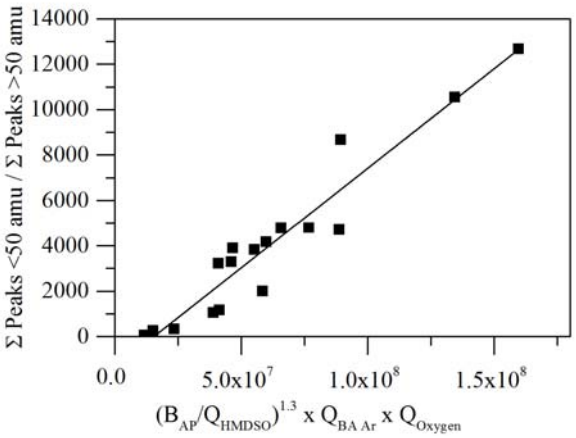

Figure 9 . The degree of fragmentation was analyzed taking the ratio between the sum of the peaks below 50 amu and the sum of the peaks above 50 amu. The dissociation was plotted as a function of several process parameters as shown in equation (2).

The value for α was chosen such that the correlation between the fit and the data points was optimized. This maximum value was found at $\alpha = 1.3$. This indicates that the power per unit of monomer has a more significant influence on the dissociation compared to the argon and oxygen flow.

Thin film analysis

So far it was shown that the increased P_{BA} results in higher dissociation of the monomer. The deposited films were analyzed to evaluate how the increased dissociation results in a better barrier performance. The thin film analysis was focused onto the samples with an HMDSO flow of 125 sccm. For higher monomer flows, the plasma power per unit of monomer was found to be not sufficient to significantly improve the barrier performance of the PET substrate. Further reduction of the monomer flow as well as further increase of the applied power was not possible because the heat transfer from the plasma into the substrate exceeded the critical thermal load of the polymer substrate.

The plasma analysis shows that the fragmentation of the HMDSO monomer increases with the applied power. XPS was used to measure the atomic weight of Si, O and C for selected samples with a WVTR between 0.16 and 5

g m^{-2} day^{-1}. All samples showed a composition with a Si:O:C contribution of 27:36:37 (± 2) at%. No correlation between the chemical composition and the WVTR was found, as shown in Figure 10. The measured variation is therefore related to variation in the coating as only a small fraction of the thickness is measured within the coating. This indicates there is no significant shift in the chemical composition (without taking the hydrogen content into account) from organic to inorganic with increasing power. Because the XPS measurement showed no changes, the relative change in hydrogen content was measured using GD-OES. The hydrogen content was normalized by

$$\frac{\int H\,[V]}{\int H\,[V]+\int C\,[V]+\int O\,[V]+\int Si\,[V]} \tag{3.2}$$

In this equation $\int X\,[V]$ represents the averaged signal in the bulk of the coating of element X. The WVTR was plotted as a function of the measured normalized hydrogen content in Figure 11. It is seen that the hydrogen content increases with increasing WVTR. One specimen which did not follow the trend is the specimen with a hydrogen signal of 0.413 V (open square). Even though it has the highest hydrogen content it shows a very low WVTR. This sample will be discussed later.

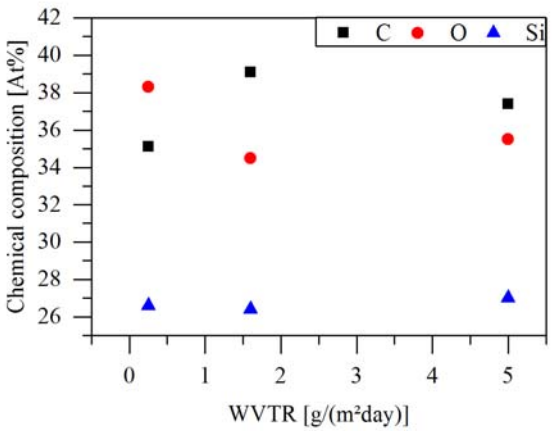

Figure 10 . The chemical composition between carbon, oxygen and silicon at a depth of 20 nm was measured using XPS shown for three samples with WVTR's between 0.1 and 5 g/(m²day). No significant changes in the chemical composition of the coatings are observed.

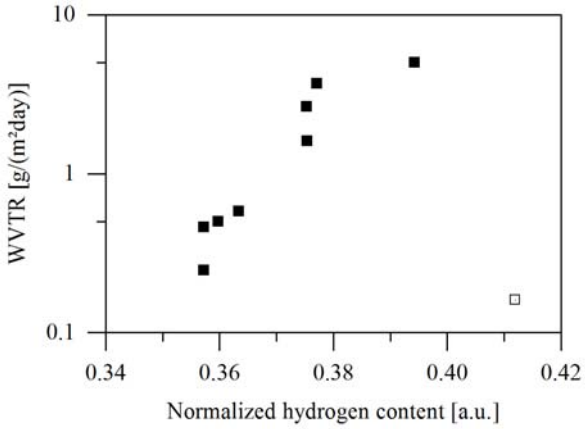

Figure 11. The WVTR (measured at 38 °C and 90% r.h.) of the thin films coatings plotted as a function of the normalized hydrogen content (equation 1) measured by GD-OES. An increase in the hydrogen content corresponds to a higher WVTR.

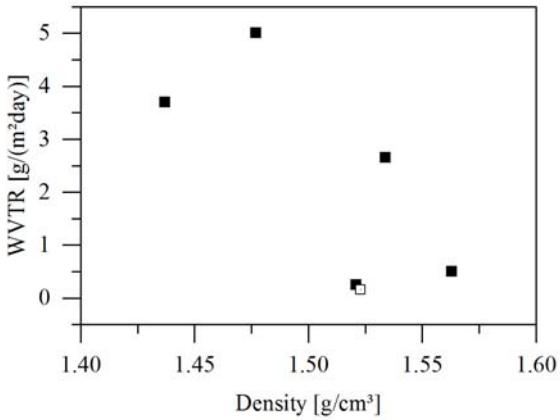

Figure 12. The WVTR (measured at 38 °C and 90% r.h.) of the thin films coatings plotted as a function of the thin film density measured using XRR.

It was described in literature that a higher mass density usually leads to an improved barrier performance [5,30]. This relation was checked by measuring the mass density of the coatings. Figure 12 shows the relation between the mass density and the WVTR. Even though there is no perfect correlation, an increased mass density indicates an improved barrier

performance. It should be mentioned that the density calculation depends on the chemical composition of the thin film. For the calculation of the mass density, the hydrogen content is not taken into account. This leads to an overestimation of the calculated density up to 0.08 $g \cdot cm^{-3}$. However, a reduction of the hydrogen content reduces the overestimation of the density. Therefore, the actual increase of the mass density with applied power could be even larger.

From the GD-OES and XRR results, it can be concluded that the lower hydrogen content increases the thin film density. The hydrogen reduction allows more cross-linking within the coating. The more dense packed molecules would result in a higher density of the film.

Our analysis up to this point shows that the increased power results in higher fragmentation of the monomer and that less hydrogen present in the deposited films improves the barrier performance. This reduction could be assigned to the reduction of either Si-H, O-H or C-H bonds in the coating. ATR-FTIR was used to analyze the influence from each of these three bonds.

Figure 13 shows the IR-ATR spectra for selected samples with the measured water vapor barrier rates between 0.16 and 6.3 g m^{-2} day^{-1}. Unless stated otherwise, the samples that are not shown showed similar trends. The numbers shown in the figure correspond to the measured WVTR of the samples. For the coated films, a broad peak is observed between 3000 and 3500 cm^{-1} which is assigned to the presence of O-H bonds [23]. The black line represents the bare PET which shows no significant increase between 3000 and 3500 cm^{-1}. Therefore, the influence of the substrate can be ignored in this domain. The differentiation between the lines lies within the measurement uncertainty and no correlation has been found between the WVTR and a change in the number of OH bonds. Figure 13 also shows peaks from 2800 till 3000 cm^{-1}. These are assigned to the C-H stretching within CH_x groups [22,31]. Unfortunately, these peaks were related to absorption in both the substrate and coating. Even though it is clear that the coating still obtains C-H bonds, no conclusions can be drawn regarding the change of these bonds in a quantitative sense.

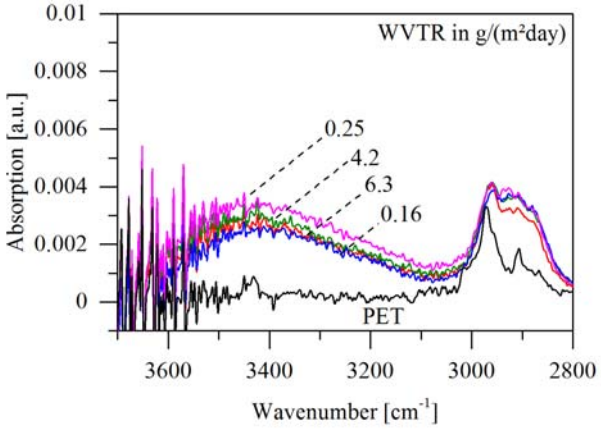

Figure 13 IR-ATR spectra between 2800 and 3700 cm-1 of several SiOx samples with WVTR's between 6.3 and 0.16 g/m²day. The black line represents the spectra of bare PET.

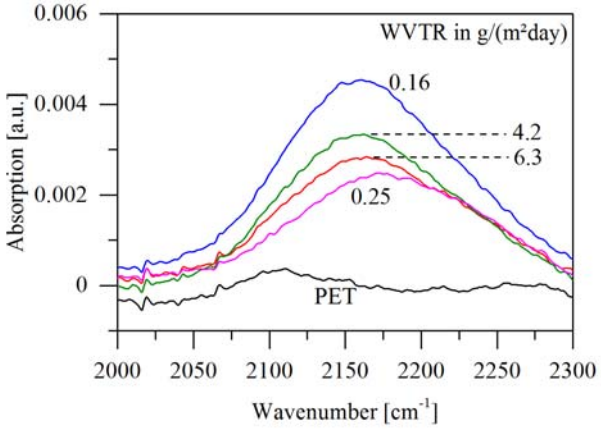

Figure 14. IR-ATR between 2000 and 2300 cm-1 spectra of several SiOx samples with WVTR's between 6.3 and 0.16 g/m²day. The black line represents the spectra of bare PET.

The domain between 2260 and 2095 cm^{-1} was analyzed for the presence of Si-H bonds [23]. Figure 14 shows this domain for the same samples as shown in Figure 13. The black line again represents the bare PET. Also in this domain, the PET does not influence the measured intensity. The numbers shown in the graph denote the measured WVTR. Some spread was found between the different samples. However, no correlation was found between the presence of Si-H bonds and the barrier performance. Therefore it is thought that the deviations are due to insignificant l variations in the coatings.

As a result, the reduction of water content should probably be assigned to breaking of Si-C and/or C-H bonds. The characterization of these bonds, which lies in the domain between 900 and 1500 cm^{-1}, was difficult because the C-H bonds which are present in the PET are interfering with the spectra of the samples. However a significant increase of a broad peak between 1000 and 1060 cm^{-1} was observed for lower water diffusion rates. This peak is related to various Si-O-Si and Si-O-C bond and stretching modes [22,31–33]. Therefore, it is most likely that the increased plasma power results in the breaking of C-H bonds in the HMDSO molecule. As a result, the Si-O-Si and Si-O-C bonds are not terminated by hydrogen groups, which allow a higher degree of crosslinking and the formation of a more dense structure improving the barrier performance. Similar relations between the plasma power and the degree of cross-linking have been found for other types of plasma polymer films [34–36].

This FTIR results are consistent with the fragmentation of HMDSO as described in literature [21,27,33]. The first dissociation steps are the removal of CH_3 groups and the breaking of Si-C bonds. The remaining $Si-(CH_x)_x$ groups are incorporated in the film. At higher power, an increasing number of C-H bonds are broken and the hydrogen may react e.g. with oxygen and is pumped away as H_2O. The reduction of hydrogen allows for a higher degree of cross-linking and therefore increases the density of the film.

One of the clear hydrogen sources is the hydrogen bound to the HMDSO. However, another imported source is water vapor outgassing from the substrate. Water vapor from the substrate film is a combination of water in the bulk as well as water molecules attached to the surface. To check the influence of these two water vapor sources, two experiments were performed.

In the first experiment, the substrate was exposed to vacuum for approximately 12 minutes to allow the water to migrate out of the substrate. In the second experiment, the substrate reel was pre-dryed over 2 months under a nitrogen atmosphere. Both experiments lead to a reduced WVTR of approximately 20 % compared to the "wet"-substrate.

Discussion and Conclusions

This section showed that for organic barrier coatings produced using a mixture of HMDSO and Oxygen, the applied power per unit of monomer is the critical process parameter. Sufficient power guarantees the complete dissociation of the molecule and leads to dense coatings that show intrinsic gas permeation barriers down to 0.16 g/(m²day) on a PET substrate. The hydrogen content in the coatings was found to play a significant role in the barrier performance.

The samples discussed in this paper were made during different deposition runs to make sure that reproduction was possible. Almost all samples are in good agreement with the proposed mechanism for improved barrier performance. One sample however deviates from this trend. This sample was indicated throughout this chapter with an open square. The sample shows a low WVTR but shows a high hydrogen signal as well as a slightly higher Si-H signal. So far, no clear explanation has been found for this specimen. Reproduction of this specific sample has not been possible up to this point.

3.3 On the limit of the improved gas barrier performance

The previous section discussed the improvement of the water vapor barrier performance as a result of the applied plasma power. The improvement was, in the end, limited due to the thermal degradation of the polymer as a result of the heat load during deposition. As the mechanism of the barrier coating was based on fragmentation of the monomer and cross-linking in the coating, it should be evaluated whether or not further increase in the applied power improves the functionality of the coating. The PET substrate (Melinex 401 CW) was replaced by a thermally more stable PEN film (Optfine PQA 1, 125 µm) to allow for further increase in the plasma power per sccm of HMDSO. Using the PEN substrate successfully allowed us to increase the power with a

factor of 2 without damaging the substrate. The WVTRs of the coatings were measured and are shown in Figure 15. The horizontal axis shows the applied power per unit of monomer whereas the vertical axis shows the permeation rate in g/(m²day). During the deposition, the web speed was fixed at 1 m/min and a HMDSO flow of 125 sccm was used. The black squares represent the WVTR's measured earlier whereas the red dots represent the samples with a PEN substrate. The first observation is that the samples in the 40-60 W/(sccm HMDSO) range show similar WVTR values. This is in contrast with sputtered coatings for which identical coating on PEN Optfine and PET Melinex show difference up to one order of magnitude [37]. The coating deposited with an applied plasma power of 120 W/(sccm HMDSO) shows an improved gas barrier performance with a WVTR as low as 0.05 g/(m²day). The trend is still going downwards which indicates that there is still room for improvement. It is also interesting to look at the open symbols. These represent the highest applied load where initial thermal degradation was observed.

This experiment proofed that further reduction of the WVTR is possible. Either the thermal heat load from the plasma on the substrate or improved heat dissipation are required to avoid thermal damage of the substrate.

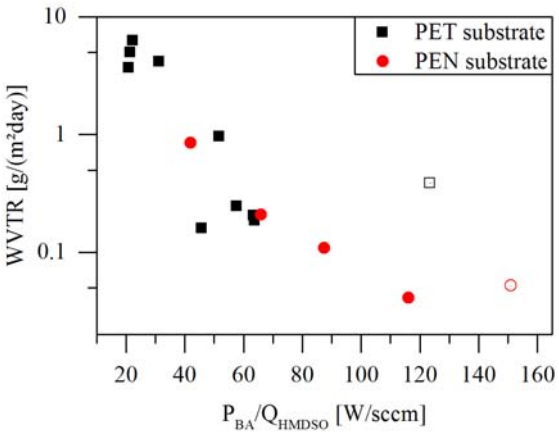

Figure 15. The WVTR of multiple coatings is shown as a function of the applied power per unit of monomer. The black squares denote the samples deposited on a PET substrate. The red circles denote the coatings deposited on a PEN substrate. The open symbols indicate the first sample with slight thermal degradation.

3.4 Conclusions

This chapter gives an extensive overview of the impact of the Oxygen-to-HMDSO ratio and applied plasma power per unit of monomer on the chemical and gas barrier properties of coatings deposited using a hollow cathode activated plasma with a separate booster. Increasing the Oxygen-to-HDMSO ratio to 16 allows for the deposition of mainly inorganic coatings similar to sputtered SiO_2 with respect to the chemical properties and mass density. FTIR reveals that the PECVD deposited coatings still contains a significant number of –OH groups compared to the sputtered coating. The resulting water vapor transmission rates are much higher compared to the sputtered SiO_2 and even approach the bare substrate. Reducing the Oxygen-to-HDMSO ratio results in an organic $SiOC_{1.5}$ coating with a 50x lower WVTR compared to the substrate.

The barrier performance for organic coatings is found to improve with plasma power. A step-by-step explanation was given of the relation between the applied plasma power and barrier performance for organic plasma polymer films. The improved barrier performance is due to the increased density of the deposited plasma polymer film. The higher density was found to be a result of the reduced hydrogen content in the films. Since the IR-ATR analysis showed no correlation between the barrier performance and the O-H or Si-H bonds, the reduced hydrogen should be a result of the reduction of C-H bonds. Therefore, sufficient power is necessary to break C-H bonds in the HMDSO molecule allowing for the formation of sufficiently dense coatings that exhibit a low WVTR.

The last part of this chapter evaluates the barrier limit of these polymeric coatings. The PET was replaced by a thermally more stable PEN to further increase the energy per HMDSO molecule. A steady increase was observed toward 0.05 g/(m²day) with no indication of any saturation effects provided that the substrate withstands the increased substrate temperature.

3.5 References

[1] A.S. da Silva Sobrinho, N. Schühler, J.E. Klemberg-Sapieha, M.R. Wertheimer, M. Andrews, S.C. Gujrathi, Plasma-deposited silicon oxide and silicon nitride films on poly(ethylene terephthalate), J. Vac. Sci. Technol. A 16 (1998) 2021-2030.

[2] M. Creatore, F. Palumbo, R. D'Agostino, Deposition of SiOx Films from Hexamethyldisiloxane/Oxygen Radiofrequency Glow Discharges: Process Optimization by Plasma Diagnostics, Plasmas and Polymers 7 (2002) 291–310.

[3] M. Creatore, F. Palumbo, R. D'Agostino, P. Fayet, RF plasma deposition of SiO2-like films: plasma phase diagnostics and gas barrier film properties optimization, Surf. Coat. Technol. 142–144 (2001) 163–168.

[4] C. Chaiwong, P. Rachtanapun, S. Sarapirom, D. Boonyawan, Plasma polymerization of hexamethyldisiloxane: Investigation of the effect of carrier gas related to the film properties, Surf. Coat. Technol. 229 (2013) 12–17.

[5] A. Bieder, A. Gruniger, R. von Rohr, Deposition of SiOx diffusion barriers on flexible packaging materials by PECVD, Surf. Coat. Technol. 200 (2005) 928–931.

[6] A. Sonnenfeld, A. Bieder, P. Rudolf von Rohr, Influence of the Gas Phase on the Water Vapor Barrier Properties of SiOx Films Deposited from RF and Dual-Mode Plasmas, Plasma Process. Polym. 3 (2006) 606–617.

[7] J. Zhang, Q. Chen, Y. Zhang, F. Liu, Z. Liu, The power source effect on SiOx coating deposition by plasma enhanced chemical vapor deposition, Thin Solid Films 517 (2009) 3850–3853.

[8] S. Zanini, C. Riccardi, M. Orlandi, E. Grimoldi, Characterisation of SiOxCyHz thin films deposited by low-temperature PECVD, Vac. 82 (2007) 290–293.

[9] S Steves, B Ozkaya, C-N Liu, O Ozcan, N Bibinov, G Grundmeier, P Awakowicz, Silicon oxide barrier films deposited on PET foils in pulsed plasmas: influence of substrate bias on deposition process and film properties, J. Phys. D: Appl. Phys. 46 (2013) 84013.

[10] K Bahroun, H Behm, F Mitschker, P Awakowicz, R Dahlmann, Ch Hopmann, Influence of layer type and order on barrier properties of multilayer PECVD barrier coatings, Journal of Physics D: Applied Physics 47 (2014) 15201.

[11] M. Deilmann, H. Halfmann, S. Steves, N. Bibinov, P. Awakowicz, Silicon Oxide Permeation Barrier Coating and Plasma Sterilization of PET Bottles and Foils, Plasma Process. Polym. 6 (2009) 695–699.

[12] L. Agres, Y. Ségui, R. Delsol, P. Raynaud, Oxygen barrier efficiency of hexamethyldisiloxane/oxygen plasma-deposited coating, J. Appl. Polym. Sci. 61 (1996) 2015–2022.

[13] J. Madocks, J. Rewhinkle, L. Barton, Packaging barrier films deposited on PET by PECVD using a new high density plasma source, Mater. Sci. Eng. B 119 (2005) 268–273.

[14] D.G. Howells, B.M. Henry, J. Madocks, H.E. Assender, High quality plasma enhanced chemical vapour deposited silicon oxide gas barrier coatings on polyester films, Thin Solid Films 516 (2008) 3081–3088.

[15] A. Brunet-Bruneau, J. Rivory, B. Rafin, J.Y. Robic, P. Chaton, Infrared ellipsometry study of evaporated SiO2 films: Matrix densification, porosity, water sorption, Journal of Applied Physics 82 (1997) 1330–1335.

[16] W.A. Pliskin, Comparison of properties of dielectric films deposited by various methods, Journal of Vacuum Science and Technology 14 (1977) 1064–1081.

[17] Burton, B. B., Kang, S. W., Rhee, S. W., S.M. George, SiO2 Atomic Layer Deposition Using Tris(dimethylamino)silane and Hydrogen Peroxide Studied by in Situ Transmission FTIR Spectroscopy, J. Phys. Chem. C 113 (2009) 8249–8257.

[18] J. D. Ferguson, E.R. Smith, A.W. Weimer, S.M. George, ALD of SiO2 at Room Temperature Using TEOS and H2O with NH3 as the Catalyst, J. Electrochem. Soc. 151 (2004) 528–535.
[19] P.G. Pai, Infrared spectroscopic study of SiOx films produced by plasma enhanced chemical vapor deposition, J. Vac. Sci. Technol. A 4 (1986) 689-694.
[20] A. Lefèvre, L.J. Lewis, L. Martinu, M.R. Wertheimer, Structural properties of silicon dioxide thin films densified by medium-energy particles, Phys. Rev. B 64 (2001) 115429.
[21] D. Magni, C. Deschenaux, C. Hollenstein, A. Creatore, P. Fayet, Oxygen diluted hexamethyldisiloxane plasmas investigated by means of in situ infrared absorption spectroscopy and mass spectrometry, J. Phys. D: Appl. Phys. 34 (2001) 87–94.
[22] D.S. Wavhal, J. Zhang, M.L. Steen, E.R. Fisher, Investigation of Gas Phase Species and Deposition of SiO2 Films from HMDSO/O2 Plasmas, Plasma Process. Polym. 3 (2006) 276–287.
[23] S. Holly, P. Sohár, L. Láng, Absorption spectra in the infrared region, Akadémiai Kiadó, Budapest, 1977.
[24] A. Oancea, O. Grasset, E. Le Menn, O. Bollengier, L. Bezacier, S. Le Mouélic, G. Tobie, Laboratory infrared reflection spectrum of carbon dioxide clathrate hydrates for astrophysical remote sensing applications, Icarus 221 (2012) 900–910.
[25] R. Reuter, K. Rügner, D. Ellerweg, de los Arcos, Teresa, A. von Keudell, J. Benedikt, The Role of Oxygen and Surface Reactions in the Deposition of Silicon Oxide like Films from HMDSO at Atmospheric Pressure, Plasma Process. Polym. 9 (2012) 1116–1124.
[26] G.F. Weston, A paper in our education series: The theory and practice of vacuum science and technology in schools and colleges, Vacuum 25 (1975) 469–484.
[27] R. Basner, R. Foest, M. Schmidt, K. Becker, H. Deutsch, Absolute total and partial electron impact ionization cross sections of hexamethyldisiloxane, International Journal of Mass Spectrometry 176 (1998) 245–252.
[28] H. Yasuda, Plasma polymerization, Academic Press, Orlando, 1985.
[29] K. Li, O. Gabriel, J. Meichsner, Fourier transform infrared spectroscopy study of molecular structure formation in thin films during hexamethyldisiloxane decomposition in low pressure rf discharge, J. Phys. D: Appl. Phys. 37 (2004) 588-594.
[30] D.S. Wuu, W.C. Lo, L.S. Chang, R.H. Horng, Properties of SiO2-like barrier layers on polyethersulfone substrates by low-temperature plasma-enhanced chemical vapor deposition, Thin Solid Films 468 (2004) 105–108.
[31] S. Saloum, M. Naddaf, B. Alkhaled, Properties of thin films deposited from HMDSO/O2 induced remote plasma: Effect of oxygen fraction, Vac. 82 (2008) 742–747.
[32] Y.-B. Park, S.-W. Rhee, Microstructure and interfacial states of silicon dioxide film grown by low temperature remote plasma enhanced chemical vapor deposition, J. Appl. Phys. 86 (1999) 1346–1354.
[33] Min Tae Kim, Deposition behavior of hexamethydisiloxane films based on the FTIR analysis of Si–O–Si and Si–CH3 bonds, Thin Solid Films 311 (1997) 157–163.
[34] L. Denis, F. Renaux, D. Cossement, C. Bittencourt, N. Tuccitto, A. Licciardello, M. Hecq, R. Snyders, Physico-Chemical Characterization of Methyl Isobutyrate-based Plasma Polymer Films, Plasma Process. Polym. 8 (2011) 127–137.
[35] D. Hegemann, E. Körner, N. Blanchard, M. Drabik, S. Guimond, Densification of functional plasma polymers by momentum transfer during film growth, Appl. Phys. Lett. 101 (2012).

[36] S. Ligot, E. Bousser, D. Cossement, J. Klemberg-Sapieha, P. Viville, P. Dubois, R. Snyders, Correlation Between Mechanical Properties and Cross-Linking Degree of Ethyl Lactate Plasma Polymer Films, Plasma Process. Polym. 12 (2015) 508–518.
[37] J. Fahlteich, S. Mogck, T. Wanski, N. Schiller, S. Amberg-Schwab, U. Weber, O. Miesbauer, E. Kucukpinar-Niarchos, K. Noller, C. Boeffel, The Role of Defects in Single- and Multi-Layer Barriers for Flexible Electronics, Proceedings of the annual technical conference- Society of Vacuum Coaters (2014) 403–413.

Chapter 4

Mechanical characterization of highly curved coated polymer substrates[a]

Just as challenging as the thin film deposition is the characterization of these thin coatings itself. One of the relevant issues in thin film characterization is the mechanical characterization of thin hard coatings on soft substrates. To explain the degree of complexity, it was chosen to dedicate a separate chapter to the work done on the qualification of several characterization methods.

The first part of this chapter deals with the accurate measurement of the residual stress of coatings on soft and rather thin substrates, which usually show much larger curvatures compared to classically coated silicon wafers. The second part deals with the mechanical characterization of the hard coatings (>10 GPa) on compliant polymeric substrates (< 5 GPa). The difficulty in measuring thin film coatings is explained more thoroughly. Afterwards, four characterization approaches are examined and the results are compared.

---

[a] *A part of this chapter is based on the following journal publication:*

Michiel Top, Guus Mulder, Nicole Prager; John Fahlteich, Jeff Th. M. De Hosson, (2018): Effect of humidity on the residual stress in silicon-containing plasma polymeric coatings. In Surface and Coatings Technology 347, pp.46–53. DOI: 10.1016/j.surfcoat.2018.04.066.

4.1 Curvature measurements

A material system always tries to reach the state of lowest total stress. Therefore, residual stress may lead to irreversible bending of coated substrates as both the coating and substrate try to obtain their lowest stress state. Measurement of the substrate curvature is often done using profilometry or white light interferometry. These techniques can measure small deflections of the samples with extremely high precision and are very useful and well applied for samples with low curvature (i.e. having a large radius of curvature). However, for thicker hard films on a thin soft substrate, the residual stress result in curvature that is usually much larger (i.e. much smaller radius of curvature) and thereby exceeds the vertical measurement range of the mentioned devices making them not applicable.

(a)

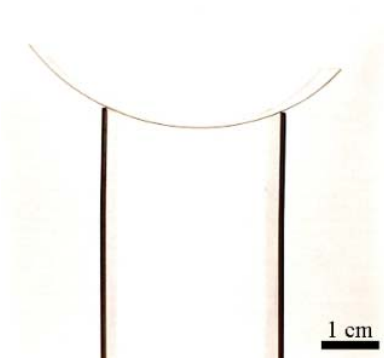

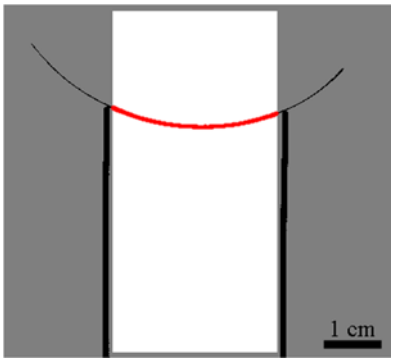

(b) (c)

Figure 1 (a) Picture of the curvature measurement setup. (b) Image taken with the build-in microscope of a specimen. (c) Image after processing in imageJ. The white area indicates the region of interest. The red-line indicates the circular fit.

A photographical measurement that directly measures the curvature is considered to be more effective for specimen with small bending radii (high curvature). Within this thesis research, a simple set-up was designed and build to obtain reliable optical images of the sample curvature. A picture of the measurement setup is shown in Figure 1a. The specimen holder on the left consists of two thin metal plates to minimize the contact between sample and holder and allows the sample to deform freely. The camera at the right side of the picture was used to take an image as shown in Figure 1b. The distance between the camera and specimen holder was 40 cm. The distance was maximized to avoid any optical distortion but short enough to fit it on a table. After processing the image to a macro script in Fiji [1], the curvature was optically measured by fitting a circle with radius r through the specimen as is shown in Figure 1c. The bright area represents the area used for fitting and the red line represents the fit.

Several external effects and measurement errors were identified and their effects are discussed in the following sections.

Effect of gravity

The specimen area between the two sample holders is larger compared to the outer area. Thus gravity pulls more at the inner part of the specimen. Depending on the position of the specimen, this leads to an under- (for the "u"-concave position) or overestimation (for the "n"-convex position) of the radius as is illustrated in Figure 2.

The effect of gravity was estimated using specimen with a radius of curvature between 25 and 250 mm. The specimens were both measured four times in "u"-concave position and 4 times in "n"-convex position. The average and standard deviation were calculated. All values in "n"-convex position showed a larger radius compared to concave "u", which agrees with the theory as described above. The deviation between the average and the "u" and "n" positions $((u - n)/2)$ as a percentage of the average radius are shown as a function of the average radius $((u + n)/2)$ in Figure 3.

The results show almost no effect for the highly curved specimen but show an increasing effect at larger radii. The increase of the difference was unexpected because a smaller radius leads to a larger mismatch ratio between the material inside and outside of the specimen holders. As the highly

Figure 2. Schematic representation of both sample position. In the "u" concave position, the radius is underestimated due to the gravity that pulls at the specimen. The radius is overestimated for the "n" convex position.

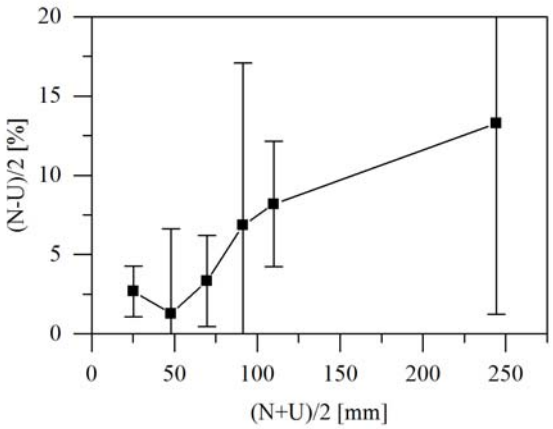

Figure 3. The deviation between the average and the "u" and "n" positions $((u-n)/2)$ as a percentage of the average radius is shown as a function of the average radius $((u+n)/2)$.

curved specimen tend to be much less flexible compared to the low stress sample, the main mechanism is thought to be gravity-induced deformation. Nonetheless, there is no reason to assume that the pulling force is higher in "u" or "n"-position, which allows us to use the average of both measurements. Therefore the average was taken in order to correct for the influence of gravity.

Error sources

To make sure that the measurements are reproducible and to have a good discussion on the significance of the measurements, a proper error analysis was made. Three different error sources were identified and analyzed:

1 Variation between specimen (*Specimen variation)*

2 Errors due to positioning of the specimen on the specimen holder *(Mounting error)*

3 Errors due to the variation in the images and the accuracy of data processing. *(Calculation error)*

An experiment was designed to calculate the contribution of each of the error sources. 15 specimen were prepared under constant plasma conditions. Measuring these 15 specimen and calculating the error distribution gives us the total measurement error. Additionally, 1 specimen was measured 15 times. During each measurement, the sample was removed and replaced on the sample holder to include both the error due to positioning of the sample and the error within the data analysis (2 and 3). For the last measurement, the same sample was measured 15 times without touching the sample. Between each measurement, the light was turned off and on to solely measure the impact of the camera quality and the data processing (3).

The result of these measurements is shown in Figure 4. The measurements were performed on highly curved (R = 26 mm) samples and low curved (R = 290 mm) samples. The different curvatures were tuned by variation of the coating thickness. The written numbers represent the error as a percentage of the radius. The highly curved specimen shows a rather small error of 0.4% for both the mounting and calculation error. The specimen variation is mainly responsible and contributes to the total error with 1.8%. This leads to a total error of 2.6%. For the sample with R = 290 mm, the calculation error was equally large as the combined mounting and calculation error. This indicates that the calculation error is mainly responsible. The calculation error of 6.3% is already much higher compared to the total error of the highly curved specimen. This was related to the resolution of the camera system: the sample shape is fitted to an arc with radius R. For large radii, the height of the arc, which is analyzed, is only 7-8 pixels compared to a line thickness around 2-3 pixels. This small difference limits the accuracy of the fit and is the main limitation for low curved samples. The high specimen variation is related to the sample deformation as was discussed in the previous section and causes a deviation of the perfect spherical shape. The total error of 12.3% limits the application and clearly shows that the measurement method is mainly suited for highly curved samples.

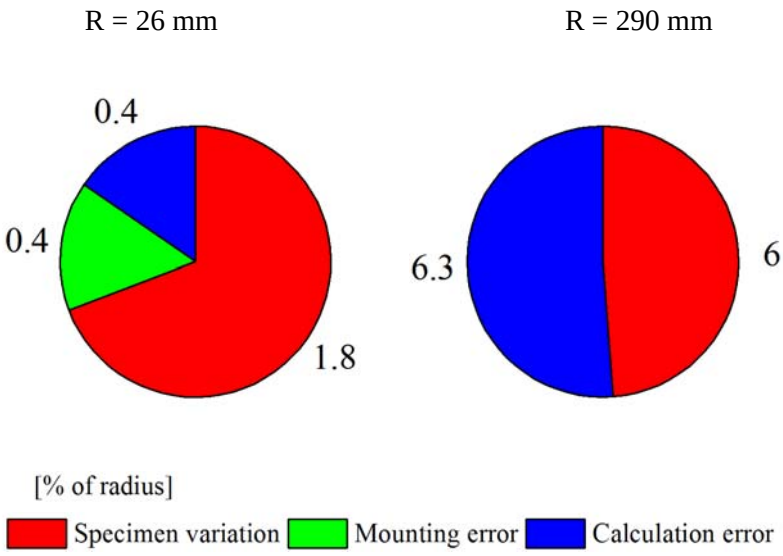

Figure 4. Different error sources contributing to the total error for (left) high curvature and (right) low curvature. The error contribution values are written as a percentage of the measured radius.

Error due to coating thickness gradient

Converting the curvature into a residual stress requires information about the coating thickness. Within this research, the coating thickness is calculated as an average in the center of the sample using the optical transmission model. It should however be taken into account that this is only an average as the coating thickness may vary across the web. An exact map of the coating thickness on the 6x6 cm sample can be measured using Hyperspectral Imaging (HSI) [2]. This high-resolution spectrometer technique can be used to find gradients in the coating thickness. Figure 5 shows the HSI results for 5 line scans along the transverse web direction (TD). The scans were taken at 10 mm distance in the machine direction of the substrate (MD). The coating shows no deviation in MD. Intermediate measurement at 250 µm distance-intervals (not shown here for clarity) show no deviation in MD as well. This indicates that the coating shows no variation over time at these length scales. An asymmetric thickness profile is present in TD. This can be explained by the asymmetric geometry of the deposition chamber. The vacuum pumps are located on one side of the deposition chamber (PS) which results in an asymmetrical gas flow along TD within the vacuum chamber and thereby

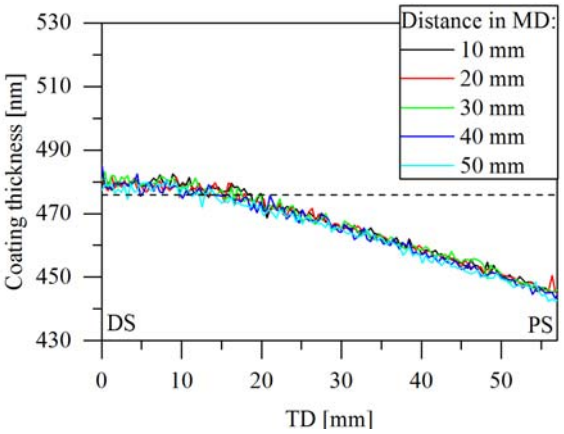

Figure 5. Left) The coating thickness calculated using HyperSpectral Imaging. The lines represent scans along TD at 5 different positions along MD. The dashed line indicates the nominal value measured using the large spot spectrometer.

influences the local deposition rate. The stress of the arithmetic average thickness is 465 nm whereas the thickness measured using normal spectroscopy was 476 nm. As this is only a minor difference of 2% it was neglected in further investigations.

4.2 Extensions of the Stoney equation.

The substrate curvature can be correlated to the thin film stress using a thin film stress model. Literature shows a large number of different models. More simple models are restricted by various assumptions whereas more complicated models are usually valid in a wider range. The latter models require more input parameters and therefore a better knowledge of the sample properties. The simplest and most well-known model was published already in 1909 by Gerald Stoney [3] and is known as the Stoney equation, which relates the stress and curvature by

$$\sigma_S = -\frac{E_S h_S^2}{6 h_c}\left(\frac{1}{R}\right) \tag{4.1}$$

where E_s and h_s are the Young's modulus and thickness of the substrate and h_c is the thickness of the coating. R denote the radius of curvature. Even though the Stoney equation is widely applied in literature, there are some very strict requirements that limit the application of the Stoney equation.

The Stoney equation was originally derived using classical beam theory and thereby only considers one dimension bending and neglects any shear stresses in the sample. Timoshenko suggested to replace the Young's modulus (E) by the bi-axial Young's modulus $E^* = E(1-\nu)$ [4]. This allows us to work with bi-directional curvature even though the expression remains limited to very small deformations. Bi-directional bending usually leads to warping of the substrate and requires the usage of shear components. Masters et al.[5] discussed the necessity of mid-plane shear components for samples which have a surface profile that is described by

$$w(x,y) = \frac{1}{2}(ax^2 + by^2) \tag{4.2}$$

Where a and b correspond to the curvature in the x and y direction, respectively. They found that the shear components need to be included when a and b are non-zero. As the optical curvature measurements only allows a reliable measurement of the radius if there is no curvature in the camera direction, the measurements are always measured as such that the displacement field is measured in the x-direction with a being non-zero (perpendicular to the field of view of the camera) and $b \to 0$ (parallel with the field of view of the camera). This allows us to neglect the mid-plane shear component of the stress.

Table 1. Mechanical properties used for the stress calculation. The substrate values are given for both the machine and transverse direction which are different as a result of the anisotropy in the substrate.

Property	Value	Method / Source
Young's modulus substrate (Es) (MD/TD)	3.6 / 4.6 GPa	Uniaxial elongation test
Poisson ratio substrate (ν_s)	0.35 ± 0.08	Literature[6]
Poisson's ratio coating (ϑ_c)	0.3	Literature[7,8]
Substrate thickness (hs)	75 µm	Product specifications
Coating thickness (hc)	100-1000 nm	Optical simulation of visible light transmittance

The most stringent requirement of the Stoney equation concerns the thickness ratio between the coating and the substrate. For oxide coatings on polymeric films, the thickness of the substrate has to be at least a 1000 times thicker compared to the thickness of the coating [9]. As this is not the case within this research, additional terms are required. Extensions of the Stoney model were developed by Röll [10], Timoshenko [4] and Inoue that provide us with a more general relation between stress and curvature.

Benabdi and Roche [11] published an overview of the different models and successfully related the different models to each other.

The most general equation (which was also described by Inoue) is given by

$$\sigma_c = -\frac{E_s h_s^2}{6h_c(1-\nu_s)R} \times \frac{1}{(1+\alpha\beta)} \times [1+\beta(4\alpha-1) + \beta^2[\alpha^2(\beta-1)+4\alpha+\frac{(1-\alpha)^2}{1+\beta}]] \quad (4.3)$$

With $\beta = h_c/h_s$ and

$$\alpha = \frac{E_c(1-\nu_s)}{E_s(1-\nu_c)} \quad (4.4)$$

This equation consists of the Stoney equation (red), a correction for the in-plane deformation of the substrate (green) and first and second order terms (blue and orange) for the effect of the coating thickness. The impact of these correction factors was calculated for the highest values of α and β used in this thesis research. Using the values given in Table 1, β stays below $1/75$ and α takes values not higher than 8. Using these values to calculate the first and second order term for the effect of the coating thickness returns maximum values of 0.25 and 0.0033 for the first and second order terms, respectively. Therefore, the first order terms were taken into account but the second order terms were ignored. The correction for the in-plane deformation returns a value of 0.9 and therefore was also included. This gives us a final expression for the residual stress:

$$\sigma_c = -\frac{E_s h_s^2}{6h_c(1-\nu_s)R} \times \frac{1}{(1+\alpha\beta)} \times [1+\beta(4\alpha-1)] \quad (4.5)$$

4.3 Quantitative evaluation of the Young's modulus[a]

Section 4.2 discussed the model required for the residual stress calculation based on curvature measurement. One of the input parameters that was not extensively discussed is the Young's modulus of the coating. The Young's modulus was classically defined as the ratio between uniaxial tensile stress σ and the uniaxial strain ϵ by

$$E = \sigma/\epsilon \tag{4.6}$$

As classical strain experiments cannot be applied to thin coatings on thick substrates, nanoindentation is often used as an alternative to measure the Young's modulus of thin film materials. The model of Oliver and Pharr [12] describes a method to calculate the Young's modulus based on the elastic response of the unloading curve during an indent. As the original model assumes purely elastic deformation during unloading of a semi-infinite bulk material, there are strong limitations regarding the application of nanoindentation for thin film coatings. As a rule of thumb, the indentation depth should not exceed 10% of the coating thickness to avoid significant influence of the substrate [13]. This is widely simulated using finite element models and is generally valid for compliant coatings on hard substrates. However, it was shown that measurements of hard coatings on compliant substrates already show substrate effects for indentation depths as low as 2% [14,15]. The influence of the substrate creates strong limitations to the allowed indentation depths. For very low indentation depths, the resolution of the indentation equipment limits the measurement accuracy but also requires a more detailed understanding of the contact mechanics between the tip and sample, which is still not completely understood.

Figure 6 shows a schematic representation of a cross-section of the coating to illustrate the challenges of nano-indentation on thin film coatings. Section (c) corresponds to the section where the substrate influences the measurement and should therefore be avoided during nano-indentation experiments.

[a] *The work in this section was greatly supported by Jaroslav Lukes (Bruker) and Malgorzata Kopycinska-Müller (Fraunhofer IKTS).*

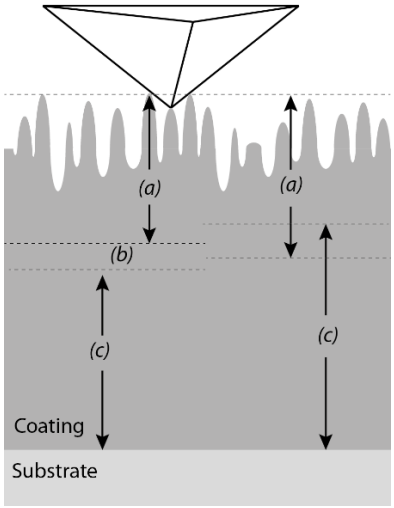

Figure 6. Schematic cross-section of the thin film coating. The different sections are with respect to the indentation depth. Section (a) in mainly influenced by the coating roughness whereas section (c) is influenced by the substrate. Section (b) can be used to measure the Young's modulus using classical nanoindentation but is not always present as (right side) section (a) and (c) may overlap.

Avoiding substrate effects requires a reduction of the indentation depth (<50 nm). At these low indentation depths it has to be taken into account that the Hertzian contact model does not provide an accurate description of the tip-sample interaction as surface roughness influences the actual contact error (Section (a)). The roughness reduces the actual contact between coating and indenter and leads to an underestimation of the measured Young's modulus. Apart from roughness effects, the macroscopic assumption of the tip-shape is usually not valid and a proper understanding is required to make sure that a good approximation of the actual contact area is available.

Applying nanoindentation on thin stiff plasma polymer coatings on soft polymer substrates still poses a big challenge and requires deep understanding of the indentation mechanism. This section discusses classical nanoindentation of PECVD deposited coatings and evaluates alternative experimental methods to measure the Young's modulus. To compare these characterization methods, several organic coatings were deposited under constant plasma conditions with different thicknesses (150 2600 nm) and surface roughness by variation of the web speed between 0.1 and 2 m/min.

4.3.1 Continuous Stiffness Measurements

Continuous Stiffness Measurements (CSMs) were performed using a Nano Indenter XP (MTS) equipped with a Berkovich-indenter. Here, a classical indentation is imposed with a harmonic oscillation. More information can be found in a review paper by Xiaodong et al. [16]. CSM allows the calculation of the Young's modulus as a function of depth. For each sample, approximately 25 measurements were taken. If not mentioned otherwise, the average values and standard deviation are given in this thesis. The load was applied to keep the strain rate constant at 0.05 s^{-1}. During the loading, a harmonic oscillation with 45 Hz was added for the CSM. Before and after every sample, indentations were made in a quartz reference sample to check whether the tip was damaged or contaminated during the measurement.

The indentation curves of the 160 and 2650 nm coatings are shown in Figure 7. Figure 7a (160 nm thick coating) shows severe plastic deformation. Apart from a slightly increased load, the response of the sample is mainly dominated by the substrate as shown in Figure 8. The red indentation curve was made on the uncoated substrate and shows an almost identical response as the substrate that is coated with the 160 nm thick coating. Figure 7b shows a mainly elastic behavior as the unloading curve almost overlaps with the loading curve. The increasing maximum load for a similar indentation depth already indicates a much higher hardness and modulus compared to substrate.

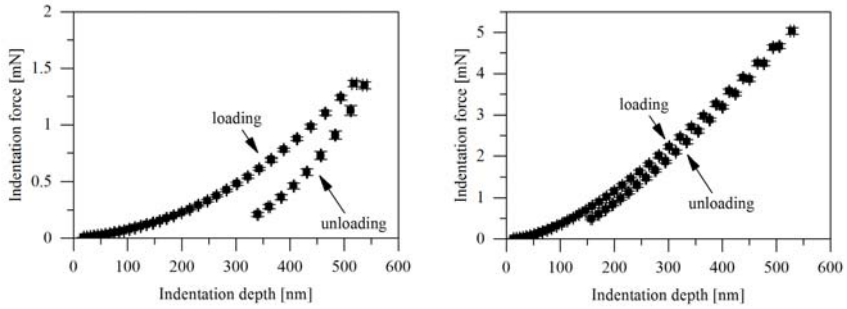

(a) (b)

Figure 7. Load-displacement curves of a (a)) 160 nm and (b) 2650 nm thick coating on 75 µm PET Melinex. Please note the different scales on the y-axis.

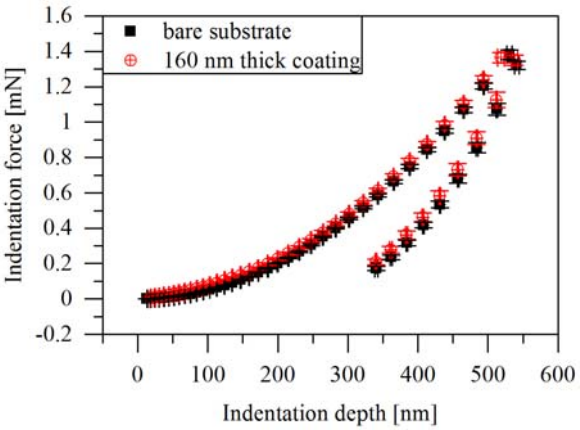

Figure 8. Indentation in Melinex 401 CW Substrate and the 160 nm thick coating.

Figure 9 shows the results of the CSM measurements. The different lines correspond to different thicknesses and the error is calculated based on the standard deviation of 25 different measurements. The bare substrate shows a constant hardness of 0.33 GPa and a Young's modulus of 3.5 GPa. The 160 nm thick coatings shows a steep decrease and approaches the substrate modulus rather fast. The hardness curve of the 640 nm thick coating also shows an overall decrease but seems to stabilize at indentation depths below 100 nm. The thicker coatings stabilize around 3 GPa as well. This is a good indication that the hardness can be estimated for coatings with a thickness larger than 600 nm. However, all measurement curves of the Young's modulus directly decrease towards the Young's modulus of the substrate. Up to at least 2.6 µm coating thickness, no stable plateau was formed that allows for the calculation of the Young's modulus. This is in agreement with Pelegri et al. [14] who stated that a measurement of a hard coating on a compliant substrate is already influenced by the substrate for indentation depths around 2% of the total coating thickness. This would require an indentation depth below 52 nm for the 2.6 µm thick coating. At this depth, the surface roughness starts playing an important role and may falsify the effective contact area as was shown in Figure 6.

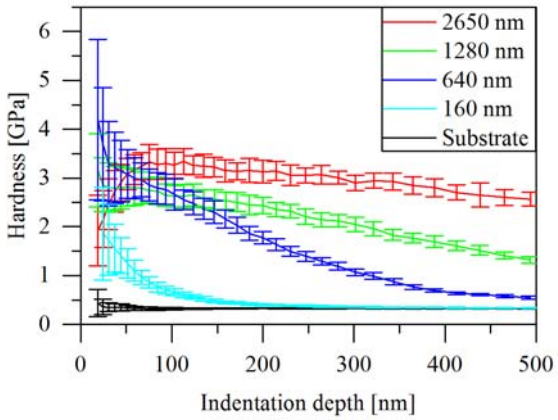

(a)

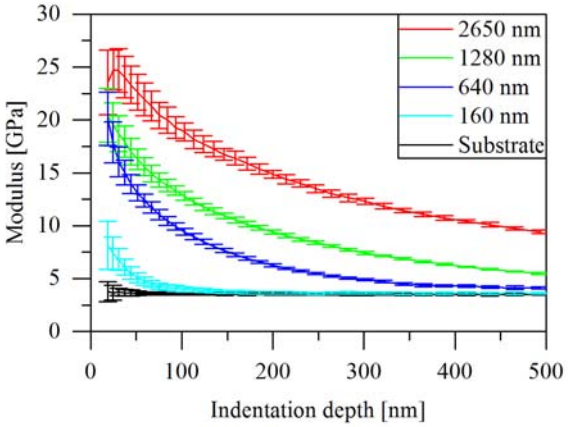

(b)

Figure 9. The graphs show the (a) hardness and (b) Young's modulus results of the CSM measurements for different coatings thicknesses as well as the bare substrate. The coating thickness is shown in the upper right corner. The left picture shows the evaluated hardness and the right picture shows the evaluated Young's modulus.

4.3.2 Peak Force Quantitative Nanomechanical Mapping

As no section (b) (see Figure 6) exists in the samples discussed in this thesis, an alternative measurement technology is necessary. This section applies Peak Force Quantitative Nanomechanical Mapping (PF QNM) [17]. PF QNM is available at Atomic Force Microscopes (AFM) type Multimode (Developed by Bruker).

PF QNM combines the high resolution and sharp tip of an AFM with mechanical characterization at very small indentation depths. The high lateral resolution allows for direct measurement within section (a) as the topological information is used for corrections of the surface roughness [18]. More information about PF QNM can be found in [17]. PF QNM measures the force interaction between the tip and sample to calculate the Derjaguin-Muller-Toporov (DMT) modulus of the sample. The DMT modulus is an extension of the Hertzian contact model by assuming the elastic contact of two spheres. They added an additional component to correct for the adhesion forces between the two bodies.

Several authors already investigated the reliability of PeakForce QNM for selected samples. Dokukin and Sokolov [19,20] investigated the influence of the tip radius while measuring bulk polymers (with Young's moduli between 0.6 and 2.8 GPa). They found large discrepancies between the Young's moduli measured using PF QNM and the bulk reference moduli. However, they demonstrated that, at least for their samples, quantitative agreement with the bulk moduli could be obtained using a rather blunt probe and the Johnson-Kendall-Roberts (JKR) model. Young et al. [21] also discussed measurements on polymers. They found that a proper calibration with a reference sample close to the actual modulus of the measured sample is required to obtain reliable and reproducible results.

For the experiments in this research, PF QNM measurements were performed using a BRUKER Multimode 8 PeakForce AFM. A silicon tip (RTESPA-525 Tip, Bruker) was used as recommended by BRUKER for samples with an estimated modulus between 1 and 20 GPa. These tips have a nominal tip radius of 8 nm, which allow indentation measurements at high lateral resolution. A scan area of 500 x 125 nm was used with a resolution of 128 x 32 measurements at a scanning rate of 0.5 lines per second. The number of indents was chosen in such a way that the wear of the tip was

minimized while maintaining sufficient information on the surface topography. The maximum tip force was fixed to make sure that the tip deflection is 5 nm (as recommended by the manufacturer). Bruker Scanasyst [22] was used to control the remaining feedback parameters. The samples were glued onto steel discs from Bruker using a 2-component adhesive. Before each measurement, the tip was calibrated on Highly Oriented Pyrolytic Graphite (HOPG) with a nominal modulus of 18 GPa. After the measurements on the actual sample, the HOPG sample was measured again to check for any damage or wear of the tip during the measurements.

The AFM measurement has an advantage over classical indentation that the mechanical data and the surface topography at the exact same position are available. Figure 10 shows the results of the topography (a) and the modulus (b) measurements. The resolution of the topography image is limited due to dulling of the tip but is still very useful in the discussion and validation of the mechanical properties.

The topography resembles the well-known cauliflower like structure whereas the modulus map looks like an inverted cauliflower structure with low modulus cusps and a connected high-modulus network. As the features in the topography and modulus map are similar in size this strongly indicates that the mechanical measurements are influenced by the surface topography.

To confirm the correlation between microstructure and measurement moduli, the boundaries between the nodular structures were identified using a gray level watershed algorithm in Fiji [1]. The height map is converted into a gray level image where the z-scale is indicated by the gray level. The watershed algorithm “floods” the image starting at very light colors (low z-values) and step by step includes darker colors (high z-values). Islands that are surrounded by the “flood” are stored as boundaries. For more information about the watershed algorithm is referred to [23] and [24]. Watershedding allowed the identification of the boundaries between the columnar structures which were afterward plotted on top of the measured modulus map as shown in last picture of Figure 10. The blue lines indicate the boundaries of the height map which were found by the watershed algorithm. The blue lines almost perfectly align with the “high-modulus web” which was observed in the modulus map. This confirms that the topography influences the measurement of the modulus. The effect of the topography can be explained by assumptions of the DMT model [25].

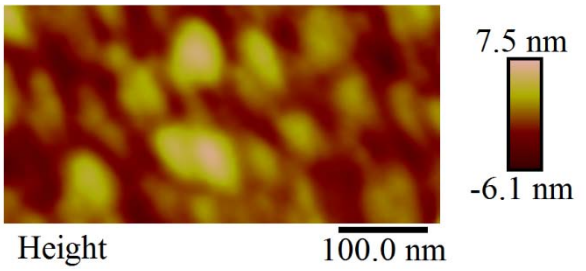

(a)

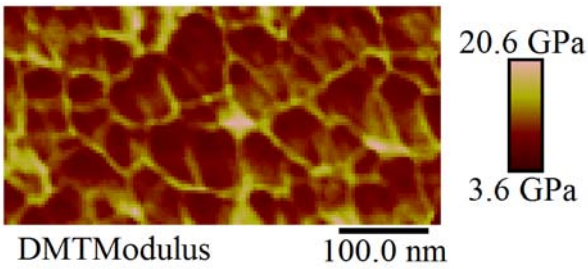

(b)

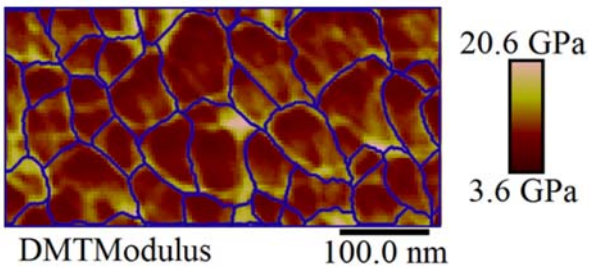

(c)

Figure 10. (a) AFM Topography image (planarized) of the 300 nm thick coating. (b) Corresponding DMT Modulus map of the picture in (a). (c) The DMT Modulus map of (b) with an overlay of the boundaries of the height-image (a) measured using the Watershed-algorithm. A clear correlation is found between the boundaries in the topography map and the maxima in the modulus

The DMT model assumes the contact between two spheres. The contact between tip and sample at the cusps will be governed by side contact of the adjacent spheres. This leads to a much higher contact area and thereby an overestimation of the calculated modulus. As a result, only the coatings on top of the spheres can be used for the analysis. The data of the samples was processed using a Matlab script, which calculates the local maxima of the topography map and takes the measurement values of the modulus map at the corresponding coordinates.

This procedure was used to calculate the Young's modulus. Figure 11a and b show the arithmetic surface roughness (Ra) in nm and the Young's modulus in GPa as a function of the coating thickness, respectively. Each data point represents the average of at least three scans. The morphology shows a clear trend that the surface roughness increases with the coating thickness. Figure 11b however shows that the coatings up to 500 nm have an identical Young's modulus of 11.5 ± 1 GPa. The 640 nm thick coatings show a slightly higher Young's modulus of 14.2 ± 2 GPa. The 1250 nm thick coating has a Young's modulus that is over two times higher compared to the other coatings. The identical results for the coatings up to 500 nm strongly support that the measurement does not get influenced by the substrate and that effects of the surface roughness can be corrected for. The increasing error for the thicker coatings indicates that for very rough surfaces, the deviations from the model become larger and thereby reduces the accuracy of the method. The increase in the Young's modulus can be assigned to the higher thermal load on the coating as a result of the longer exposure time to the plasma and thereby a more dense coating is produced. As this could not be excluded, only the samples with a coating thickness below 1 µm were considered in further investigations. The absolute values that were measured are very questionable as the CSM measurement of the 640 nm thick coating already shows values above 15 GPa even though it is known the that CSM measurement underestimated the actual Young's modulus.

This absolute error is partly assigned to the relative calibration method as the HOPG Sample presented us values between 15 and 25 GPa (after an initial calibration at 18 GPa). This already leads to an error of 25%. In addition, the surface topography of the HOPG was very different (smooth flat flakes) compared to the structure of the coating, which most likely has an impact on the contact mechanics between the coating and sample as well.

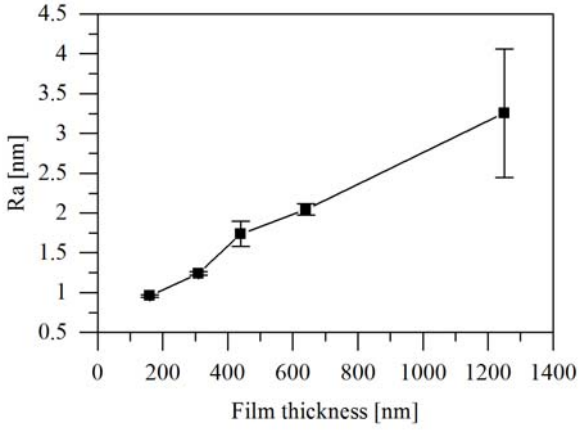

(a)

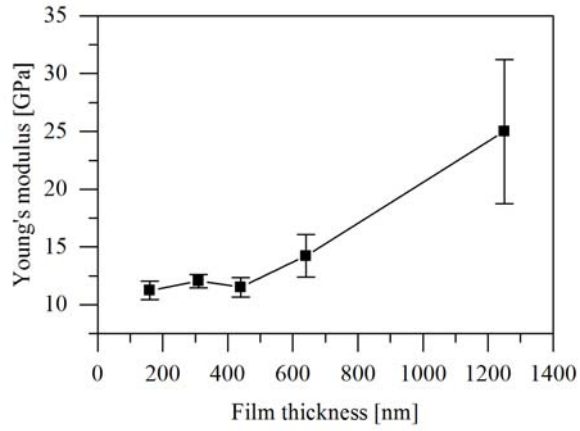

(b)

Figure 11. (a) The arithmetic surface roughness (Ra) as a function of the coating thickness. With increasing coating thickness, the morphology of the coating becomes rougher. (b) The average Young's modulus of the samples as a function of the coating thickness. The thin coatings up to 500 nm show similar values. The 600 nm thick coating shows a slightly higher modulus and the 1250 nm coating is 2 times higher compared to the other values. With increasing roughness, the error in the measurement increases as well.

In summary, Peakforce QNM offers a way to obtain fast information on both the surface topography and relative mechanical properties. It has the potential to measure thin coatings of soft substrates. For absolute measurements, a calibration sample with similar properties and as well as similar surface topography is essential to obtain accurate results.

4.3.3 Atomic Force Acoustic Microscopy

Alternatively to PeakForce measurements, Atomic Force Acoustic Microscopy (AFAM) can be used to analyze the coatings. AFAM setups are based on contact resonance spectroscopy and are similar to an AFM with the sample located on a broadband transducer. Whilst PeakForce QNM applies a sinusoidal vibration to the tip and measures the deflection, AFAM methods use a transducer to apply a frequency sweep on the sample while the tip is in contact with the coating [26]. The resonance of the cantilever is measured and a resonance peak will be observed at the effective tip-sample spring constant k^*. k^* can be related to the tip and sample properties by [27]

$$\frac{1}{k^*} = \frac{1}{k_{sample}} + \frac{1}{k_{tip}} \tag{4.7}$$

k_{sample} is the spring constant of the sample and k_{tip} corresponds to the spring constant of the tip.

Before deriving the Young's modulus, we need to take a closer look at the contact mechanics between the tip and the coating. Using classical Hertzian contact mechanics, two spherical bodies are in elastic contact with each other. This is schematically shown in Figure 12a. The contact area can be described by a circle with radius a. For this description, the spring constant of the sample and tip can be described by

$$k_x = 2M_x a \tag{4.8}$$

Where M_x is the elastic modulus of the sample or tip and a is the contact radius between the tip and the sample. Work of Kopycinska-Müller et al. [28,29] showed that the AFM tip, for single nm indentation depths, should be approximated by a flat punch instead. Additionally, the asperities at the surface of the indenter influence the contact area as well at indentation depths in the single nanometer range and should be taken into account. A schematic representation is given in Figure 12b.

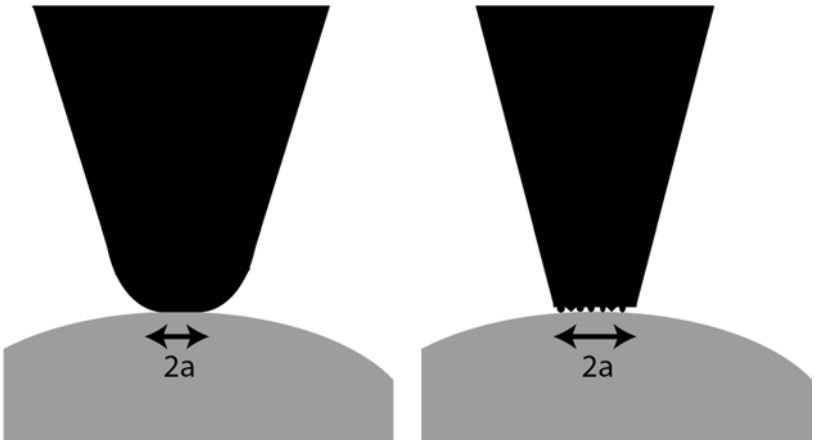

(a) (b)

Figure 12.(a) Schematic representation of Herztian contact, Both the sample (gray) and the tip (black) are described by a sphere in pure elastic contact. (b) Schematic representation of the tip-sample contact as described by Kopycinska et al. [29]. The tip is described as a cone with a flat punch. At the top of the flat punch, asperities are present that reduces the actual contact.

They proposed a modified equation for k_{tip} being

$$\frac{1}{k_{tip}} = \frac{1}{0.611\, M_{tip} \cdot a} + \frac{1}{A \cdot E^{*(1-m)} \cdot F^m} \tag{4.9}$$

Where A represents the fill factor of the asperities, F represents the applied load, E^* is the reduced modulus ($\left(\frac{1}{M_s} + \frac{1}{M_{tip}}\right)^{-1}$) and m is the form factor of the asperities ($m = 0$ corresponds to a cylindrical shape and $m = 1/3$ corresponds to a spherical shape).

Combining Eq. (4.7) - (4.9) gives us an expression for the effective tip-sample spring constant k^*

$$\frac{1}{k^*} = \frac{1}{2M_s a} + \frac{1}{0.611\, M_{tip} \cdot a} + \frac{1}{A \cdot E^{*(1-m)} \cdot F^m} \tag{4.10}$$

The effective contact radius (a) is determined using a calibration sample. Within this research, fused silica with a Young's modulus of 72 GPa [12] was used. After calibration of the contact radius, the effective tip-sample spring constant k^* was calculated for different loads. Eq. (4.10) was fitted to

the data and solved for M_s. The reduced substrate modulus can be converted into the Young's modulus E_s by

$$E_s = M_s \cdot (1 - \nu^2) \tag{4.11}$$

Where ν denotes Poisson's ratio. Figure 13 shows an example of the development of the tip-sample contact stiffness normalized over the cantilever stiffness (35 N/m) as a function of the applied load. The filled markers denote the loading curve and the open markers denote the unloading curve. The difference between loading and unloading indicates plastic behavior of the sample. The load of 1400 nN corresponds to a calculated indentation depth of 4 nm.

7 measurements were performed on both the 300 and 600 nm thick coating. The tip radius was measured using a reference material (fused silica) and was 23 ± 2 nm. Using the known tip radius, the Young's modulus was calculated for the 300 and 640 nm thick coating. The calculated Young's moduli were 19.2 ± 2.3 GPa and 19.2 ± 1.5 GPa, respectively. The similar moduli for 300 and 600 nm thick coatings agree to the measurements made with the PeakForce QNM method. However, the values measured with PF QNM were approximately 25 % lower.

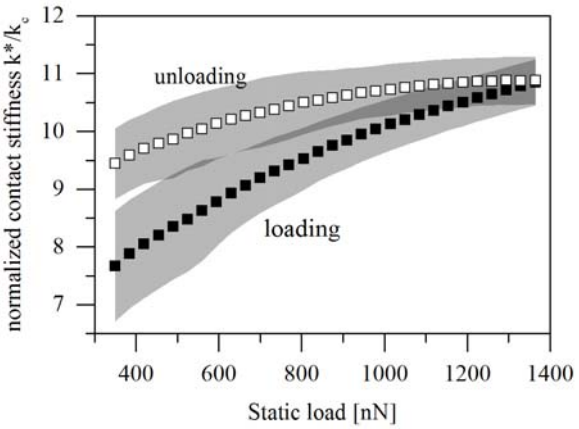

Figure 13. An example of the normalized contact stiffness against the applied load of the tip. The filled markers represent the loading curve and the unfilled markers represent the unloading.

4.3.4 Nanoindentation on the coating cross-section

Alternatively to indentation in the growth direction of the coating, a cross-section can be prepared that is directly indented as is schematically shown in Figure 14a. This requires a high positioning accuracy of the indenter which is possible using the SPM possibilities of the Hysitron TI 950 TriboIndenter. This allows us to perform Dynamic Mechanical Analysis (DMA) with a lateral resolution at the nano-scale. The nanoDMA analysis with a high lateral resolution provides us with spatial resolved information on the mechanical properties as well as on the microstructure.

During a DMA analysis, an oscillating force is applied to the sample leading to an oscillation of several nm into the coating. Based on the response of the coating, the mechanical behavior of the coating can be characterized. A sinusoidal stress is applied that can is described at time t by [30]

$$\sigma(t) = \sigma_0 \sin \omega t \tag{4.12}$$

Where σ_0 is the maximum applied stress and ω is the frequency of oscillation. The response of the material in terms of strain (ϵ) at time t can be described by

$$\epsilon(t) = \epsilon_o \sin(\omega t + \delta) \tag{4.13}$$

Where ϵ_0 is the maximum strain and δ is the phase lag between applied stress and measured strain. For purely elastic materials, the reaction of the material will be instantaneous corresponding to $\delta = 0$. For purely visco-elastic materials, the strain is proportional to the stress rate which causes a phase lag of $\delta = \frac{\pi}{2}$. As real materials provide both an elastic as well as visco-elastic reaction, the phase lag lies somewhere between these extreme cases and is used characterize the material behavior. Both contributions are quantified by the storage (elastic portion) modulus ϵ_s and loss (visco-elastic portion) modulus ϵ_l:

$$\epsilon_s = \epsilon_0 \sin(\delta) \tag{4.14a}$$

$$\epsilon_l = \epsilon_0 \cos(\delta) \tag{4.14b}$$

The Young's modulus can be calculated from there by

$$E = \sqrt{\epsilon_s^2 + \epsilon_l^2} \times (1 - \nu^2) \tag{4.15}$$

Two different methods were used to prepare a cross-section of the coating. The first two specimen were prepared using ultramicrotomie. Before preparation, the specimen was mechanically supported by embedding the specimen in an Embed 812 Epoxy resin. The resin was cured at 60 °C. The cross-section was prepared using a UV6 Ultramicrotome (Leica-Microsystems) with a diamond cutter. The cut was made in water to avoid scratching as a result of generated particles. The final sample is shown in Figure 14b. The upper part (indicated with the arrow) was sliced with the ultramicrotome to create a smooth surface.

The ultramicrotome cut was performed in two directions, one parallel and one perpendicular to the coating direction. Additionally, a cross-section was prepared using an ion polisher. More information on this preparation technique can be found in chapter 2. All cross-sections were analyzed using nanoDMA mapping and SEM imaging

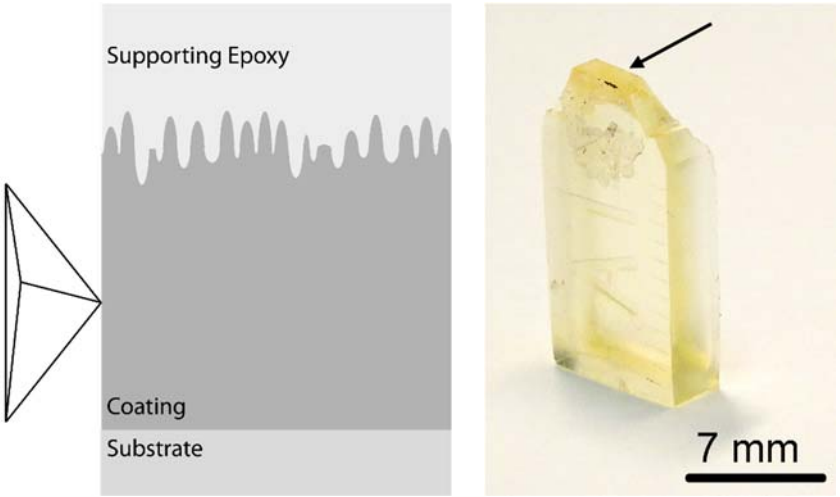

(a) (b)

Figure 14. (a)) Schematic representation of the indentation during cross-section nano-indentation. (b) Sample after preparation. The upper part (indicated with the arrow) of the sample was used for the analysis.

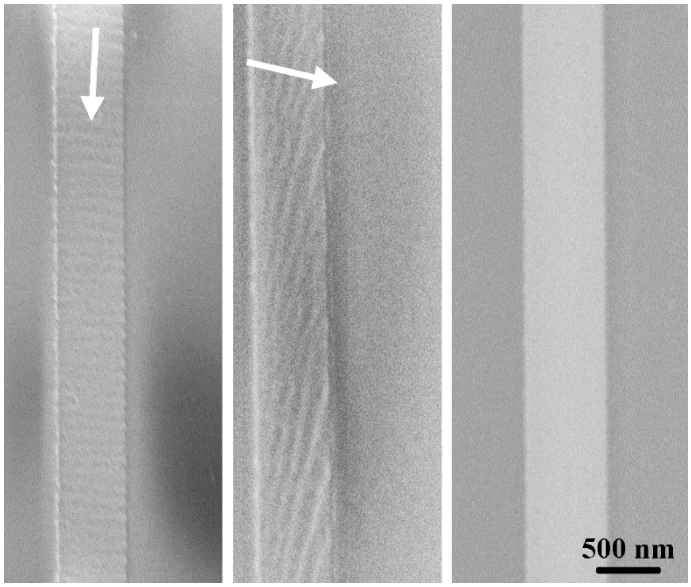

(a) (b) (c)

Figure 15. SEM images of the prepared cross-sections. (a) and (b) are prepared using ultramicrotomie. The white arrow indicate the direction of the cut. (c) was prepared using the ion polisher.

Figure 15 shows the SEM images of the three cross-sections that were prepared. (a) and (b) show the cross-sections prepared using ultramicrotomie under two different cutting angles. The white arrows indicate the direction of the cut. (c) shows the cross-section prepared using the ion polisher.

The cross-sections prepared using ultramicrotomie show a wave like microstructure in the coating. The waves are perpendicular to the cutting direction of the ultramicrotome, which strongly indicates that they are the results of the sample preparation. It is anticipated that vibrations during the preparation lead to these small waves. The cross-section made with the ion polisher shows a perfectly smooth surface without any noticeable microstructure. The three cross-sections were analyzed using nanoDMA and the maps of the measured storage moduli are shown in Figure 16. Figure 16a shows that the mechanical characterization is clearly affected by the remaining microstructure of the cross-section prepared using ultramicrotomie. A profile of the storage modulus was taken at the center of the coating and plotted in Figure 17a. A large variation between

approximately 10 and 17 GPa is observed, which makes it very difficult to correctly interpret the data. It should be mentioned that the topological height of these waves was only 1-2 nm between neighboring minima and maxima. Even such small structures already lead to such a large error in the mechanical measurement. The results of the cross-section with the cutting direction perpendicular to the coating are shown Figure 16b. The effect of the microstructure is almost invisible. Some slight waviness can be observed at the left side of the coating. However, the center area shows much less variation compared to the first sample as can be seen in Figure 17b. All graphs in Figure 17 have the same vertical scale to provide a good comparison. Whereas the variation in much less, the average modulus is only 8.9 ± 0.5 GPa. This is much smaller as expected based on the CSM measurements.

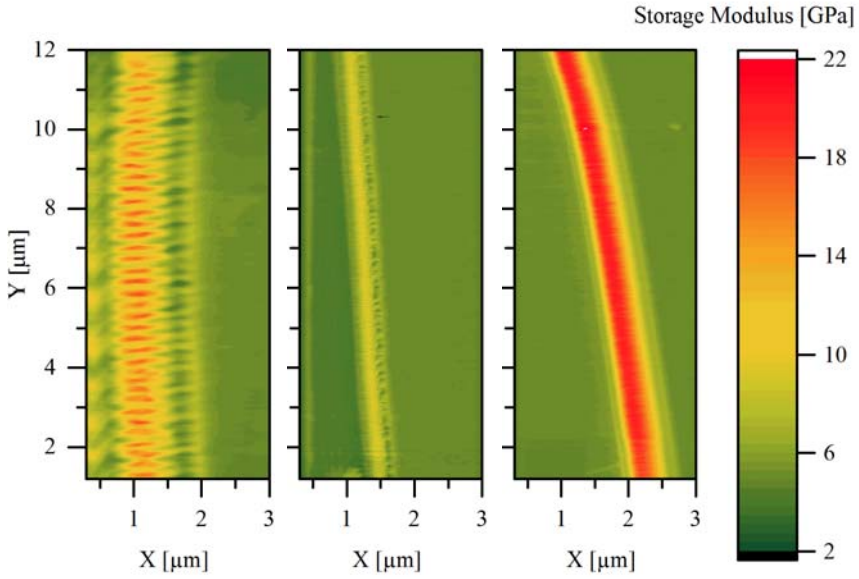

Figure 16. The storage modulus map of the three prepared cross-section. (a), (b) and (c) correspond to the SEM images shown in Figure 15.

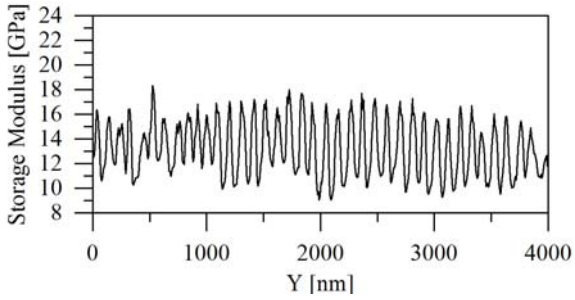

(a)

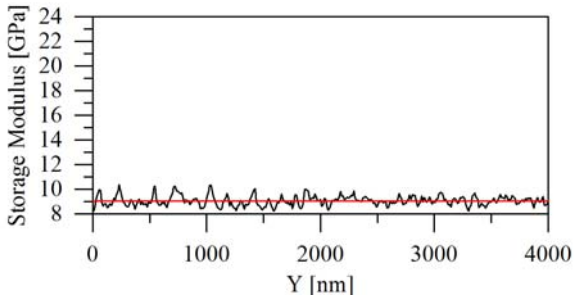

(b)

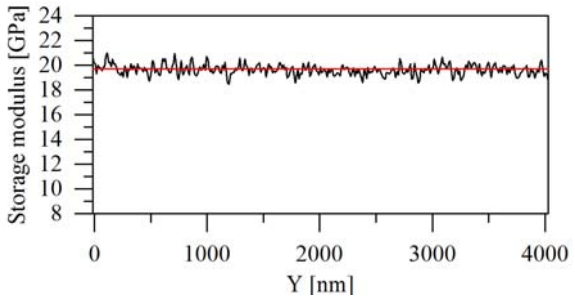

(c)

Figure 17. Profiles of the Storage modulus maps (Figure 16) were taken from the center of the coating. (a), (b) and (c) correspond to the SEM images shown in Figure 15. All graphs have the same vertical scale for easy comparison.

Figure 18 analyzes the profile perpendicular to the coating and shows that there is no stable value measured at the center of the coating. It is anticipated that during the cut perpendicular to the coating, epoxy is spread out over the surface of the coating leading to the formation of a thin epoxy film. The much lower Young's modulus of the epoxy leads to an underestimation of the mechanical properties of the coating.

The last cross-section that is discussed in this section was prepared with the ion polisher. Figure 16c shows a map of the measured storage moduli. The smooth surface of the cross-section clearly improves the homogeneity of the mechanical results. The profile at the center of the coating was shown in Figure 17c. The average storage modulus of 19.7 ± 0.6 GPa is much higher compared to Figure 17b. This strongly supports the statement that the surface of the cross-section gets contaminated when performing an ultramicrotomic cut perpendicular to the coating direction. As the results in Figure 7 already showed that the main response of the coating is elastic, the storage modulus is expected to be much higher compared to the loss modulus. The analysis of the loss modulus confirmed that viscoelastic behavior of the coating is not significant (E_{loss} < 1 GPa). Eq. 4.15 was used to calculate the Young's modulus returning a value of 17.9 ± 0.6 GPa.

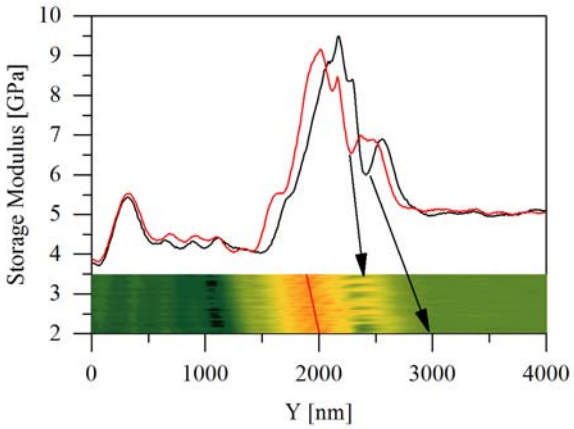

Figure 18. Storage modulus profiles perpendicular to the coating. The two lines corresponds to the upper and lower line of the modulus map.

4.3.5 Discussion

Four different indentations methods were discussed in this chapter. As the results do not always agree with each other, it suffices to say that the indentation of these films is extremely challenging and should not be underestimated. Technological developments of both the AFM and nano-indenter allow us to measure both the mechanical and topological properties with high spatial resolution. These maps were found to be extremely helpful while discussing the validity of the results and finding possible error sources. To compare the different methods, all measurement results on the 640 nm thick coating are shown in Figure 19. The continuous black line represents the CSM result. The curve shows a steep drop starting at 20 GPa and already decreased below 10 GPa within the first 100 nm indentation depth. As part of the initial 50 nm can be identified as section (a) (see Figure 6), an even higher modulus would be expected as roughness effects tend to underestimate the actual modulus [31] due to their reduced contact area. Combining the sharp decrease and possible roughness effects, an even higher modulus than 20 GPa is expected solely based on the CSM measurements.

The Peak Force QNM measurements returned the lowest value of 14.2 GPa. For the Peak Force measurements, it was already concluded that an accurate

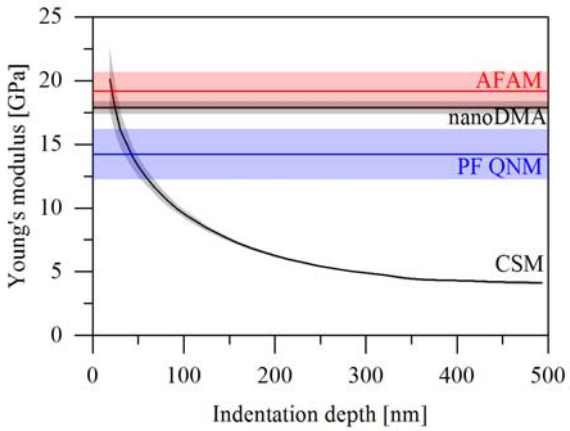

Figure 19. Isolated CSM results of the 640 nm thick coating. The red line represents the AFAM result. The blue line represent the PF QNM result. The horizontal black line represents the nanoDMA result on the cross-section of the coating.

calibration sample is required to guarantee reliable results. The sample should not only exhibit similar mechanical properties but also a similar microstructure.

The results of the AFAM measurements correspond to the initial measurement values of the CSMs indicating that the advanced model for the contact mechanics between sample and tip is able to calculate the Young's modulus of the coating very well even though the calibration sample (fused silica) has a much higher Young's modulus and different microstructure.

The nanoDMA measurements show very good agreement with the AFAM measurements provided that a sample can be prepared without any remaining microstructure or surface contamination. The ion polisher proofed to be a good preparation method for this type of samples. The preparation of the cross-section has an advantage over the AFAM method for samples with extremely high surface roughness that may be not well described by the introduced tip-sample interaction model. Careful selection of the appropriate preparation method does require additional effort for the cross-section nanoDMA analysis.

4.4 Conclusions

This chapter introduces a novel method for the measurement of residual stresses that is applicable for samples with high curvatures. Different error sources were successfully identified and corrections or estimations of the resulting error were provided. This setup is especially interesting to measure external influences of the environment as the setup is relatively small and very mobile and can be used to measure very small changes in the sample curvature. Measurement under controlled conditions are extremely advantageous to allow calculation of the environmental contribution to the stress. This will be discussed in more detail in the next chapter.

A critical analysis of the Stoney equation is provided and correction terms are discussed to convert the radius of curvature into the residual stress for the samples used in this research. A reliable description of the stress requires to take the effect of the coating thickness and in-plane deformation of the substrate into account,.

To summarize this chapter, mechanical characterization of thin stiff coatings on soft substrates remains a challenging tasks. The technological and scientific advances over the last years allow very accurate measurements and improved understanding of the tip-sample geometry. Combining measurement techniques and the possibility to map mechanical properties and compare them with microstructural information is considered very helpful to understand whether measurement are valid and to identify possible error sources. The CSM measurements were very helpful for coatings above several hundred nanometer to provide a window of the expected Young's modulus. Depending on the possibilities, cross-section nanoDMA or AFAM measurements could help to quantify the exact modulus. If a proper reference sample is available, Peak Force QNM is a good and fast method to measure the coating properties as well.

4.5 References

[1] J. Schindelin, I. Arganda-Carreras, E. Frise, V. Kaynig, M. Longair, T. Pietzsch, S. Preibisch, C. Rueden, S. Saalfeld, B. Schmid, J.-Y. Tinevez, D.J. White, V. Hartenstein, K. Eliceiri, P. Tomancak, A. Cardona, Fiji: an open-source platform for biological-image analysis, Nat Meth 9 (2012) 676–682.

[2] F. Gruber, P. Wollmann, B. Schumm, W. Grählert, S. Kaskel, Quality Control of Slot-Die Coated Aluminum Oxide Layers for Battery Applications Using Hyperspectral Imaging, Journal of Imaging 2, 2016.

[3] G.G. Stoney, The Tension of Metallic Films Deposited by Electrolysis, Proceedings of the Royal Society of London. Series A, Containing Papers of a Mathematical and Physical Character 82 (1909) 172–175.

[4] S. Timoshenko, Analysis of Bi-Metal Thermostats, J. Opt. Soc. Am. 11 (1925) 233–255.

[5] C.B. Masters, N.J. Salamon, Geometrically nonlinear stress-deflection relations for thin film/substrate systems, International Journal of Engineering Science 31 (1993) 915–925.

[6] Y. Leterrier, A. Pinyol, L. Rougier, J. H. Waller, J.-A. Månson, P. J.J. Dumont, J. Andersons, J. Modniks, M. Campo, P. Sauer, J. Schwenzel, Influences of roll-to-roll process and polymer substrate anisotropies on the tensile failure of thin oxide films, Thin Solid Films 518 (2010) 6984–6992.

[7] L. Körner,A. Sonnenfeld, R. Heuberger, J.H. Waller, Y. Leterrier, J.A.E. Månson, Ph. R. von Rohr, Oxygen permeation, mechanical and structural properties of multilayer diffusion barrier coatings on polypropylene, J. Phys. D: Appl. Phys. 43 (2010) 115301.

[8] A. Morinaka, Y. Asano, Residual stress and thermal expansion coefficient of plasma polymerized films, Journal of Applied Polymer Science 27 (1982) 2139–2150.

[9] Yves Leterrier, Durability of nanosized oxygen-barrier coatings on polymers, Progress in Materials 48 (2003) 1–55.

[10] K. Röll, Analysis of stress and strain distribution in thin films and substrates, J. Appl. Phys. 47 (1976) 3224–3229.
[11] M. Benabdi, A.A. Roche, Mechanical properties of thin and thick coatings applied to various substrates. Part I. An elastic analysis of residual stresses within coating materials, Journal of Adhesion Science and Technology 11 (1997) 281–299.
[12] W.C. Oliver, G.M. Pharr, An improved technique for determining hardness and elastic modulus using load and displacement sensing indentation experiments, J. Mat. Res. 7 (1992) 1564–1583.
[13] W.C. Oliver, G.M. Pharr, Measurement of hardness and elastic modulus by instrumented indentation: Advances in understanding and refinements to methodology, J. Mat. Res. 19 (2004) 3–20.
[14] A.A. Pelegri, X. Huang, Nanoindentation on soft film/hard substrate and hard film/soft substrate material systems with finite element analysis, Compos. Sci. Technol. 68 (2008) 147–155.
[15] B. Zhou, B.C. Prorok, A new paradigm in thin film indentation, J. Mater. Res. 25 (2010) 1671–1678.
[16] Xiaodong Li, Bharat Bhushan, A review of nanoindentation continuous stiffness measurement technique and its applications, Mater. Charact. 48 (2002) 11–36.
[17] B. Pittenger, N. Erina, C. Su, in: A. Tiwari (Ed.), Nanomechanical Analysis of High Performance Materials, Springer Netherlands, Dordrecht (2014), 31–51.
[18] V. Cech, T. Lasota, E. Palesch, J. Lukes, The critical influence of surface topography on nanoindentation measurements of a-SiC:H films, Surf. Coat. Technol. 261 (2015) 114–121.
[19] M.E. Dokukin, I. Sokolov, On the Measurements of Rigidity Modulus of Soft Materials in Nanoindentation Experiments at Small Depth, Macromolecules 45 (2012) 4277–4288.
[20] M.E. Dokukin, I. Sokolov, Quantitative mapping of the elastic modulus of soft materials with HarmoniX and PeakForce QNM AFM modes, Langmuir the ACS journal of surfaces and colloids 28 (2012) 16060–16071.
[21] T.J. Young, M.A. Monclus, T.L. Burnett, W.R. Broughton, S.L. Ogin, P.A. Smith, The use of the PeakForce TM quantitative nanomechanical mapping AFM-based method for high-resolution Young's modulus measurement of polymers, Meas. Sci. Technol. 22 (2011) 125703.
[22] Bruker Nano Surfaces Division, Introduction to Bruker's ScanAsyst and PeakForce Tapping AFM Technology, 2011, accessed 2 August 2017.
[23] D. Sage, Graylevel watershed, Biomedical Image Group, Switzerland, 2011, http://bigwww.epfl.ch/sage/soft/watershed/.
[24] S. Beucher, C. Lantuejoul, in: International Workshop on Image Processing: Real-time Edge and Motion Detection/Estimation, Rennes, France (1979).
[25] B. Derjaguin, V. Muller, Y. Toporov, Effect of contact deformations on the adhesion of particles, J. Colloid Interface Sci. 53 (1975) 314–326.
[26] U. Rabe, S. Amelio, E. Kester, V. Scherer, S. Hirsekorn, W. Arnold, Quantitative determination of contact stiffness using atomic force acoustic microscopy, Ultrasonics 38 (2000) 430–437.
[27] G.S. Batog, A.S. Baturin, V.S. Bormashov, E.P. Sheshin, Calculation of the thicknesses and elastic properties of thin-film coatings using atomic-force acoustic microscopy data, Technical Physics 51 (2006) 1084–1089.
[28] M. Kopycinska-Mueller, J Gluch, B Köhler, Study of mechanical behavior of AFM silicon tips under mechanical load, Nanotechnology 27 (2016) 454001.
[29] M. Kopycinska-Müller, J. Gluch, U. Rabe, B. Köhler, Verfahren zum Kalibrieren einer Spitze eines Rasterkraftsmicroscops, Patent DE 2016P58793.

[30] K.P. Menard, Dynamic Mechanical Analysis: A Practical Introduction, Second Edition, CRC Press, 2008.
[31] C. Walter, C. Mitterer, 3D versus 2D finite element simulation of the effect of surface roughness on nanoindentation of hard coatings, Surf. Coat. Technol. 203 (2009) 3286–3290.

Chapter 5

Influence of the carbon concentration inside the coating on the mechanical properties and stress formation mechanisms[a]

In practice, residual stresses are unavoidable in material systems with different thermo-mechanical properties [1]. High residual stresses are, especially in thick coatings, an important cause for coating failure as a result of delamination, spalling and cracking of the coating. Coating failure is well studied in literature [2–5]. To minimize the probability of cracking or delamination, it is important to have a

1. *high coating toughness*
2. *low residual stress state*
3. *high interfacial adhesion.*

---

[a] *A part of this chapter is based on the following journal publication:*

Michiel Top, Guus Mulder, Nicole Prager; John Fahlteich, Jeff Th. M. De Hosson, (2018): Effect of humidity on the residual stress in silicon-containing plasma polymeric coatings. In Surface and Coatings Technology 347, pp.46–53. DOI: 10.1016/j.surfcoat.2018.04.066.

As already introduced in chapter 1, these requirements can become more complicated in multi-layer systems as the interfacial adhesion between the underlying layers could introduce additional weak point within the system leading to buckling of the upper layers. Therefore it is important to reduce the residual stress within multi-layer coating systems.

The residual stress is caused by a combination of different stress formation mechanisms. It is important to have an in-depth understanding of the origin of the stress in order to minimize the residual stresses. This chapter aims at separating the different contributions to the residual stress state of plasma polymer coatings on polymer substrate deposited in a roll-to-roll system. The effect of the carbon concentration in the coating is discussed for the coating dependent stress formation mechanisms.

5.1 Origins of residual stresses in a Roll-to-Roll (R2R) system

Whereas static deposition is usually well approximated by an isotropic bi-axial stress distributions in the X and Y direction for all mechanisms, anisotropy needs to be considered for Roll-2-roll deposited samples due to the machine direction of the web coater as well as the anisotropic nature of the PET substrate. The anisotropy of the PET substrate is related to the production process. The substrate is stretched both along and perpendicular to the machine direction directly after the extrusion. This leads to non-isotropic mechanical properties of the substrate [6,7]. Two main directions are differentiated: Machine Direction (MD) and Transverse Direction (TD), which are illustrated in Figure 1.

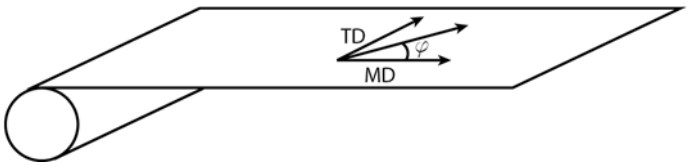

Figure 1. Residual stresses in a Roll-to-roll system cannot be considered isotropic. In the further discussion, the Machine Direction (MD) and the Transverse Direction (TD) are differentiated. The angle φ is used to describe the remaining directions.

Several stress contributions are related to the coating properties and are, under the assumption of an isotropic coating, acting in all directions [8]:

$$\sigma = \sigma_{intrinsic} + \sigma_{thermal\ expansion} + \sigma_{hygroscopic\ expansion} \quad (5.1)$$

$\sigma_{intrinsic}$ covers the processing induced stress related to different coating formation stages and microstructural development and is closely related to the growth mechanism. $\sigma_{thermal\ expansion}$ is related to the difference of the thermal expansion coefficient between the coating and the substrate. Thermal expansion is well scrutinized in literature [9–11] because elevated substrate temperatures during deposition are often used to improve the functional coating properties [12–14]. Thermal stress can also lead to device failure for applications were the sample is exposed to large variations in temperature (e.g. building integrated photovoltaics). $\sigma_{hygroscopic\ expansion}$ is related to stress induced by changes in the relative humidity when the substrate and coating have different coefficients of hygroscopic expansion. Unfortunately, only scant information is available on the hygroscopic expansion of thin plasma polymer coatings [8] even though it is known that water vapor leads to volumetric changes [15,16] of polymeric materials and may cause device failure [17].

The hygroscopic and intrinsic stresses will be discussed in section 5.5 and 5.6. Section 5.7 will shortly introduce the thermal expansion and discuss the challenges to obtain reliable information on the thermally induced residual stress.

Residual stress for coatings deposited in a roll-to-roll process contain additional components in MD and TD, which are described by

$$\sigma_{MD^\circ} = \sigma_{intrinsic} + \sigma_{thermal\ expansion} + \sigma_{hygroscopic\ expansion} + (\sigma_{web\ tension} + \sigma_{viscoelasticity}) + \sigma_{curved\ deposition} \quad (5.2)$$

and

$$\sigma_{TD} = \sigma_{intrinsic} + \sigma_{thermal\ expansion} + \sigma_{hygroscopic\ expansion} - \upsilon * \sigma_{web\ tension} \quad (5.3)$$

$\sigma_{web\ tension}$ is induced by the applied web tension and leads to elongation of the substrate along MD and contraction (υ represents Poisson's ratio of the substrate) of the substrate along TD. $\sigma_{viscoelasticity}$ is related with

viscoelastic deformation of the substrate during storage. $\sigma_{curved\ deposition}$ is related to the curved state of the substrate during the deposition. These contributions will be discussed in section 5.3 and 5.4.

Mathematical description of the deflection field

As the stresses in the MD and TD are both significant, the forces will add up and lead to a resulting curvature that is measured. The displacement field for a sample is described by

$$W(X,Y) = \frac{1}{2}\,(a\,X^2 + b\,Y^2) \tag{5.4}$$

were W describes the deflection at the coordinates X and Y. a and b represent the radius of curvature in X and Y direction. Choosing X and Y parallel to MD and TD generally leads to non-zero values of a and b. As the substrates cannot bend in both directions, the maximum curvature of the sample will be somewhere between the MD and TD directions at an angle φ as is schematically shown in Figure 2. Because Masters et al. [18] showed that non-linear terms in the stress can only be neglected for samples when $a \to 0$ or $b \to 0$, we need to rotate our coordinate system with $\varphi°$ to make sure that a or b becomes zero before we are able to calculate the stress using Eq. (4.5). The deflection field for the highly curved samples in this research can be described by

$$W(X',Y') = \frac{1}{2} r\,(Y')^2 \tag{5.5}$$

after rotating the system of coordinates by $\varphi°$. W is the deflection and r is the radius of curvature in the Y' direction. The curvature in X' direction is zero. The rotation of the coordinate system is schematically illustrated in Figure 2. Both φ and r can be measured experimentally. The circle indicates the specimen used for the measurement and the dashed lines indicate the direction without curvature. The radius of curvature to calculate the stress will be evaluated along the Y'-axis.

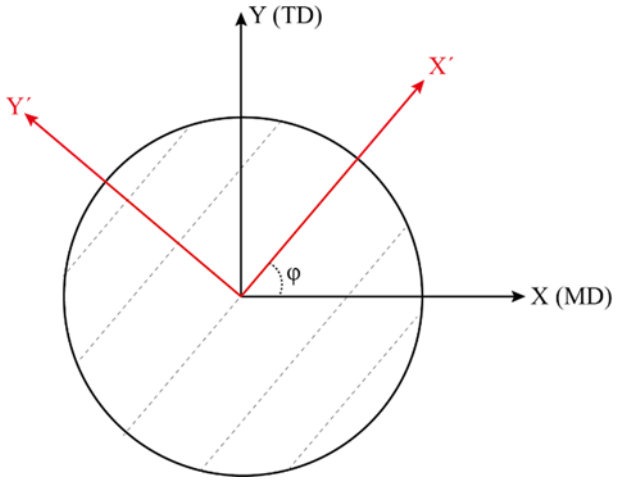

Figure 2. Schematic representation of the system of coordinates chosen for the stress calculation. X and Y correspond to the machine direction (MD) and the transverse direction (TD), respectively. X´ and Y´ denote the rotated system where the specimen shows no curvature along X´.

Experimental parameters.

Several publications discuss the relationship between deposition process parameters and the residual stress of silicon-containing plasma polymer coatings. Unfortunately, the complexity of the stress formation mechanism leads to a limited understanding [19,20]. Even a comparison of results among publications in literature that focus on the stress formation in PECVD deposited coatings using HMDSO and oxygen is difficult due to the interdependencies of the process parameters as will be further explained in section 5.6. To isolate the effect of the change in Oxygen-to-HMDSO ratio, the sample analyzed in this chapter are deposited under constant HMDSO flow, power and pressure. The constant HMDSO flow provides similar deposition rates (between 281 and 346 nm·m/min). Choosing the web speed appropriately, coatings of 500 and 1000 nm were deposited for Oxygen-to-HMDSO ratios of 3, 6 and 10. The pressure was kept constant by reducing the pumping speed when the oxygen flow was reduced. The variation in the oxygen flow could not be extended any further as we were not able to maintain the same pressure (2.7 Pa) during the deposition with higher or lower oxygen flow due to the limited range of pumping speed. The remaining process parameters can be found in Table 1. It has to be mentioned

that even though the total pressure remains the same, the partial pressure of oxygen as well as for the HMDSO fragments changes. However, these parameters were not accessible within the web coater and are therefore not considered. During variation of the oxygen flow, the applied web tension was kept constant at 80 N. The web tension was varied in section 5.4 to determine the effect of the applied web stress whereas the oxygen flow was kept constant at 200 sccm.

Table 1. Overview of the experimental process parameters used for the deposition of the coatings in this section.

Process parameter	Range
Web coater	***labFlex® 200***
Web speed	0.56-0.64 m/min (500 nm coating thickness)
Cooling drum temperature	Room Temperature
Argon Flow	200 sccm + 70 sccm through the hollow cathode
Web tension	50 - **80** -140 N
HMDSO flow	50 sccm
Oxygen flow	150-600 sccm
Process pressure	2.73 ± 0.05 Pa
HC Discharge Current / Voltage	150 A / 13.8 - 14.7 V
BA Discharge Current / Voltage	95 A / 21.4 – 21.9 V

5.2 Chemical and Mechanical characterization

A brief overview of the chemical (EDS), topological (SEM/AFM) and mechanical (CSM/AFAM) properties is provided before the individual stress mechanisms are discussed. The results of the EDS analysis are listed in

Table 2 and show that the oxygen to silicon ratio in the coating increases as expected whereas the carbon concentration in the coating decreases. Even the sample with the highest oxygen flow has 1.6 times more carbon compared to silicon in the coating, which indicates that all coatings have a significant organic fraction and are not directly comparable to SiO_2. The surface roughness for the 1000 nm thick coatings decreases slightly from 3.8 to 3.3 nm with increasing oxygen flow.

Figure 3 shows the microstructure of the three 1000 nm thick coatings. From top to bottom, the samples that were deposited with (a) low, (b) medium and (c) high oxygen flow are displayed. The micro-crack is analyzed under an angle of approximately 45° to obtain information on both the surface microstructure (upper part) and the cross-section (lower part) after crack formation.

The coatings look very similar. All samples show a cauliflower like surface topography. For the sample with low oxygen flow, the microstructure at the surface seems to be more compressed whereas the sample with high oxygen flow looks more porous. Looking at the cross-sections of the three coatings, it was found that the approximately 100 nm at the top of the cross-section for all coatings show a columnar structure that represents the features at the surface indicating a columnar structure. However, below these 100 nm, all coatings show a dense and (within the resolution of the microscope) pore-fee bulk material.

Table 2. Overview of the Chemical composition (EDS), surface properties (AFM) and mechanical properties (AFAM).

O2:HMDSO ratio [-]	**O/Si [-]**	**C/Si [-]**	**Surface Roughness [nm]**	**Young's modulus [GPa]**
3	1.5	2.8	3.8 ± 0.1	19.3 ± 1.8
6	1.9	2.4	3.8 ± 0.1	18.6 ± 1.7
10	2.1	1.6	3.4 ± 0.2	21.0 ± 1.5

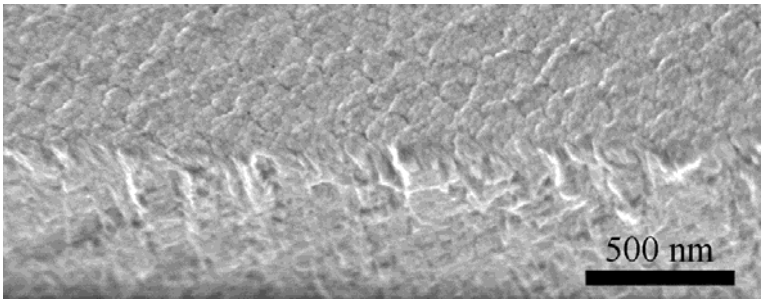

(a)

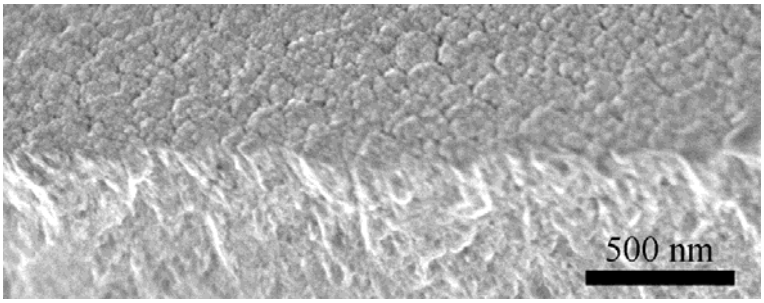

(b)

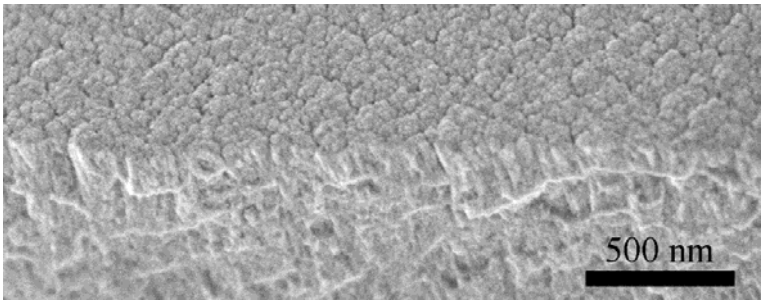

(c)

Figure 3. SEM micro-crack images of the 1 µm thick coating with Oxygen-to-HMDSO ratio of (a) 3, (b) 6 and (c) 10. The edge of the crack is positioned in the middle of each image. The upper part represents the surface of the coating and the lower part displays the microstructure of the cracked coating.

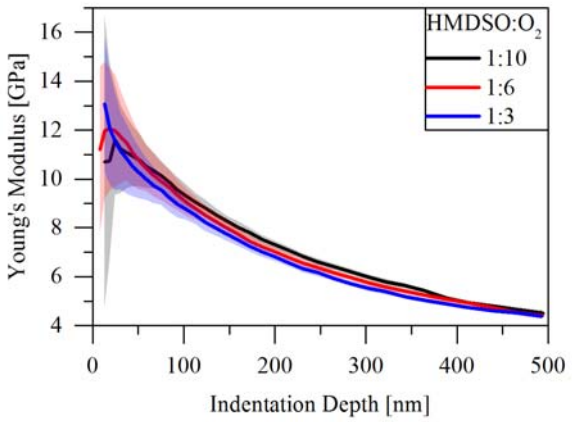

Figure 4. Continuous stifness measurements of the three coatings measured on the 1000 nm thick coatings. Within experimental error, no significant changes are visible.

The qualification of different techniques for mechanical characterization has been discussed in chapter 4. As shown, a combination of different methods proved the most reliable way to characterize the coatings. In this chapter, a combination of Continuous Stiffness Measurements (CSM) and Atomic Force Acoustic Microscopy (AFAM) was used. CSMs were performed on all three coatings with identical (1000 nm) thickness to narrow down the range of expected moduli as well as to obtain information on the difference between the different coatings. Figure 4 shows the measured Young's moduli as a function of the indentation depth. All curves immediately descent from the beginning and approach the Young's modulus of the substrate within the first 500 nm. Within experimental error, no significant differences are observed between the coatings indicating similar Young's moduli. All coatings show initial values around 12 GPa and decrease towards the Young's modulus of the substrate. This indicates that the Young's moduli of the coatings are very similar and have values above 12 GPa.

Exact quantification was done using AFAM and the measured values were shown in Table 2. These measurements agree that there is no significant difference between the coatings. The value of 20 ± 2 GPa lies within the range of expected moduli based on the CSM and is assumed to be a good approximation for the calculation of the residual stress.

The similarity in the moduli was unexpected as theory usually states that the Young's modulus increases with decreasing organic content. This indicates that the more inorganic coatings may have a slightly higher porosity. This will be further discussed in section 5.6 when discussing the intrinsic stress.

5.3 Curved deposition

The first contribution towards the residual stress that is related to the deposition geometry is $\sigma_{curved\ deposition}$. This part is related to the residual strain caused by the curved state of the substrate during deposition. $\epsilon_{curved\ deposition}$ is a function of the process drum radius and the substrate thickness and is given by [21]:

$$\epsilon = \frac{d_{substrate}+d_{coating}}{2\,r_{process\,drum}} \left(\frac{1+2\eta+\chi\eta^2}{(1+\eta)(1+\chi\eta)}\right) \tag{5.6}$$

In this equation, $d_{substrate}$ is the substrate thickness, r is the radius of curvature, $\eta = d_{film}/d_{substrate}$ and $\chi = \frac{E_{film}}{E_{substrate}}$. For values of $\eta \ll 1$ and $\chi \leq 10$, the second part of the equation approaches 1 and Eq. (5.6) can be well approximated by

$$\epsilon = \frac{d_{substrate}}{2\,r_{process\,drum}} \tag{5.7}$$

For a 75 µm thick PET substrate in the *labFlex® 200*, the elongation due to the curved substrate equals 0.015 %. Using Hooke's law, the stress contribution is estimated around 3 MPa which is almost negligible.

5.4 Web tension and viscoelastic deformation

The stress contribution that is unique for roll-to-roll processes is $\sigma_{web\ tension}$ and it is related to the externally applied tension to the substrate during the coating process. The applied web tension is induced by application of an angular momentum on the unwinder against the web direction and the application of an angular moment on the winder in the direction of the web. This is schematically shown in Figure 5. The applied angular momentum presses the substrate against the process drum. Since the web speed is controlled by the rotation of the cooling drum, a minimum web tension is required to ensure that the friction between process drum and web is high

enough to avoid slip movement between the drum and the substrate. The web is not supported between the winders and the process drum leading to elongation of the web in the machine direction and contraction in the transverse direction as the applied web tension is fully exerted on the web. Under constant web speed, the stress exerted on the web is the same as the web tension that is set in the process parameters and will be represented by F_w. During acceleration and de-acceleration, the forces increase or decrease, respectively. This thesis is limited to the situation of constant web speed as this represents the situation during the deposition of functional coating material.

Increasing the web tension does not only deform the substrate [22] but also improves the mechanical contact between the substrate and the process drum. The increased contact improves the heat transfer coefficient (See Chapter 2) and thereby reduces the temperature of the substrate. Higher web tension may be required for thermally sensitive substrate or during processes with a high thermal load.

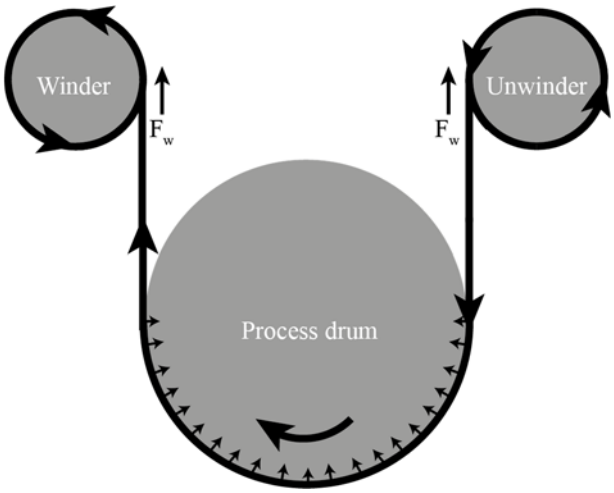

Figure 5. Schematic representation of a simple web path. The unwinder and winder exert an angular momentum to keep the web under tension. The resulting force F_w leads to elongation of the web between the winders and the process drum. The minimum web tension is required to press the substrate against the process drum and guarantee sufficient friction between the substrate and process drum to avoid any slip of the substrate.

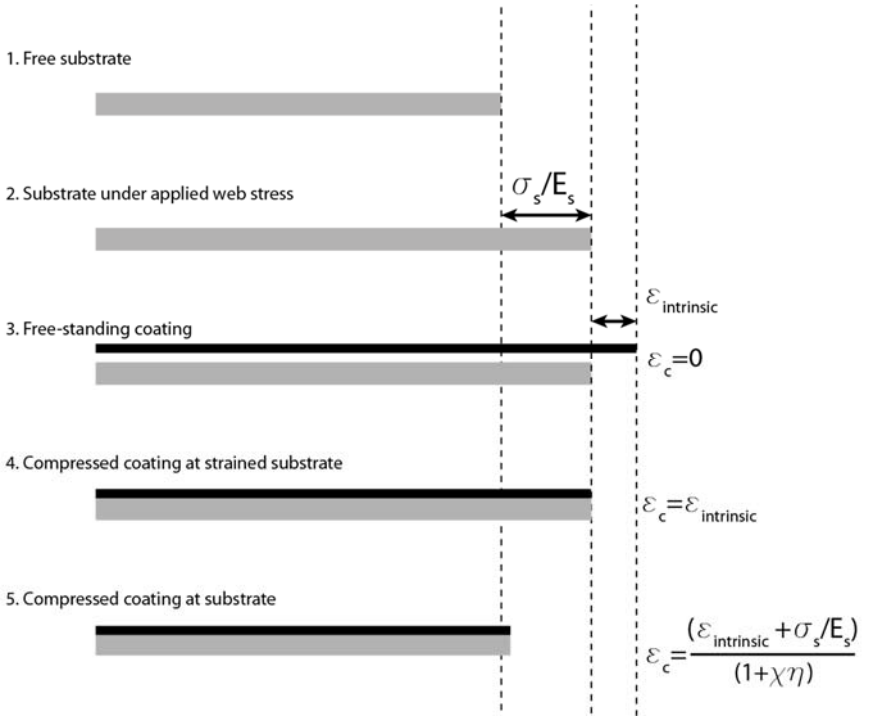

Figure 6. Schematics of the residual strain in the coating during the different stages of the deposition process. Based on [23].

Straining the substrate during the deposition leads to a mismatch in the strain of the coating and the substrate. The formation of residual strain in the coating during the different stages of the deposition is schematically presented in Figure 6. Initially, the substrate is in the unstrained position (step 1). During the winding process, the applied web stress leads to an elongation of the substrate (step 2) of σ_s/E_s with σ_s being the applied web stress and E_s is the Young's modulus of the web. Step 3 describes a fictive stage were the coating is grown as a free-standing coating without any residual strain ($\epsilon_c = 0$). After the coating is deposited to the substrate (step 4), the coating possesses a residual strain equal to the intrinsic strain ($\epsilon_c = \epsilon_{intrinsic}$). Figure 6 demonstrates the case for compressive intrinsic strain of the coating. The substrate contracts after of the web tension is removed (step 5) increasing the residual strain of the coating. Depending on the ratio of the Young's modulus and thickness of the coating and substrate

($\eta = h_c/h_s$ and $\chi = \frac{E_c}{E_s}$), part of ϵ_c will relax due to in-plane deformation of the substrate as was described in section 4.2. This effect is taken into account by adding the term $1/\chi\eta$.

The calculations made in this thesis do not include any contributions of the mismatch in the thermal expansion coefficients of the coating and the substrate. More information on the contribution on thermal effects can be found in the original model developed by Huang et al. [23,24]. They performed an extensive discussion on the temperature dependent Young's modulus of polymer materials. For PET, the Young's modulus can be well approximated using a temperature independent Young's modulus between 20 and 60 °C, which is the presumed temperature domain during the deposition. Assuming no significant thermal effects due to the change in web tension, we can keep all other parameters constant. Following the stages described in Figure 6, the residual strain in the coating can be calculated using compatibility of strains [25] and is described by

$$\epsilon_c = \frac{E_c \cdot h_c \cdot \frac{\sigma_s}{E_s} + \mathrm{h_c}\sigma_{intrinsic}}{E_s \cdot h_s + E_c \cdot h_c} \tag{5.8}$$

In this equation, h_c and h_s represent the thickness of the coating and substrate and E_c and E_s represent the Young's modulus of the coating and substrate, respectively. $\sigma_{intrinsic}$ describes the intrinsic stress in the coating.

As there is no information available on the intrinsic stress in the coating, a reference position with an applied web tension σ_{s0} and corresponding residual strain $\epsilon_{c,\sigma_{s0}}$ was measured. Assuming that all other contributions remain the same, this allows us to predict the change in ϵ_c under variation of σ_s. Rewriting Eq. (5.8) provides us with the following description of the residual strain:

$$\epsilon_c = \frac{E_c \cdot h_c \cdot \frac{\Delta\sigma_s(\varphi)}{E_s}}{E_s \cdot h_s + E_c \cdot h_c} \frac{1}{1+\chi\eta} + \epsilon_{c,\sigma_{s0}} \tag{5.9}$$

Where $\epsilon_{c,\sigma_{s0}}$ is the residual strain of the coating at the reference position and $\Delta\sigma_s$ is the difference in the applied web stress and the web stress at the reference position.

The residual strain of the coating cannot be measured directly. Therefore, the residual strain is calculated from the curvature of the specimen. The residual

strain in a thin coating on top of a relatively thick substrate with a radius of curvature equal to *R* can be described by [21]

$$\epsilon_c = \frac{h_s+h_c}{2R}\left(\frac{1+2\eta+\chi\eta^2}{(1+\eta)(1+\chi\eta)}\right) * 100\% = \frac{h_s+h_c}{2R}\,K \qquad (5.10)$$

The symbol *K* is used to improve the readability of the next equations. Combining Eq. (5.9) and Eq. (5.10) gives us:

$$\frac{h_s+h_c}{2R_{\Delta\sigma_s+\sigma_0}}\,K = \frac{E_c\cdot h_c\cdot\frac{\Delta\sigma_s(\varphi)}{E_s}}{E_s\cdot h_s+E_c\cdot h_c}\frac{1}{1+\chi\eta} + \frac{h_s+h_c}{2R_{\sigma_o}}\,K \qquad (5.11)$$

Eq. (5.11) allows us to predict the radius of curvature for samples with different applied web stresses provided that one reference measurement is available. Additionally, it can be used to calculate the curvature at $\sigma_s = 0$. As was discussed in section 5.1, the maximum radius of curvature is not always in the machine direction. Therefore, the change in curvature will only experience one component of the reduced applied stress as well as a contraction in the transverse direction. For samples were the maximum curvature is measured under an angle (φ), the corrected force under an angle φ is given by

$$\Delta\sigma_s(\varphi) = (cos(\varphi) - \nu\cdot\sin(\varphi))\cdot\Delta\sigma_s(0). \qquad (5.12)$$

Table 3. Used parameters of the deposited coating and for the substrate

Parameter	Values Melinex 401 CW
Web width	220 mm
$\boldsymbol{h_s}$	75 µm
$\boldsymbol{E_s}$	3.6 GPa (MD) /4.6 GPa (TD)
Poisson ratio	0.35
$\boldsymbol{h_c}$	454 nm
$\boldsymbol{E_c}$	20 GPa

Table 4. Relevant machine parameters for the LabFlex 200.

Parameter	Values in the *labFlex® 200*
Radius Process Drum	25 cm
Standard Web tension/stress	80 N / 3 MPa
Web width	220 mm

Further calculations and experiments on the effect of the applied web stress and the resulting elongation and coating stress are performed in the labFlex® 200 using a Melinex 401 CW PET substrate. The important machine and substrate parameters are provided in Table 3 and Table 4, respectively.

Figure 7 shows the predicted deformation of the substrate as a function of the applied web stress assuming linear elastic deformation. The solid line shows the elongation of the substrate in machine direction (MD). The dashed line shows the increasing contraction with increasing web stress. The vertical dotted line represents the standard settings used for experiments in this research. The markers represent the additional values tested to evaluate the effect of the applied web tension on the coating. The minimum value of 3 MPa (50 N) was the limit to guarantee sufficient heat dissociation and the maximum value of 8.4 MPa (140 N) was due to the machine specifications.

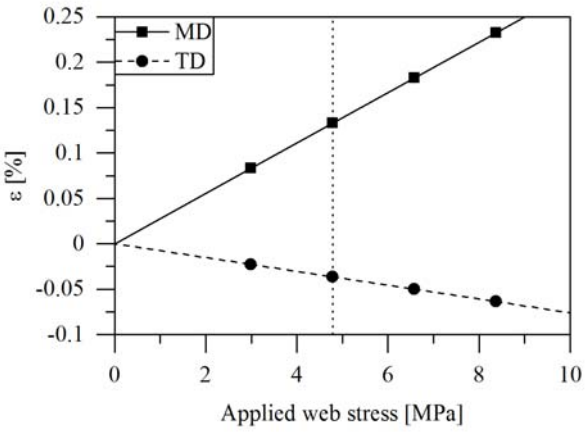

Figure 7. Calculated elongation of the substrate in MD and contraction of the substrate in TD as a function of the applied web stress for a Melinex 401 CW substrate.

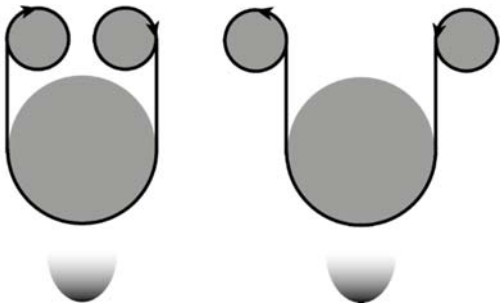

Figure 8. The left images shows the out-out winding configuration whereas the right image shows the in-in winding configuration. The substrate is coated at the bottom.

As the substrate is stored in a bended position before and after the deposition, visco-elastic deformation may lead to curvature of the substrate. To correct for any visco-elastic deformation during storage of the substrate before deposition as well as the coated substrate after deposition, two deposition experiments were performed with different winding paths shown in Figure 8. In both experiments, the same variation of the applied web stress between 3 and 8.4 MPa was tested under constant plasma process parameters. Both visco-elastic effects before and after the deposition contribute in compression towards the intrinsic stress in the first geometry, which is referred to as Out-Out. The second geometry, which is referred to as In-In, is chosen such that the visco-elastic effects contribute tensile toward the intrinsic stress.

The result of the experiment is shown in Figure 9. The horizontal axis shows the applied web stress in MPa and the vertical axis shows the measured radius of curvature in mm. The black squares present the experimental results and the red lines predict the theoretical change based on Eq. (5.12). As reference position (ϵ_{f,R_0}), the average of the two measurements at 4.8 MPa was taken. Figure 9a shows the result of the samples measured in the Out-Out configuration. The measured results show good agreement with the theoretical prediction and the radius at $\sigma_s = 0$ lies at 47.9 mm. For the samples deposited in the In-In configuration, the theoretical description shows good agreement with the experimental data with increasing web tension. The curvature of the sample with low web tension is 6.4 mm lower compared to the theoretical prediction. Small thermal wrinkles were

observed at this sample indicating that the low applied web tension was not high enough to provide sufficient cooling of the substrate during this deposition run. Assuming that the theoretical model provides good agreement if sufficient cooling is available, the radius of curvature at $\sigma_s = 0$ corresponds to 53 mm.

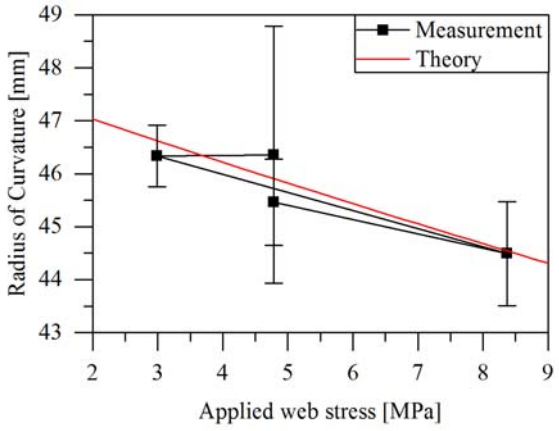

(a)

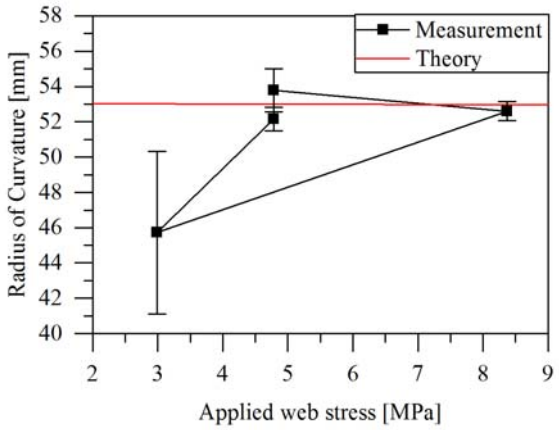

(b)

Figure 9. The measured radii of curvature are plotted as a function of the applied web stress for the (a) Out-Out configuration and the (b) In-In configuration. The red line predict the theoretical change. As reference, the averages value of the two measurements at 4.8 MPa was taken in both cases.

The larger radius (i.e lower residual stress) for the In-In configuration is in agreement with the visco-elastic change counterworking the residual stress. The radii of 47.9 and 53 mm correspond to residual stresses of 261 MPa and 236 MPa. Assuming that the effect is equal in both directions, the actual stress is 248 MPa. This indicates that the visco-elastic deformation, in this case, causes an error of 5% of the total residual stress.

The effect of visco-elastic deformation is specific for this deposition system. Additional parameters like storage-time, bending radius during storage and winding tension will play an important role towards the visco-elastic deformation. A detailed investigation is almost impossible as the storage times and storage conditions between production, slitting and delivery are usually not available. A dedicated investigation is required were detailed information on the visco-elastic contribution is necessary.

Validity of the web tension model

The theoretical predictions of the web tension model show good agreement with the experimental results. However, the samples were only tested in a very limited range of web tension and deposition parameters. To check whether the validity of the model can be extended, an additional experiment with magnetron sputtered aluminum (113 nm thickness, $E_c = 69\,GPa$) was deposited on a 23 µm thick PET substrate (Mylar, DuPont). Due to the smaller thickness, the range of applied web stress was much broader (between 8 and 24 MPa). ϵ_{f,R_0} was calculated at an applied web stress of 20 MPa. The result is shown in Figure 10. The black dots represent the measurements and the red line shows the theoretical prediction. Due to the larger range of applied web tension, the $1/\sigma_s$ tendency becomes more apparent. The theory and measurements show good agreement even though the measurements at lower applied web stress are slightly underestimated. This may be due to the nature of the 23 µm substrate that easily deforms under lower curvature and may lead to slight deformation of the sample.

To conclude, the good agreement in the two very different bi-layer systems and wide range of applied web stresses indicates that the theoretical description is a good approximation to calculate the influence of the applied web stress on the residual stress in roll-to-roll coated samples.

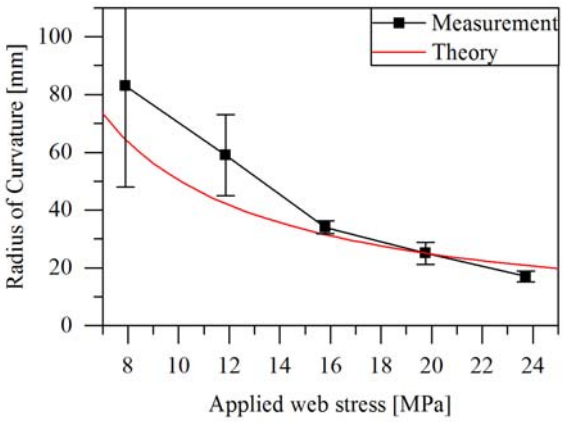

Figure 10. The measured radii of curvature are plotted as a function of the applied web stress. The red line predict the theoretical change. As reference, the measurement at 20 MPa was taken

Effect of web tension on the angle φ.

Additionally to the radius of curvature, the angle φ (see Figure 2) was studied to obtain a better understanding on the origin of the direction where maximum curvature occurs. Figure 11 shows the angle φ as a function the applied web stress for the coating deposited in the (black squares) In-In and (red dots) Out-Out configuration. Within each series, a small variation is observed which is related to the larger contribution of the applied web stress in the machine direction. For both series, the angles are decreasing with increasing web stress indicating that the stress in MD becomes larger as was predicted by Eq. (5.2) and (5.3). More interesting is the comparison between the In-In and Out-Out configuration which shows a change of sign when the angle φ is calculated with respect to the machine geometry. However, it should be considered that the back-side of the PET substrate is coated when changing the web path configuration from In-In to Out-Out. The change in signs strongly indicates that the angle is largely influenced by the anisotropy nature of the substrate. The blue triangles in Figure 11 show the same angles for the Out-Out configuration but calculated with the reference system chosen in correspondence with the substrate. The deformation at positive values of φ was understood by measuring the Young's modulus at $\varphi = 45°$ and $\varphi = -45°$ with respect to the substrate geometry (i.e. the black dots and

the blue triangles). The modulus at 45° was 3497 ± 17 MPa whereas the modulus at -45° corresponds to 5030 ± 218 MPa. The lower modulus at 45° shows less mechanical resistance and becomes the preferred direction for deformation.

Even though the black squares and blue triangles show the same slope, the absolute values have an off-set of 26 ± 3°. No clear explanation was found for this off-set. However, the complexity of the anisotropy related to the bi-axial deformation process during production of the PET requires a numerical model with extensive knowledge of angle-dependent Young's modulus, which is out of the scope of the thesis.

As a final note, the coating deposited with 3 MPa applied web stress in the In-In configuration shows a higher stress, which was earlier related to a thermal effect. As the thermal effect is an isotropic effect this does not lead to a shift in the angle, which agrees with the measured results.

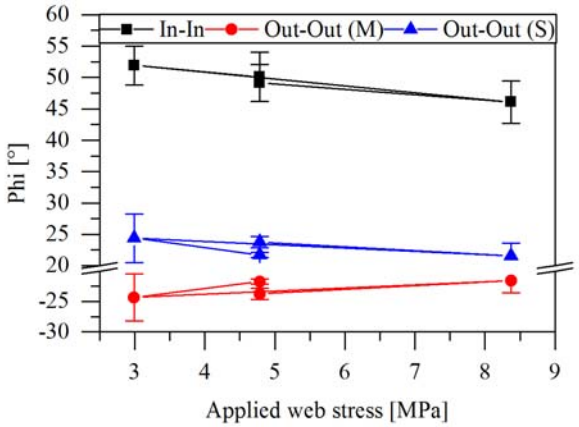

Figure 11. The measured angle φ is shown as a function of the applied web stress. The In-In and Out-Out configuration are marked by the black squares and red dots, respectively. The blue triangles represent the same measurement data as the red dots. However, the reference system was chosen according to the substrate instead whereas the red dots were calculated according to the deposition geometry.

5.5 Hygroscopic expansion of thin films

One of the stress contributions that is often ignored is the residual stress related to the difference in hygroscopic expansion of coating and substrate. Hygroscopic expansion induces, similar to the thermal expansion, a residual strain into the layer system due to a mismatch in the coefficient of hygroscopic expansion (CHE) of the coating and substrate. Even though several authors mention that hygroscopic expansion is significant and should be considered, scant literature is available that provides material properties related to hygroscopic expansion. Some research was executed on the hygroscopic expansion of silicon nitride and silicon oxide on a polyimide substrate [8,18]. It was found that silicon nitride coatings contract with increasing humidity whereas silicon oxide expands. For the latter case a hygroscopic expansion coefficient of 53 ± 55 10^{-6} (% r.h.)$^{-1}$ was found with a rather large experimental error. In this section, we introduce curvature measurements under controlled humidity at constant temperature (room temperature) and use the change in radius to calculate the coefficient of hygroscopic expansion for the coatings presented in section 5.2.

Calculation of the coefficient of hygroscopic expansion

This section explains the quantification from the measured radius to the coefficient of hygroscopic expansion. Changing the relative humidity induces a change in the mismatch strain, which can by described by:

$$\epsilon_{\phi 2} - \epsilon_{\phi 1} = (\beta_s - \beta_c) * (\phi_2 - \phi_1) \tag{5.13}$$

In this equation $\epsilon_{\phi i}$ represents the mismatch strain at ϕ_i % r.h.. β_s and β_c represent the coefficient of hygroscopic expansion on the substrate and coating, respectively. The residual strain can be calculated from the radius of curvature based using Eq. (4.5) as was described in section 4.2. Converting the residual stress into strain using Hooke's law gives us:

$$\begin{aligned}\epsilon_{1\to 2} &= -\frac{1-\nu_c}{1-\nu_s}\frac{E_s h_s^2}{6E_c h_c}\frac{1}{\left(1+\frac{h_c E_c(1-\nu_s)}{h_s E_s(1-\nu_c)}\right)}\left(1+\frac{h_c}{h_s}\left(4\frac{E_c}{E_s}-1\right)\right)\left(\frac{1}{R_2}-\frac{1}{R_1}\right)\\ &= -C\left(\frac{1}{R_2}-\frac{1}{R_1}\right)\end{aligned} \tag{5.14}$$

Were R_1 and R_2 and the radius of curvature at ϕ_1 and ϕ_2 % r.h.. The factor C is introduced to improve the readability of the equations. C is a specimen

depending parameter that depends only on coating and substrate properties and is independent of any environmental parameters. Eq. (5.13) and (5.14) can be combined to:

$$\left(\frac{1}{R_2}-\frac{1}{R_1}\right)=-\frac{(\beta_s-\beta_c)}{c}(\phi_2-\phi_1) \tag{5.15}$$

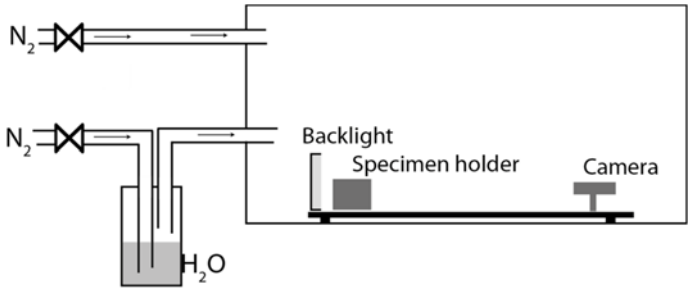

Figure 12. Schematic representation of the setup used for measurement of the CHE. The dark box represents the specimen holder with (directly left) the back light. The camera is located at the right.

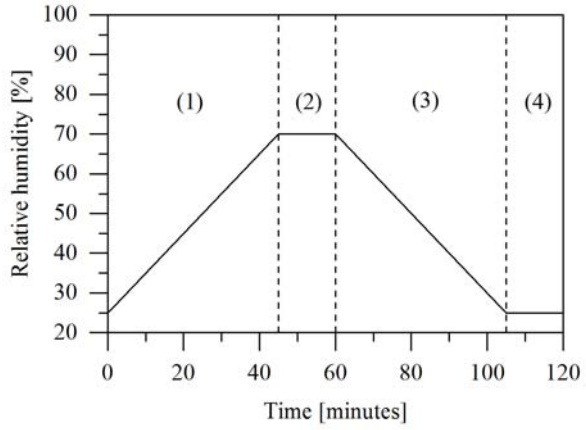

Figure 13 Schematic representation of the relative humidity as a function of time. (1) indicates the zone were the relative humidity is ramped up. (2) is the zone were the sample is relaxed and checked for any time-delayed effects. The relative humidity is ramped down in zone (3) and any time-delayed effects are again checked in zone (4).

Plotting the experimental data as $1/R$ against ϕ yields a linear relationship with the slope equal to $-\frac{(\beta_s-\beta_c)}{c}$. Eq. (5.15) can be used to calculate the coefficient of hygroscopic expansion of the coating provided that the hygroscopic expansion coefficient of the substrate is known.

Measurement of the coefficient of hygroscopic expansion

The measurements were performed with the setup described in chapter 4. The relative humidity was controlled by placing the measurement setup in a closed box (Aldrich® AtmosBag, Sigma Aldrich) as schematically illustrated in Figure 12. The relative humidity was controlled using nitrogen gas. The direct inlet of dry nitrogen reduced the relative humidity. The relative humidity was increased by feeding the nitrogen through a water reservoir before letting it into the chamber. Small holes made for the electrical connectors of the camera and backlight as well as an additional hole were sufficient to vent the bag and to avoid changes in pressure over time. The humidity and temperature in the chamber were monitored using an Extech RH30 hygro-thermometer. The error in the relative humidity was ± 4% according to the specifications of the manufacturer. This setup allowed us to control the humidity between 20% and 70%.

Chapter 4 identified three different error sources (specimen variation, mounting and calculation error). It is important to minimize the error as the hygroscopic change only induce small changes in the radius. Eq. (5.15) showed that only the change in radius, i.e. the slope of the curve, is relevant for the calculation of the CHE. Therefore, within each measurement series, one specimen was located on top of the specimen holder and remained untouched during variation of the relative humidity. This allowed us to rule out any errors due to specimen variation as well as errors due to mounting.

In preliminary experiments, the nitrogen flow was varied to check the response time of the coatings due to the change in humidity. A schematic representation of the relative humidity as a function of time is given in Figure 13. First, the sample was positioned at the sample holder and the box was conditioned at a relative humidity of approximately 25%. Section (1) (see Figure 13) represents the ramp up of the relative humidity and took approximately 45 minutes. In section (2), the humidity was kept constant and the radius of curvature was constantly monitored to see if any time-delayed

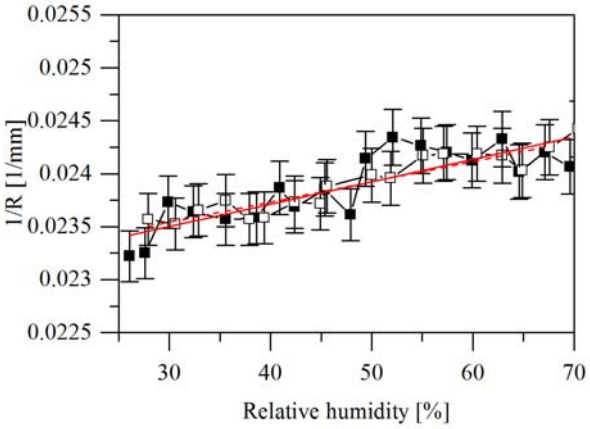

(a)

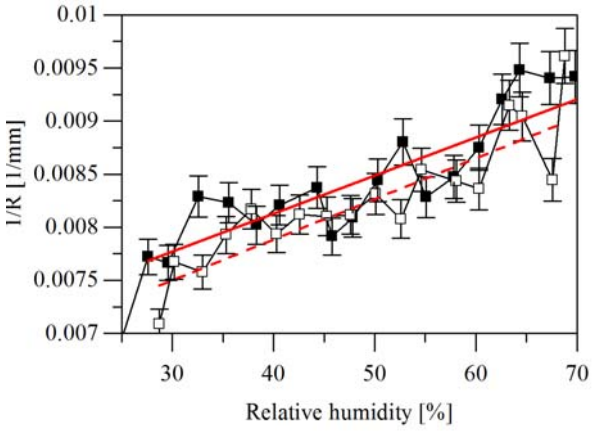

(b)

Figure 14 Experimental data of the 500 nm thick coatings with (a) low oxygen flow and (b) high oxygen flow. The y-scale represents 1/R in mm for both pictures. The scale is shifted due to the difference in residual stress. The filled symbols were measured under increasing relative humidity and the open symbols were measured while decreasing the relative humidity. The continuous and dashed line shows the least square linear fit of all data points for increasing and decreasing relative humidity, respectively.

effects could be observed. The humidity was decreased during section (3). Section (4) was again used to check for any hysteresis effects similar to section (2). As the humidity control was done manually, small deviations from this graph cannot be excluded. A curvature change upon a change in humidity was observed instantaneously. The curvature was monitored during the 15 minute period at constant humidity to check for any delay in the expansion effects. As no change in curvature was observed during these 15 minutes it was concluded that the reaction took place within the time-frame of the experiment. The time-scale agrees with results from Buchhold et al. [27] who showed that the absorption of water in 10 µm thick PI films from dry condition to 98% r.h. occurs within 10 minutes. The experiment as described in Figure 13 was performed for two different specimens, which were measured both in the convex and concave position. This allowed us to calculate eight slopes for each sample and the average was used to calculate the coefficient of hygroscopic expansion.

Figure 14 shows 1/R against the relative humidity for selected specimen with low (a) and high (b) oxygen flow. For clarity, only one of the specimens is shown in the graph. The results that are shown are similar to the results measured with other specimen. The horizontal axis represents the relative humidity and the vertical axis represents 1/R in mm^{-1}. The vertical axis is shifted between the two pictures due to the difference in the residual stress of the specimen. The absolute height of both vertical axis is identical (0.003 mm^{-1}) for both pictures. In all specimens, the radius of curvature decreases with increasing humidity. The filled symbols were measured while increasing the relative humidity whereas the open symbols were measured while decreasing the relative humidity. The continuous and dashed lines represent the least square fit of the data measured during increase of decrease of the relative humidity, respectively. The measured change in radius is clearly reversible and was found to be similar for different specimens and for measuring in concave and convex mode. The relation between 1/R and the relative humidity can be approximated by a linear function as was expected from Eq. (5.15). Some nonlinearities are visible but these were mainly related to a measurement error. The least- square fits in Figure 14a align almost perfectly for increasing and decreasing humidity. In Figure 14b, the dashed line lies slightly lower compared to the continuous line. The difference lies within the measurement uncertainty and is not systematic. A

higher offset on measurements at decreasing humidity has been observed as well for other specimen. The slopes of both linear fits, which are used to the calculation of the expansion coefficient, are very similar and therefore this effect was not further considered. It is clear that the slope of the specimen with the inorganic coating is higher compared to the slope of the organic coatings indicating that there is a measurable difference between the two coatings.

Influence of the carbon concentration on the coefficient of hygroscopic expansion

Fitting the slopes allowed us to calculate the coefficient of hygroscopic expansion using Eq. (5.15). *C* (in Eq. 5.15) is the same for all 500 nm thick coatings because the mechanical properties are the same and has a value of 11.4 ± 0.2 m/MPa. Figure 15 shows the results with the Oxygen-to-HMDSO ratio on the horizontal and the CHE (β_c) on the vertical axis. The (black) squares represent the 500 nm thick coatings whereas the (red) dot represents a specimen with 1000 nm coating thickness. The organic coating shows the lowest expansion coefficient with 19.5 ± 1.4·10^{-6} (% r.h.)$^{-1}$. Increasing the oxygen flow also increases the hygroscopic expansion coefficient up to 29.2 ± 2·10^{-6} (% r.h.)$^{-1}$ for the coating with the Oxygen-to-HMDSO ratio of 10.

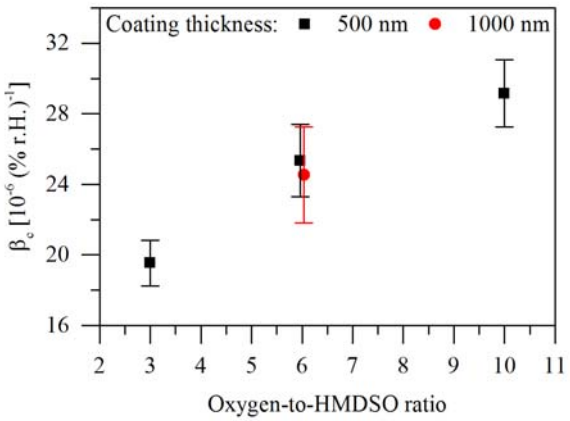

Figure 15. CHE (β_c) in dependence of the O_2/HMDSO ratio in the plasma for 500 nm thick layers on PET (black squares). The red dot denotes the sample with a 1000 nm thick coating.

The effects of the coating thickness was checked by measuring an additional specimen with a 1000 nm (instead of 500 nm) thick coating (Oxygen-to-HMDSO ratio: 6). The radius of the 1000 nm coating was 35 ± 5 mm compared to 75 ± 5 mm for the 500 nm coating. The CHE of $2.45 \pm 2.9 \cdot 10^{-6}$ (% r.h.)$^{-1}$ corresponds to the CHE of the thinner coating $2.54 \pm 2.1 \cdot 10^{-6}$ (% r.h.)$^{-1}$ within the experimental error. This confirms that the model corrects for the thickness effect of the coating and that the CHE does not depend on the coating thickness within the accuracy of our measurement.

5.6 Intrinsic stresses

Several publications discuss the relation between deposition process parameters and the residual stress of silicon-containing plasma polymer coatings. A brief overview of the available literature on PECVD processes with HMDSO and Oxygen is provided below.

Several groups used RF-Plasmas for the deposition of silicon-containing plasma polymers without additional heating of the substrate. Zajícková et al. [26] investigated the oxygen to HMDSO ratio for thick (> 1.5 µm) coatings on PC and measured tensile stresses for inorganic coatings and compressive stresses for organic coatings. They were able to deposit stress free layers with Oxygen-to-HMDSO ratios of 7.5 for a variety of applied plasma powers. Chaiwong et al. [27] observed faster spontaneous delamination of coatings deposited with an Oxygen/HMDSO plasma compared to coatings deposited with an Argon/HMDSO plasma without mentioning further details.

Liao et al. [28] relate the composite parameter (HMDSO/O_2)/Plasma power to the residual stress. They mainly observed compressive stresses that increased for lower values of the composite parameter. They observed low tensile stresses for high values of the composite parameter. This corresponds to Hegemann et al. [29] who found an increasing compressive stress with increasing power and increasing oxygen to HMDSO ratio. In addition, they observed a reduced compressive stress for higher deposition pressures.

This brief summary shows that several research groups worked on the relation between process parameters and residual stress. Even though some common tendencies were observed, the stress formation mechanism is still not completely understood and further experiments are still necessary. Most

research groups focus on RF plasmas. It is likely that the usage of a DC arc discharge plasma source has an effect on the stress formation mechanisms as well as it was shown that the RF frequency has an effect on the stress formation mechanism [30] as well.

The intrinsic stress in the coating was measured as described in chapter 4. Figure 16 shows the residual stress as a function of the Oxygen-to-HMDSO ratio. The measurements were performed at room temperature and low relative humidity (< 25%) to avoid for any environmental contributions. The (red) squares and the (blue) circles represent the coatings with a thickness of 500 and 1000 nm, respectively. The negative stresses mean that all coatings experience compressive stress. The 1000 nm coatings tend to have a slightly higher stress compared to the 500 nm coatings. A decrease of the residual stress (500 nm thick coating) from 240 MPa down to 102 MPa is observed with increasing oxygen flow. This corresponds to a reduction of 58% and is mainly contributed to a change in the intrinsic stress as all other mechanisms were found to have a much smaller impact. The observed trend corresponds to the observation by Zajíčková [26] even though we observed compressive stresses for all our samples whereas Zajíčková already observed tensile stresses for Oxygen-to-HMDSO ratios above 7.5. This could be explained by Hegemann's observation that coating stresses become more compressive if deposited at lower pressure. Zajíčková had a pressure between 1.2 Pa (for very low oxygen flows) up to 43 Pa (for high oxygen flows). Based on the data provided by Zajíčková, the pressure in the deposition chamber during the deposition of coatings with tensile stresses was above 15 Pa whereas the pressure in our experiments was kept constant at 2.7 Pa.

Table 5 gives an overview of the experiments mentioned in the earlier presented literature on the change in residual stress with increasing oxygen flow. Increasing the Oxygen-to-HMDSO ratio can lead to both increase and decrease in the residual stress. As we observe a decrease in the residual stress, it is tending to take a closer look at the changes in the chemical bonds present in the coating in order to explain the difference between the different groups. FTIR-ATR measurements were performed on the 1000 nm samples to avoid any absorption of the substrate.

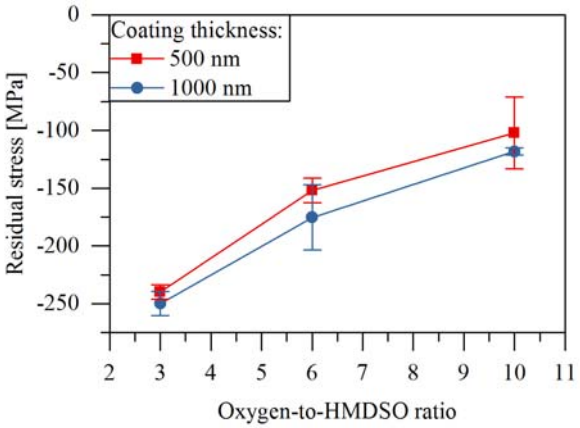

Figure 16. Measured residual stress as a function of the Oxygen-to-HMDSO ratio for the (red square) 500 nm and (blue dot) 1000 nm thick coatings. The negative values indicate that the coatings show compressive stress.

Table 5. Literature overview of publications were the relation between Oxygen-to-HMDSO and the residual stress were investigated. - indicates that there was no information available. The last row represents the results obtained in this chapter.

Oxygen-to-HMDSO	**Oxygen flow**	**HMDSO Flow**	**Power**	**Pressure**	**Stress**	**Source**
↑	↑	Cst.	Cst.	↑	↓	[26]
↑	↑	Cst.	Cst.	-	↑	[28]
↑	Cst.	↓	Cst.	-	↑	[28]
↑	↑	-	↑	↑	↑	[29]
↑	**↑**	**Cst.**	**Cst.**	**Cst.**	**↓**	

Similar to the coatings in Chapter 3, a large peak between 1100 and 1000 cm^{-1} was observed, which is mainly assigned to Si-O-Si asymmetric stretching and Si-O-C rocking [31–34]. Increasing the oxygen flow shows a drastic increase in the number of Si-O-Si and Si-O-C bonds. A small peak

shift is visible from the SiO_2 layer that goes to lower wavenumbers as the layer becomes more organic. Park et al. [31] assigned this shift to a change in the angle between the Si-O-Si bonds. The angle can be determined by $n = 1134\ cm^{-1} \sin(\frac{\phi}{2})$ in which n is the wavenumber in cm^{-1} and ϕ is the angle between the bonds. Calculating the peak bond corresponds to a shift in the peak length from 127° to 131° with increasing inorganic content. The bond angle is much lower than 137° as was measured in for sputtered SiO_2 [35].

Figure 17 shows the peaks between 2750 and 4000 cm^{-1} for the three different coatings. The broad peak is observed between 3000 and 3500 cm^{-1}, which is assigned to the presence of -OH bonds [36]. -OH groups can be present both as SiO-H groups (chemical bonding) and H_2O (physical bonding). The latter group indicates the presence of micropores. The peak amplitude both increases and shifts to the right with increasing oxygen flow. This indicates that not only the amount of –OH groups increases but also the way –OH groups are incorporated changes. All 1000 nm thick coatings were analyzed. Because the coating thickness was the same for all coatings, the areas under the peaks were compared directly with each other without any additional normalization. Originpro was used to perform a deconvolution of the individual peaks.

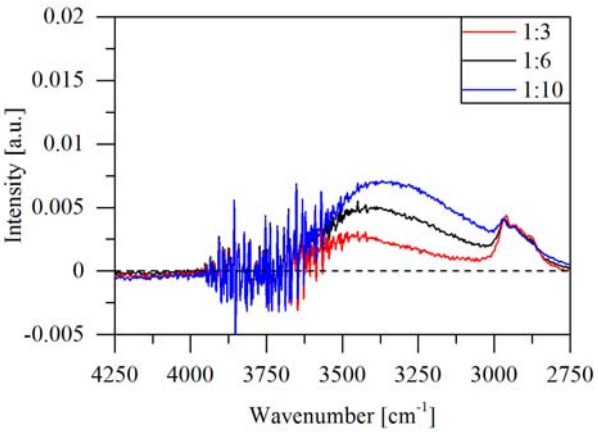

Figure 17. FTIR-ATR spectra of the 1000 nm thick coatings. The domain between 2750 and 3000 cm^{-1} indicates the presence of CH_x groups and peak between 3000 and 3750 cm^{-1} represents the presence of –OH bonds.

The deconvolution of the peaks was performed with 5 individual peaks corresponding to the H_2O and SiO-H peak as well as peaks for CH_2 and CH_3.(below 3000 cm^{-1}). The latter ones were not further considered in the quantitative evaluation as the effect between substrate and coating could not be strictly separated. The sole purpose to include these peaks in the deconvolution was to guarantee a good agreement between the fit and the measurement signal. The bare PET shows no absorption between 3000 and 3700, which allows us to designate the left two peaks to absorption in the coating. An example of the deconvolution is shown in Figure 18. The black line indicates the measurement signal and the red line the final fit. The green lines correspond to the individual absorption bands. The high noise level for wavenumbers above 3600 cm^{-1} is related to hydrogen in the measurement chamber. This noise limited the quality of the fit at the left side of the spectrum. Both the peak shape and peak center were used as fitting parameters.

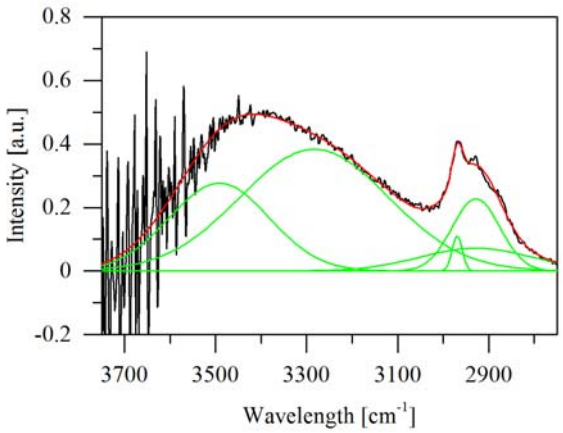

Figure 18. Example of the peak deconvolution in Originpro of the OH peak for the coating with 6 times more oxygen compared to HMDSO. The green and red lines represent the individual peaks of the deconvolution and the sum of the peaks, respectively. The black line represents the measurement signal. The noise at the left side of the spectrum was assigned to water vapor absorption.

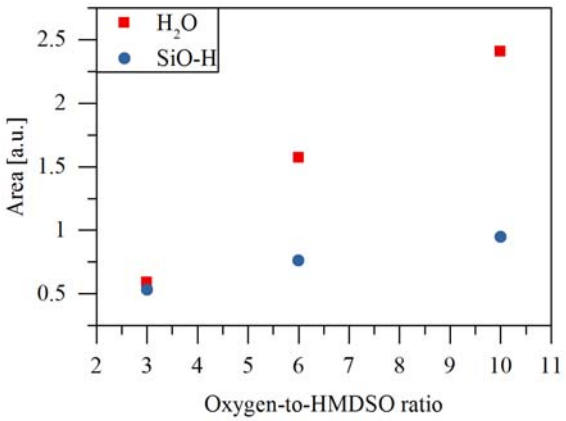

Figure 19. Calculation of the area corresponding to the H_2O and the SiO-H bonds after deconvolution. The number of both bonds increase with increasing oxygen flow.

The coatings with high oxygen flow had the center of their -OH peaks at 3266 ± 2 and 3481 ± 2 cm^{-1}. The peaks of the coating with an Oxygen-to-HMDSO ratio equal to 3 were shifted slightly higher and were found at 3283 and 3492 cm^{-1}. The locations of the peaks match well with literature and can be assigned to water molecules trapped in coating matrix and the hydroxyl stretch in neighboring silanol groups, respectively [37]. The peak at 3650 cm^{-1}, which is related to isolated silanol groups [38] was not observed but cannot be completely excluded due to the high noise level at the this part of the coating. The small peak shifts were mainly assigned as a fit error. No explanation was found in literature explaining the physical meaning of this shift.

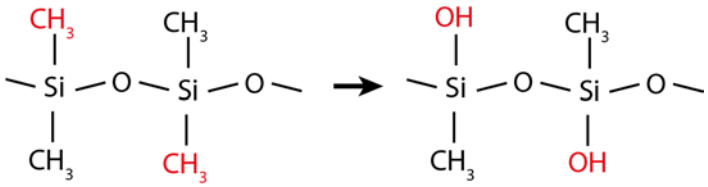

Figure 20. Schematic visualization of the chemical change with increasing oxygen flow. The CH_3 groups are replaced by OH groups..

The areas below the two peaks are plotted as a function of the oxygen-to-HMDSO ratio in Figure 19. Both the SiO-H and H_2O peak increase with increasing oxygen flow. The SiO-H peak increases with 70% whereas the water peak increases almost 4 times. The 70% increase of neighboring SiO-H bonds indicates that the additional oxygen per silicon molecule is largely included as additional OH groups connected to the silicon atoms instead of creating a SiO_2 network. This agrees with smaller angle of the Si-O-Si bonds compared to sputtered SiO_2 indicating that there is no real SiO_2 structure present but that CH_3 groups are replaced by OH groups as is schematically visualized in Figure 20. It is stressed here that the chemical structure is a theoretical visualization as the exact structure cannot be described due to the amorphous structure and the lack of information on the exact hydrogen concentration in the coating. It was shown that the presence of OH groups in SiO_2-like coatings increases the viscous flow and thereby contributes to the lower intrinsic stresses in the coating [39].

The increase of water trapped in the coating matrix indicates the increasing presence of pores within the coating [38,40]. The micro porosity of the coating can explain why the Young's modulus of the more oxide coating did not increase, even though it is known that the Young's modulus of bulk SiO_2 is much higher than 20 GPa.

Higher power per unit of monomer is necessary to increase the density and avoid the increased porosity as was discussed in chapter 3. This also explains why Liao [28] and Hegemann [29] observed increased residual stress for higher oxygen flows. Due to their choice of parameters, they increased the applied plasma power per unit of monomer with increasing oxygen flow. This reduced the porosity and leads to an increase in the residual stress.

5.7 Thermal stresses

As polymer coatings are only able to withstand a limited heat load, it is important to cool the PET substrate during the deposition process. In the *labFlex® 200*, the substrate is cooled on the back-side as it is contacted directly against a metal drum, which is water-cooled. Exact measurement of the substrate temperature is difficult due to the temperature gradient in the substrate as discussed in section 2.3.1. Contactless temperature measurements with a pyrometer were extensively tested during this research

but were not successful as the low substrate temperature leads to much lower thermal radiation power compared to the reflections of external heat sources or thermal fluctuations in the measurement device leading to substantial errors in the measurement.

Additionally, for the calculation of the residual stress, accurate data of the coefficient of thermal expansion is required. Experiments similar to the hygroscopic expansion were performed by locating the measurement setup in a climate chamber to control the temperature up to 50 °C. Whilst the hygroscopic expansion showed a direct and reversible effect, the change in curvature due to change in temperature takes over 500 minutes as can be seen in Figure 21.

The temperature was kept at 50 °C between the two dashed lines. The black lines was measured at room temperature as a reference. After 550 minutes, the sample was cooled down to room temperature again. The change in curvature remained after removal of the temperature indicating a non-reversible expansion of the coating or shrinkage of the substrate.

Accurately measurement of the surface temperature of the substrate as well as investigations in the thermal stress formation mechanism were not solved during the time-frame constraints of this thesis and are questions to be answered in future research.

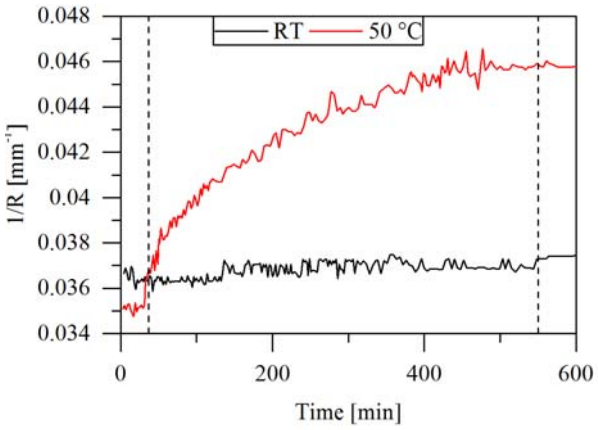

Figure 21. Measuring the effect of the temperature on the curvature (1/R) as a function of time. The red line represents a specimen that was heated to 50 °C between the two dashed lines. The black sample was measured at room temperature as reference.

5.8 Conclusions

This chapter provides an overview of the stress mechanisms of roll-to-roll coated thin films. For the coating dependent stress formation mechanisms, three different coatings with a different organic/inorganic fraction were compared and discussed.

The applied web stress leads to an additional curvature in the coating, which was predicted by the theoretical model. The applied web stress only slightly influences the radius of curvature for the plasma polymer coatings studied in chapter. It was however shown that for other coating systems, the error by neglecting the applied web stress can be significant and should be taken into account.

This chapter presents a method to accurately determine the hygroscopic expansion coefficients of thin film coatings provided that the substrate properties are known. The hygroscopic expansion coefficient of plasma polymer coatings on PET increased from $19.5 \pm 1.4 \cdot 10^{-6}$ (% r.h.)$^{-1}$ up to $29.2 \pm 2 \cdot 10^{-6}$ (% r.h.)$^{-1}$ with increasing oxygen flow.

The intrinsic stress was found to be the main contribution to the residual stress and could be lowered from 240 MPa to 102 MPa with an increasing oxygen-to-HMDSO ratio from 3 to 10. The increased oxygen flow led to incorporation of OH groups instead of the formation of a SiO_2-like chemical structure.

5.9 References

[1] Y. Leterrier, Durability of nanosized oxygen-barrier coatings on polymers, Progress in Materials 48 (2003) 1–55.

[2] M. Yanaka, T. Miyamoto, Y. Tsukahara, N. Takeda, In situ observation and analysis of multiple cracking phenomena in thin glass layers deposited on polymer films, Composite Interfaces 6 (1998) 409–424.

[3] M.-a. Yanaka, Y. Kato, Y. Tsukahara, N. Takeda, Effects of temperature on the multiple cracking progress of sub-micron thick glass films deposited on a polymer substrate, Thin Solid Films 355 (1999) 337–342.

[4] W.P. Vellinga, De Hosson, J. Th. M., P.C.P. Bouten, Effect of relative humidity on crack propagation in barrier films for flexible electronics, J. Appl. Phys. 112 (2012) 83520.

[5] Y. Leterrier, A. Mottet, N. Bouquet, D. Gilliéron, P. Dumont, A. Pinyol, L. Lalande, J.H. Waller, J.-A. Månson, Mechanical integrity of thin inorganic coatings on polymer substrates under quasi-static, thermal and fatigue loadings, Thin Solid Films 519 (2010) 1729–1737.

[6] S.L. Zhang, J.C.M. Li, Anisotropic elastic moduli and Poisson's ratios of a poly(ethylene terephthalate) film, J. Polym. Sci. B Polym. Phys. 42 (2004) 260–266.
[7] R. Feng, R.J. Farris, Linear thermoelastic characterization of anisotropic poly(ethylene terephthalate) films, J. Appl. Polym. Sci. 86 (2002) 2937–2947.
[8] Y. Leterrier, in: S. Logothetidis (Ed.), Handbook of Flexible Organic Electronics, Woodhead Publishing, Oxford (2015), 3–36.
[9] A. Morinaka, Y. Asano, Residual stress and thermal expansion coefficient of plasma polymerized films, J. Appl. Polym. Sci. 27 (1982) 2139–2150.
[10] P. Dumont, G. Tornare, Y. Leterrier, J.-A. Månson, Intrinsic, thermal and hygroscopic residual stresses in thin gas-barrier films on polymer substrates, Thin Solid Films (2007) 7437–7441.
[11] M.M. de Lima, R.G. Lacerda, J. Vilcarromero, F.C. Marques, Coefficient of thermal expansion and elastic modulus of thin films, J. Appl. Phys. 86 (1999) 4936–4942.
[12] U. Zaghloul, G.J. Papaioannou, B. Bhushan, H. Wang, F. Coccetti, P. Pons, R. Plana, Effect of Deposition Gas Ratio, RF Power, and Substrate Temperature on the Charging/Discharging Processes in PECVD Silicon Nitride Films for Electrostatic NEMS/MEMS Reliability Using Atomic Force Microscopy, J. Microelectromech. Syst. 20 (2011) 1395–1418.
[13] B. Borer, A. Sonnenfeld, Rudolf von Rohr, Ph., Influence of substrate temperature on morphology of SiOx films deposited on particles by PECVD, Surf. Coat. Technol. 201 (2006) 1757–1762.
[14] C. Y. Kim, S. H. Kim, R. Navamathavan, C. K. Choi, W. Y. Jeung, Characteristics of low-k SiOC(–H) films deposited at various substrate temperature by PECVD using DMDMS/O2 precursor, Thin Solid Films 516 (2007) 340–344.
[15] R. Buchhold, A. Nakladal, G. Gerlach, K. Sahre, K.-J. Eichhorn, M. Müller, Reduction of mechanical stress in micromachined components caused by humidity-induced volume expansion of polymer layers, Microsystem Technologies 5 (1998) 3–12.
[16] M.J. Adamson, Thermal expansion and swelling of cured epoxy resin used in graphite/epoxy composite materials, Journal of Materials Science 15 (1980) 1736–1745.
[17] Y. Y. Chang, H. Chung, B. J. Lwo, K. F. Tseng, In Situ Stress and Reliability Monitoring on Plastic Packaging Through Piezoresistive Stress Sensor, IEEE Transactions on Components, Packaging and Manufacturing Technology 3 (2013) 1358–1363.
[18] C.B. Masters, N.J. Salamon, Geometrically nonlinear stress-deflection relations for thin film/substrate systems, International Journal of Engineering Science 31 (1993) 915–925.
[19] G. Abadias, E. Chason, J. Keckes, M. Sebastiani, G.B. Thompson, E. Barthel, G.L. Doll, C.E. Murray, C.H. Stoessel, L. Martinu, Review Article: Stress in thin films and coatings: Current status, challenges, and prospects, J. Vac. Sci. Technol. A 36 (2018) 20801.
[20] E. Chason, P.R. Guduru, Tutorial: Understanding residual stress in polycrystalline thin films through real-time measurements and physical models, J. Appl. Phys. 119 (2016) 191101.
[21] Z. Suo, E.Y. Ma, H. Gleskova, S. Wagner, Mechanics of rollable and foldable film-on-foil electronics, Appl. Phys. Lett. 74 (1999) 1177–1179.
[22] W.E. Hawkins, The Plastic Film and Foil Web Handling Guide, CRC Press, 2002,

[23] Y. Huang, J. Chen, Z. Yin, Y. Xiong, Roll-to-Roll Processing of Flexible Heterogeneous Electronics With Low Interfacial Residual Stress, IEEE Transactions on Components, Packaging and Manufacturing Technology 1 (2011) 1368–1377.
[24] Y. Huang, Z. Yin, Y. Xiong, Thermomechanical analysis of thin films on temperature-dependent elastomeric substrates in flexible heterogeneous electronics, Thin Solid Films 518 (2010) 1698–1702.
[25] Yin Zhang, Extended Stoney's Formula for a Film-Substrate Bilayer With the Effect of Interfacial Slip, J. Appl. Mech. 75 (2008) 011008.
[26] L. Zajíčková, V. Buršíková, V. Peřina, A. Macková, D. Subedi, J. Janča, S. Smirnov, Plasma modification of polycarbonates, Surf. Coat. Techn. 142 (2001) 449–454.
[27] C. Chaiwong, P. Rachtanapun, S. Sarapirom, D. Boonyawan, Plasma polymerization of hexamethyldisiloxane: Investigation of the effect of carrier gas related to the film properties, Surf. Coat. Technol. (2013) 12–17.
[28] W.-B. Liao, Y.-C. Chang, C.-C. Jaing, C.-L. Cheng, C.-C. Lee, H.-S. Wei, C.-C. Kuo, Varying stress of SiO_xC_y thin films deposited by plasma polymerization, Appl. Opt. 56 (2017) 140-144.
[29] D. Hegemann, H. Brunner, C. Oehr, Deposition rate and three-dimensional uniformity of RF plasma deposited SiOx films, Surf. Coat. Techn. 142-144 (2001) 849–855.
[30] W.A.P. Claassen, Ion bombardment-induced mechanical stress in plasma-enhanced deposited silicon nitride and silicon oxynitride films, Plasma Chem. Plasma Process. 7 (1987) 109–124.
[31] Y.-B. Park, S.-W. Rhee, Microstructure and interfacial states of silicon dioxide film grown by low temperature remote plasma enhanced chemical vapor deposition, J. Appl. Phys. 86 (1999) 1346–1354.
[32] S. Saloum, M. Naddaf, B. Alkhaled, Properties of thin films deposited from HMDSO/O2 induced remote plasma: Effect of oxygen fraction, Vac. 82 (2008) 742–747.
[33] R. Reuter, K. Rügner, D. Ellerweg, de los Arcos, Teresa, A. von Keudell, J. Benedikt, The Role of Oxygen and Surface Reactions in the Deposition of Silicon Oxide like Films from HMDSO at Atmospheric Pressure, Plasma Process. Polym. 9 (2012) 1116–1124.
[34] M. T. Kim, Deposition behavior of hexamethydisiloxane films based on the FTIR analysis of Si–O–Si and Si–CH_3 bonds, Thin Solid Films 311 (1997) 157–163.
[35] M. Top, J. Fahlteich, J.T.M. De Hosson., Influence of the applied power on the barrier performance of silicon-containing plasma polymer coatings using a hollow cathode-activated PECVD process, Plasma Process Polym. (2017) e1700016.
[36] S. Holly, P. Sohár, L. Láng, Absorption spectra in the infrared region, Akadémiai Kiadó, Budapest, 1977.
[37] M. Creatore, S.M. Rieter, Y. Barrell, M. van de Sanden, R. Vernhes, L. Martinu, Optical and chemical characterization of expanding thermal plasma-deposited carbon-containing silicon dioxide-like films, Thin Solid Films 516 (2008) 8547–8553.
[38] W.A. Pliskin, Comparison of properties of dielectric films deposited by various methods, J. Vac. Sci. Technol. 14 (1977) 1064–1081.
[39] S. B. Desu, Stress and Structural Relaxation in Metallo-Organic Chemical Vapor Deposited SiO 2 Films, Jpn. J. Appl. Phys. 30 (1991) 2123-2126.

[40] A. Brunet-Bruneau, J. Rivory, B. Rafin, J.Y. Robic, P. Chaton, Infrared ellipsometry study of evaporated SiO_2 films: Matrix densification, porosity, water sorption, J. Appl. Phys. 82 (1997) 1330–1335.

Chapter 6

Summary and Outlook

This thesis discusses the functional properties of silicon-containing plasma polymer coatings that are deposited using hollow cathode arc discharge based PECVD. This high-rate PECVD process shows great potential to replace state-of-the-art PECVD technologies like Radiofrequency or Microwave PECVD within high-rate and large area applications. This final chapter summarizes the scientific conclusions obtained in the previous chapters and provides a brief overview of possible future applications and remaining challenges.

6.1 Summary

Chapter 3 provided an extensive discussion on the permeation barrier functionality of plasma polymer coatings. Against expectation, the inorganic coatings (SiO_2H_x) showed no significantly improved permeation barrier properties over the bare PolyEthylene Terephthalate (PET) substrate (7,9 g/(m²day) measured at 38 °C and 90 % r.h.). However, the organic coatings ($SiOCH_x$) did show an improved barrier on the provision that the energy per HMDSO molecule was sufficient to completely dissociate the monomer and create a dense network. Increasing energy per HMDSO molecule allowed for the breaking of C-H bonds and thereby reduces the number of hydrogen atoms in the coating. This allowed for denser coating structures with improved permeation barrier performance. On normal PET, the reduced WVTR was limited to 0.16 g/(m²day) with a applied plasma power of 63 W/(sccm HMDSO) as further increase in the applied plasma power led to

thermal damage of the substrate. Using a thermally more stable PolyEthylene Naphthalate (PEN) film allowed us to increase the power up to 116 W/sccm HMDSO without damaging the film. The reduced WVTR down to 0.05 g/(m²day) shows that there is still room for improvement.

Unfortunately the increased plasma power lead to high residual stresses within the coating. As these high residual stresses could lead to delamination and device failure when applied within e.g. organic electronic devices, the main part of this thesis investigated the stress formation mechanism within these coatings and separated the different contributions within a roll-to-roll process to understand their contributions towards the total residual stress.

As the thin flexible substrate and relatively thick coatings led to small radii of curvature compared to e.g. thin coatings on silicon wafers. Standard characterization methods were not very suitable to reliably characterize the radius of curvature and an alternative method was introduced in **Chapter 4**. A simple measurement setup was designed that uses an optical camera to image the cross-section of an almost free-standing specimen. An image-processing script allowed us to calculate the radius of curvature.

For reliable calculations of the mechanical coating properties, four different nanoindentation and AFM based techniques were tested and compared to find a reliable method for measuring the Young's modulus of the thin films. Continuous stiffness measurements are influenced by the substrate and therefore underestimating the mechanical properties. The AFM based methods are able to solely characterize the coating by using indentation depths around 5 nm. Unfortunately, these low indentation depths require extensive knowledge about the contact mechanics between the tip and sample which is still not fully understood for non-flat (Ra > 2 nm) and thereby should be carefully interpreted. The Atomic Force Acoustic Microscopy technique with an improved contact mechanical model seems to be very promising for these types of coatings but requires critical analysis for samples with higher roughness. NanoDMA measurements at the cross-section of the coating are very promising provided that the cross-section has a very smooth surface. This technique requires more experimental effort but is very promising for coatings with high surface roughness.

Chapter 5 was dedicated to the different contributions towards the total residual stress. The applied web stress and curved substrate only have small

influence of the residual stress for the samples within this chapter. It should be taken into account that especially for thin substrates (< 50 µm), the contribution of the applied web stress becomes more significant. It was found that the orientation of maximum curvature was affected by the web tension but was mainly determined by the non-isotropic mechanical properties of the substrate. The visco-elastic deformation before and after the deposition contributes tensile or compressive towards the measured residual stress using In-In and Out-Out web-path configurations, respectively. An effect up to 5% was found for this specific experiment. As the actual contribution depends not only on the configuration but also on the storage time, this error was neglected within further contributions

The effect of the relative humidity on the residual stress was closely investigated by accurate curvature measurements under controlled relative humidity and constant temperature. The hygroscopic expansion coefficient of the coatings was calculated and was found to increase with increasing oxygen content. This was mainly assigned to the increased porosity of the coating. Analysis of 500 and 1000 nm thick coatings showed that the hygroscopic expansion coefficient is independent of the coating thickness within the measured range.

Accurate calculation of the coefficient of hygroscopic expansion help to improve the accuracy of numerical simulations studies on e.g. failure mechanisms of MEMS or organic electronics.

The last section discussed the influence of the reduced carbon concentration on the intrinsic stress. It was found that the intrinsic stress is the main contribution to the residual stress for the coatings studied in this chapter. The intrinsic stress was reduced by almost 60% for when decreasing the atomic ratio of carbon to silicon from 2.8 to 1.6. FTIR spectroscopy indicated that the increased oxygen flow does not lead to a SiO_2-like structure but rather the replacement of methyl groups by silanol groups. However, due to the lack of information on the hydrogen content, the changes at a molecular level remain not completely understood.

6.2 Applications

Even though we only started to unravel the mechanism behind the residual stress formation, the investigations during this PhD project provide a solid

base for the application of coatings deposited using hollow cathode arc discharge based PECVD within several industrial applications. Within the scope of industrialization, several promising business case studies were already initiated to provide a proof of concept. Detailed investigations whether or not these coatings meet all the required specifications should be performed in close collaboration with industrial partners. A selection of these business cases are introduced in the rest of this section.

Improved robustness of barrier coatings.

Chapter 3 showed that the deposited plasma polymer coatings may have an intrinsic barrier function down to 0.05 g/(m²day) but only with a significant thermal load that exceeds the thermal load of most polymer substrates. The usage of 100 nm thick magnetron sputtered coatings like Aluminum Oxide or Zinc-Tin-Oxide (ZTO) allow us to reach water vapor transmission rates down to $5 \cdot 10^{-4}$ g/(m²day) and are thereby far more effective as a barrier deposition technology for organic electronics. The main drawback of these inorganic coatings is the limited mechanical robustness, which leads to defect-formation during roll-to-roll processing of these films. First tests showed that the in-line applications of a protective polymeric layer are able to improve the mechanical robustness of these barrier films. The robustness was qualified using a bending fatigue test that allowed us to expose large area films to a reproducible combination of bending load and mechanical contact.

A schematic representation of the fatigue tester is shown in Figure 1a. The sample is clamped at both sides and a metal drum is positioned in the middle of the sample. The coating is pointed upwards (red line) and is therefore in direct contact with the metal drum. The left clamp is fixed whereas the left clamp moves up and down leading to a rolling movement of the sample over the surface of the coating. The mechanical robustness of a 30 nm ZTO coating deposited on a PET film (Melinex 401 CW, 75 µm) was tested was tested using a 250 cycles test with a polished metal drum (3 Kg, 38 mm diameter). During this test, the metal drum was in direct contact with the coating. The WVTR of a standard PET/ZTO film increases with a factor 10 during the fatigue test. The ZTO was protected by the application of a plasma polymer coating with thicknesses between 500 and 2500 nm on top of the

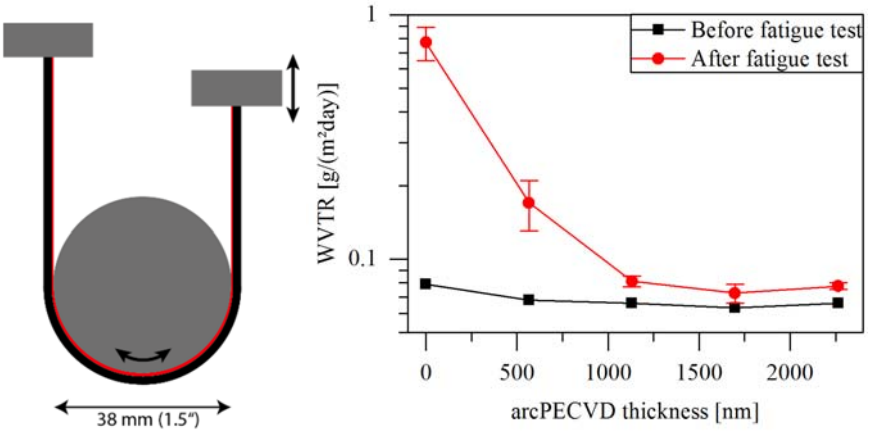

(a) (b)

Figure 1. (a) Schematic representation of the bending fatique test. The sample is clamped at both sides and a polished metal drum is placed in the middle. The left clamp moves up and down causing the metal drum to roll over the sample. One cycle consists of one movement downwards and upwards. (b) This graph shows the effect of the protective arcPECVD coating on top of a thin ZTO coating. The black squares represent the measured WVTR before the fatigue test. The red circles present the WVTR after fatigue testing. The protective function of the arcPECVD is optimized with the application of a > 1µm protective coating.

ZTO coating. The effect of the protective liner is shown as a function of the coating thickness in Figure 1b. Already with a 500 nm thick protective layer, the damage is reduced almost 50% compared to the bare ZTO/PET specimen. For coating thicknesses over 1 µm, the WVTR increases only 10-15%. This protective coating is a major advantage over single inorganic barrier films during roll-to-roll processing, as mechanical contact cannot always be avoided in industrial environments.

Improved adhesion of barrier coatings.

Most organic electronic devices are encapsulated using permeation barrier films. The barrier film is commonly fixated to the device using a Pressure Sensitive Adhesive (PSA) or UV-curable adhesive. These, usually organic adhesives show very little adhesion towards inorganic barrier coatings like Al_2O_3 and Zinc-Tin-Oxide. This leads to an overall reduced mechanical

stability of the final encapsulated devices as delamination may occur. The adhesion against the adhesive can be improved by the applications of a silicon-containing plasma polymeric coating. Within this business case, the peel force between the plasma polymeric coating and the barrier adhesive EL-92734 was tested using a German wheel peel test (Sebastian V) according to IPC-TM-650. The result of the peel force is shown in Figure 2. The increase in oxygen flow compared to the HMSDO flow leads to an increase in the inorganic content as was discussed in chapter 3 and 6. As can be seen, the organic coatings show good adhesion whereas the inorganic coatings show much lower adhesion. The adhesion of the inorganic coating corresponds to the adhesion between the EL-92734 and inorganic barrier coatings like Al_2O_3 (0.17 N/cm) and Zinc-Tin-Oxide (0.33 N/cm). Adding a thin organic PECVD-based coating on top of the inorganic barrier improves the adhesion towards the adhesive and thereby improves the overall mechanical stability of the device.

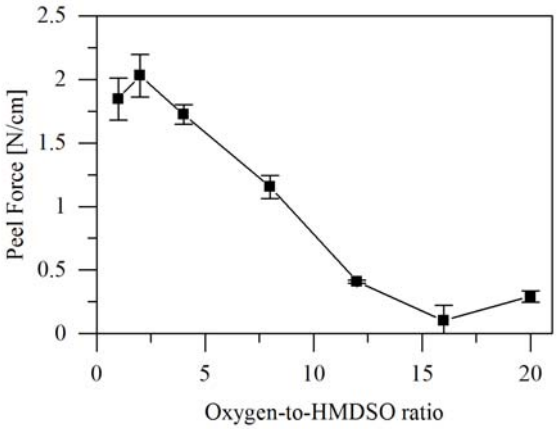

Figure 2. The adhesion between the barrier adhesive EL-92734 (Adhesives Research) and the plasma polymeric coatings was testing using a German wheel peel test (Sebastian V) according to IPC-TM-650. The average adhesion is displayed for different Oxygen-to-HMDSO flow ratios. The mainly organic coatings show a much higher adhesion (>2 N/cm) compared to the more inorganic coatings (< 0.25 N/cm).

For the low and high oxygen flow, there seems to be a local maximum and minimum in the adhesion, respectively. Understanding the adhesion between adhesives and the PECVD process parameters was out of the scope of this initial study and is topic of future investigations.

6.3 Outlook

The contributions of the different stress formation mechanisms were investigated for specimens with different carbon concentrations. As the porosity seems to play a major role, especially in the environmental conditions as well as for the intrinsic stress, an extensive evaluation towards the effect of applied power per unit of monomer would gain better understanding of the relation between the applied plasma power and the stress formation mechanisms. This would broaden the understanding from coatings with significant organic fractions up to mainly inorganic coatings

The main gap that was left in chapter 5 was the thermal contributions towards the residual stress. Accurate measurements of the surface temperature remain a big challenge and would help to improve the understanding of the growth mechanism as well as the residual stress formation mechanism.

Considering the mechanical characterization of thin stiff films of polymer substrates, no generic method was found that allows quick measurement of the mechanical properties. The development of AFMs as ultra-sensitive nano-indenters combined with an improved understanding of the contact mechanics seems to be very promising and should be continued to allow for the reliable and unambiguous characterization of thin films on all kinds of substrates within the years to come.

Dissemination

Peer reviewed articles

Hollow-cathode activated PECVD for the high-rate deposition of permeation barrier films; *M. Top, S. Schönfeld, J. Fahlteich, S. Bunk, T. Kühnel, S. Straach, J.T.H. De Hosson* (2017). In Surface and Coatings Technology 314, pp.155–159. DOI: 10.1016/j.surfcoat.2016.09.003.

Influence of the applied power on the barrier performance of silicon-containing plasma polymer coatings using a hollow cathode-activated PECVD process; *M. Top, J. Fahlteich and J.T.M. De Hosson* (2017). In Plasma Processes and Polymers 14 (9), p.1700016. DOI: 10.1002/ppap.201700016.

Effect of humidity on the residual stress in silicon-containing plasma polymeric coatings; *M. Top, G. Mulder, N. Prager, J. Fahlteich, J.T.M. De Hosson* (2018): In Surface and Coatings Technology 347, pp.46–53. DOI: 10.1016/j.surfcoat.2018.04.066.

Nanomechanical characterization of thin silicon-containing plasma polymer coatings on soft polymer substrates, *M. Top, S.A. Koeleman, T. Modes, O. Zywitzki, J. Fahlteich, J.T.M. De Hosson* (2018), Surface and Coatings Technology, *in preparation*

Presentations

Hollow-Cathode Activated PECVD for the High-Rate Deposition of Permeation Barrier Films; *M. Top, J. Fahlteich, S. Bunk, T. Kühnel, S. Straach and N. Schiller*; 59th Annual Technical Conference of the Society of Vacuum Coaters (2016) Indianapolis, USA.

Bringing permeation barriers to applications: From high barrier performance to functional films for flexible electronics; *M. Top, S. Hinze, J. Lorenz, S. Bunk, J. Fahlteich, M. Fahland;* ISFOE (2017) in Thessaloniki, Greece.

From high barrier films to functional encapsulation for perovskite and organic solar cells; *M. Top, J. Lorenz, N. Prager, J. Fahlteich, M. Fahland;* International summit on stability of organic and perovskite solar cells (2017) in St Julian's, Malta.

Application of high-rate PECVD for improved mechanical stability of roll-to-roll manufactured flexible organic electronics; *M. Top, N. Prager, F. Giebe, J. Lorenz and J. Fahlteich;* 2018FLEX (2018) in Monterey, USA.

Posters

Plasma monitoring of a hollow cathode activated PECVD process; *M. Top and J. Fahlteich*; 15th International Conference on Plasma Surface Engineering (2016) in Garmisch-Partenkirchen, Germany.

Mechanical characterization of thin plasma polymer coatings on compliant PET substrates; *M. Top, G. Mulder, J. Lukes and J.T.M. De Hosson*; Nanobruecken 2018 (2018) in Erlangen, Germany.

Acknowledgements

"Alone we can do so little, together we can do so much." -Helen Keller

The above quote by Helen Keller perfectly summarizes the most important lesson that I have learned over the last three years: everybody has their own strengths and we need to look for people that support us in the areas where we have little or no experience. I was fortunate to be surrounded by many great people who supported me along the road while writing this thesis and significantly contributed toward its success. I would like to use these last pages to thank these people.

I would like to start with Jeff de Hosson. Jeff, I already started working in your group during my bachelor studies and had a great time while working on my master thesis at the MK group. You helped me to find a great internship position in Dresden. After my decision to pursue a PhD in Dresden, you accepted the task as supervisor and supported me during numerous discussions on scientific problems, preparation of scientific papers and while writing my thesis. Your longtime experience in science supported me in many ways to finish this thesis successfully. It was a great opportunity to work with you.

Much closer to my “new home”, John Fahlteich was there as my supervisor at Fraunhofer FEP. John, you also supported me during my thesis with many discussions and gave me the freedom to develop myself on a scientific level. You were always enthusiastic (sometimes even exceeding my own enthusiasm) and showed abundant support along the way. I had the chance to develop myself in the numerous projects in which you involved me. I enjoyed every moment we have spent working together over the last 4 years and I am looking forward to the coming years.

This space is reserved for three very important colleagues who were essential during the preparation of this work: Nicole Prager, Sebastian Bunk and Thomas Kühnel. The three of you provided technical support during the many, many experiments that were performed for this thesis. Even though some experiments required a lot of machine preparation, high chances of cleaning the cooling drum afterwards or had very little chances of success, I cannot remember that one of you ever said “maybe we should skip this experiment” to yet another “I would like to try …:”. I had a great time working together with you and spending time at the web coaters. I would like to thank you for all your help. This project would not have been possible without your knowledge and support.

During the promotion, I had the opportunity to work in an amazing environment with many great colleagues within the Flat and Flexible Products department. I would like to thank everybody within our department for their contribution to a great working environment. I specifically want to mention all the students from both the Netherlands and Germany that gave me the chance to supervise them. I would like to thank Steffen Schönfeld, Maxens van Daalen, Sybren Koeleman, Guus Mulder, Sebastian Sörgel and Johanna Lorenz for their contributions toward the understanding of the hollow cathode supported PECVD process.

I would also like to thank Ulrike Bewersdorff-Sarlette and Martin Pfeiffer from Heliatek. Your interest in the “SiOCH”-coatings and our stimulating discussions were a great source of motivation for me to stay focused and to try to understand the deposition process even better.

Special thanks go out to the colleagues from the Materials Analysis department at FEP for their great support and numerous measurements that were included in this thesis. I would like to thank Kerstin for her support with the FTIR evaluation. I would also like to thank David and Vasek (MK) for their warm welcome when I stayed at the MK-Group and helped me to perform essential measurements. The results in Chapter 4 became a success due to the help and expertise of Malgorzata Kopycinska (Fraunhofer IKTS) and Jaroslav Lukes (Bruker).

Even though I was considered some kind of a workaholic, there was plenty of time to spend with friends. I would like to thank Daan, Jan, Jasper, Stephan, Anika, Juliane, Cindy and Nancy for the great time in Dresden (both at and

after work) as well as Dorian, Paul, Herre, Wytse, Jonas, Casper, Machteld and Lianne for the great time when I stayed in Groningen.

However, my greatest support in Dresden was Marlene. Marlene, I am happy to share my life with you. You were my cornerstone and supported me during the last three years. I am truly blessed to have you in my life and I am looking forward to the many years we have in front of us.

Last but not least, at the most important spot, I would like to thank my parents and brother. Looking back at the last 27 years, I had a great life and received all the support that I needed to develop myself toward the position where I currently am. *Bedankt voor alle steun en liefde die ik van jullie gekregen heb. Zonder jullie had ik dit nooit gehaald! Ik kijk uit naar de vele mooie jaren die we nog met elkaar hebben!*

Michiel Top, 27.6.2018